Cover Page

Universiteit Leiden

The handle http://hdl.handle.net/1887/18926 holds various files of this Leiden University dissertation.

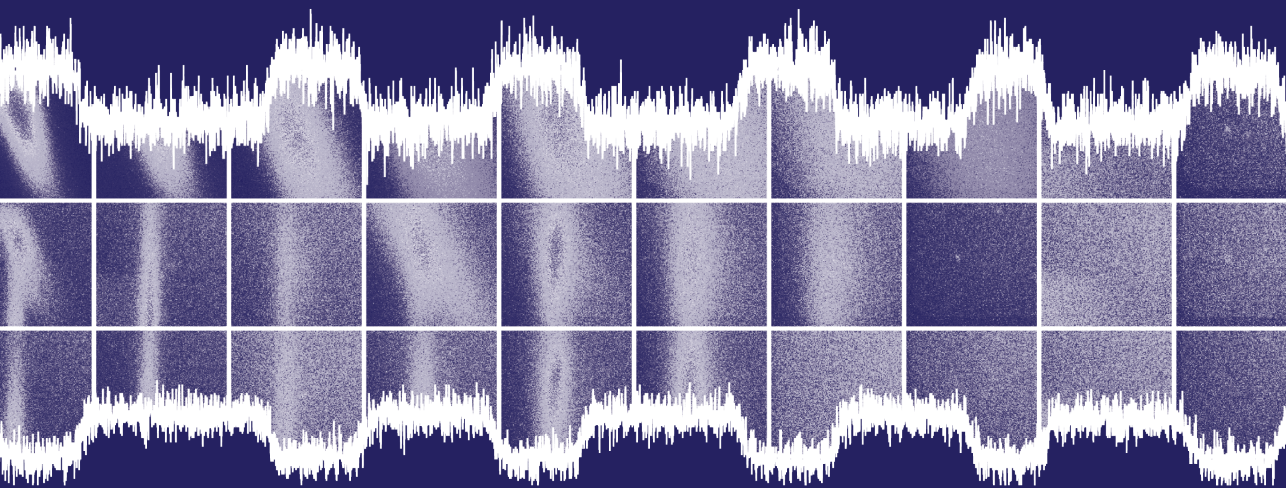# A Structural View of
Pd Model Catalysts

High-Pressure Surface X-Ray Diffraction

Richard van Rijn

A Structural View of Pd Model Catalysts

High-Pressure Surface X-Ray Diffraction

A Structural View of Pd Model Catalysts

High-Pressure Surface X-Ray Diffraction

PROEFSCHRIFT

ter verkrijging van
de graad van Doctor aan de Universiteit Leiden,
op gezag van Rector Magnificus prof. mr. P. F. van der Heijden,
volgens besluit van het College voor Promoties
te verdedigen op dinsdag 8 mei 2012
klokke 13:45 uur

door

Richard van Rijn

geboren te Delft
in 1983

Promotiecommissie

Promotor:	Prof. dr. J. W. M. Frenken
Co-promotor:	Dr. R. Felici
	European Synchrotron Radiation Facility
Overige leden:	Prof. dr. E. R. Eliel
	Prof. dr. M. T. M. Koper
	Dr. H. P. C. E. Kuipers
	Shell Global Solutions International B.V.
	Prof. dr. E. Lundgren
	Lund University
	Prof. dr. A. Stierle
	Deutsches Elektronen-Synchrotron / University of Hamburg
	Prof. dr. ir. B. M. Weckhuysen
	Universiteit Utrecht

aan mijn ouders

Contents

Contents

List of abbreviations

AFM	atomic force microscopy
DFT	density functional theory
EXAFS	extended x-ray absorption fine structure
FWHM	full width at half maximum
FTIR	fourier transform infrared spectroscopy
GISAXS	grazing incidence small angle x-ray scattering
IRAS	infrared reflection absorption spectroscopy
PEEK	polyether ether ketone
QMS	quadrupole mass spectrometry
SEM	scanning electron microscopy
SFG	sum-frequency generation
STM	scanning tunneling microscopy
SXRD	surface x-ray diffraction
TEM	transmission electron microscopy
TOF	turnover frequency
UHV	ultrahigh vacuum
XAFS	x-ray absorption fine structure
XPS	x-ray photoelectron spectroscopy
XRD	x-ray diffraction

Chapter 1

Introduction: heterogeneous catalysis and surface science

> Now even the wilderness of heterogeneous catalysis, the cornerstone of the chemical industry and one of the remaining bastions of empiricism, is beginning, reluctantly, one senses, to give way to the encroachment of high technology.
>
> *Sir David A. King [1]*

Eighteen years later, David King's statement aptly describes the state of the art in heterogeneous catalysis. The 'encroachment of high technology' has come a long way since 1994, but heterogeneous catalysis is a wilderness that remains very challenging to study at a fundamental level.

The phenomenon of catalysis was first recognized by Humphry Davy while developing a mine safety lamp known as the Davy lamp. Davy discovered catalytic oxidation by observing that a hot platinum wire immediately became incandescent in a mixture of coal gas and air [2]. The term catalysis was later coined by Berzelius [3], he writes about catalytically active materials:

> "It is proved, therefore, that many substances, simple and compound, solid and in a state of solution, possess the power of exercising upon compound bodies an influence essentially distinct from chemical affinity, an influence which consists in the production of a displacement, and a new arrangement of their elements, without their directly and necessarily participating in it, some special cases only excepted."

Since the time of Berzelius catalysis has become enormously important. One of the first applications of catalysis on an industrial scale came with the Haber-Bosch process for the synthesis of ammonia, indispensable for the production of

fertilizer for modern agriculture. Nowadays catalysis is used in a wide variety of fields ranging from the production of pharmaceuticals, the removal of sulphur components from fossil fuel, the production of plastics, the cleaning of harmful exhaust gases in three-way car catalysts, to the production of synthetic fuel. In 2011 the global annual market for catalysts was estimated to be in excess of \$29.5 billion [4].

With a phenomenon that is as important as catalysis it is surprising that most catalysts used today are still designed by a trial-and-error approach. The dream of scientists and engineers alike is to one day be able to design catalysts from first principles. To achieve this goal it is necessary to obtain a more complete understanding of all the phenomena taking place in a real catalyst on many different length and time scales. Generating essential atomic scale insight for the catalytic oxidation of CO on Pd, one of the reactions important in a car catalyst, is the aim of this thesis.

A practical catalyst is a very complicated system. The car catalyst is no exception. It consists of a honeycomb structure that supports the washcoat, a porous material which is impregnated with the catalytically active material in the form of noble metal nanoparticles. The three-way catalytic converter serves three purposes as the name suggests: the oxidation of all hydrocarbons that were not burned in the engine, the reduction of nitrous and nitric oxides to oxygen and nitrogen, and finally the oxidation of carbon monoxide. On the molecular scale one needs to understand the adsorption and desorption of molecules on the nanoparticles, the breaking of bonds in reactant molecules, and the formation of bonds in the products. The next level one needs to understand is the effects of the size, shape and composition of the metal nanoparticles on which the reactions are taking place. Sintering of the nanoparticles, poisoning by unwanted materials like lead for the car catalyst are other important effects to consider at this length scale. On a slightly larger length scale still there are parameters like the size of the pores of the support material and related diffusion phenomena and one also needs to consider the mechanical and thermal stability of the support. Finally one the largest length scales one needs to take into account the complete reactor design.

To understand phenomena on the atomic scale the traditional surface-science approach has been to study extended, single crystal surfaces of the same material as the metallic nanoparticles present in the catalyst. This translation to model catalyst surfaces, working at very low reactant gas pressures instead of the high gas

pressure they generally operate at, makes it easy to look at the surface with ions, electrons, and photons. This approach has been very fruitful for the understanding of many catalytic processes, as reflected in the Nobel Prize for Chemistry that was awarded to Gerhard Ertl in 2007 for his ground-breaking UHV studies of catalysts [5].

In spite of the tremendous progress that has been achieved with this 'traditional' surface-science approach, it is becoming increasingly clear that it is also necessary to study catalysts under practical operating conditions, because they may behave differently at high pressures and high temperatures compared to ultra high vacuum (UHV) and low-temperature conditions used in the traditional surface-science approach [6]. This has motivated the adaptation of many traditionally UHV surface-science techniques to bridge the so-called 'pressure gap'. Nowadays a range of techniques, spectroscopic, structural and morphological, is available to study extended surfaces at high pressures, each with their own advantages: scanning tunneling microscopy, x-ray photoelectron spectroscopy, sum frequency generation, transmission electron microscopy, and surface x-ray diffraction (SXRD), the technique employed in this thesis. The development of a dedicated flow reactor for SXRD experiments is detailed in Chapter 2. SXRD is a technique that is ideally suited to study crystalline surface structures [7, 8]. The real power of this technique in combination with the flow reactor is shown in Chapter 3 were we determine the structure of a Pd(100) surface under a variety of elevated O_2 and CO pressures and temperatures, and we correlate these structures with the catalytic behaviour of the surface.

Even model catalysts, free of the many complexities of a real catalyst, can show surprisingly complicated behaviour. This is best seen in Chapter 4, which describes our study of reaction rate oscillations on a Pd(100) surface. We identify the surface roughness as a new and crucial parameter that can determine whether the surface structure is metallic or oxidic in nature. The reaction follows a so called Langmuir-Hinshelwood mechanism if the surface is metallic[9], but a Mars-Van Krevelen mechanism if the surface is oxidic [10]. In the Langmuir-Hinshelwood mechanism the reactants, in our case CO and O_2, adsorb on the metallic surface and react with each other to from CO_2 as illustrated in Fig. 1.1a. The Mars-Van Krevelen mechanism, in contrast, has the CO reacting directly with the O atoms of the thin PdO layer as illustrated in Fig. 1.1b. The interplay of roughness evolution and the two different reaction mechanisms is shown to cause spontaneous reaction oscillations.
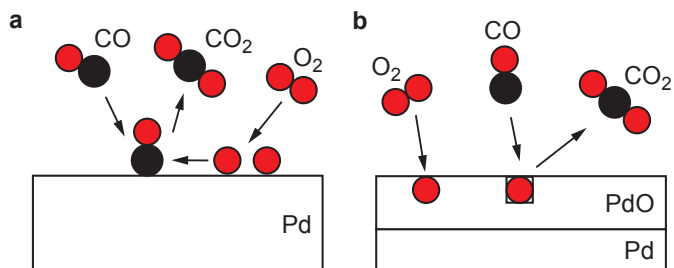
Figure 1.1: a) Langmuir-Hinshelwood mechanism **b)** Mars-Van Krevelen mechanism.

Studying an extended single crystal at high pressures is still very far from studying a real catalyst at operating conditions. On extended surfaces one excludes the effects of the particle size and shape and the interaction of the particles with the support. This gap between single-crystal model catalysts and real catalysts is called the 'materials gap'. In an effort to make model systems more realistic one can study nanoparticles supported on flat surfaces. In this way we can still use a sub-set of our techniques and employ these to study how the particles behave in situ and thereby address typical materials gap effects. Chapter 5 shows how we have used x-ray diffraction and grazing incidence small angle scattering (GISAXS, [11]) to study the size and shape of nanoparticles during spontaneous, self-sustained reaction oscillations.

Appendix A describes a part of the ongoing discussion about the most active surface phases and the role of metal oxides for CO oxidation on Pd. This discussion exemplifies the importance of combining and reconciling the results from the ever growing number of in situ techniques and first-principles computer calculations.

Chapter 2

Instrumentation: high-pressure surface x-ray diffraction

A versatile instrument for the in situ study of catalyst surfaces by surface x-ray diffraction (SXRD) and grazing incidence small angle x-ray scattering (GISAXS) in a 13 ml flow reactor combined with reaction product analysis by mass spectrometry has been developed. The instrument bridges the so-called 'pressure gap' and 'materials gap' at the same time, within one single experimental setup. It allows for the preparation and study of catalytically active single crystal surfaces and is also equipped with an evaporator for the deposition of thin, pure metal films, necessary for the formation of small metal particles on oxide supports. Reactions can be studied in flow mode and batch mode in a pressure range of 100-1200 mbar and temperatures up to 950 K. The setup provides a unique combination of sample preparation, characterization and in situ experiments where the structure and reactivity of both single crystals and supported nanoparticles can be simultaneously determined.

2.1 Introduction

Until the late 1990's, direct experimental evidence on the working mechanisms of heterogeneous catalysis at the molecular level was largely based on surface-science studies under ultrahigh vacuum (UHV) and high vacuum conditions ($<$ 10^{-5} mbar). UHV conditions provide electrons and ions long mean free paths compared to ambient pressure conditions, allowing one to use electron- and ion-based techniques, such as low energy electron diffraction and low energy ion scattering. This approach has been very successful in acquiring understanding of the fundamental interaction of molecules with single-crystalline surfaces for a large variety of catalytic systems [12, 13].

In industrial catalysis however, the vast majority of interaction processes of molecules with a surface happen at elevated temperatures and at high pressures ($>$1 bar). This discrepancy is known as the pressure gap [14]. Furthermore, a catalyst is usually not a macroscopic, low-index, single-crystal surface but very often it consists of oxide-supported nanometer size particles. Hence structural and electronic particle size effects and particle-support interactions likely influence the catalyst [15]. This last discrepancy is called the materials gap. There is a growing body of evidence that one can often not simply extrapolate UHV results to atmospheric pressures. The structure and morphology of the catalyst surface at realistically high pressures and temperatures may differ significantly from the situation at low pressures (and temperatures), which can lead to dramatic differences in reaction mechanism and catalytic performance (efficiency and selectivity). Recently a growing number of surface-science techniques, traditionally developed for UHV, are being adapted to operate under 'realistic' reaction conditions [16]. Notable examples of this development are high-pressure transmission electron microscopy (TEM) [17], high-pressure scanning tunneling microscopy (ReactorSTM) [18, 19], high-pressure x-ray photoelectron spectroscopy (XPS) [20], and high-pressure SXRD [21, 22].

The weak interaction of x-rays with low-electron-density materials (gasses) makes x-ray based techniques suitable for studying catalyst at realistic conditions. This is reflected in the large number of x-ray absorption fine structure (XAFS) and powder diffraction studies of catalysts. For studying catalytically active surfaces under realistic conditions, SXRD [7, 8] and GISAXS [11] are extremely suitable. It can be called surprising that only a handful of setups suitable for this type of research exist. The typical geometry for an SXRD type reactor is a

vessel with transparent walls for x-rays (e.g. beryllium, aluminium) in which one can introduce gas mixtures of different compositions. UHV is often required for proper sample preparation, so these vessels are often quite big (>1 liter) and can, apart from being used at high gas pressures, also be evacuated to pressures below 10^{-9} mbar. Another method frequently implemented is a UHV sample transfer from a preparation setup to the reactor setup. All these designs have the major disadvantage that the reactors are operated in batch mode, which implies that the gas composition in the reactor changes over the course of a measurement. Nevertheless excellent results have been obtained in batch reactors [23–26]. A second disadvantage of the transfer method is the necessary re-alignment of the sample with respect to the x-ray beam in diffraction experiments after each transfer.

In this paper we introduce a novel reactor setup for use in conjunction with a six circle diffractometer for SXRD/GISAXS experiments. It has been developed within the framework of a collaboration between the Interface Physics Group at Leiden University and the beamline staff at ID03, the surface diffraction beamline of the European Synchrotron Radiation Facility. The instrument bridges both the pressure gap and the materials gap without introducing the two disadvantages mentioned above (batch and realignment). It combines a small volume flow reactor with sample preparation under UHV-conditions. Furthermore it enables us to determine surface structure and morphology under reaction conditions by SXRD or GISAXS and simultaneously measure the reaction kinetics by mass spectrometry. Examples of reactions we would like to study are: CO oxidation on Pt-group metals (both single crystals and nanoparticles) [12–14], NO reduction on Pt-group metals [27], ethylene epoxidation on Ag nanoparticles [28], partial methane oxidation [29], desulphurization [30], and the Fischer Tropsch reaction [31]. We start by describing the requirements for such a setup and introduce the general architecture of the instrument. The paper ends with a demonstration of the performance of the instrument during CO oxidation experiments on Pd(111) and Pd(100).

2.2 Design Specifications

The combination of several sample preparation techniques typically requires a UHV chamber with a relatively large (>1 liter) volume. For the preparation of both single-crystal surfaces and oxide-supported nanoparticles (NPs), the instru-

ment has to combine facilities for ion bombardment, vacuum deposition and vacuum annealing. To guarantee sample cleanliness this preparation should be performed in situ, without transport through the atmosphere prior to experiments. Characterization of the sample at intermediate stages of preparation under UHV conditions should be possible with x-rays.

For experiments under catalytic conditions the requirements are different. The gas pressure around the sample needs to increase to the atmospheric pressure regime, while the gas composition in the reactor is determined by mass spectrometry simultaneously with the SXRD/GISAXS measurement. This experimental approach allows one to correlate reaction kinetics with surface structure and morphology.

Furthermore the partial pressures of the reactant gasses should be fully controllable and it should be possible to keep them constant in time. This is necessary in order to map out the precise behaviour of a model catalyst as a function of gas composition or as a function of time under constant gas and temperature conditions. This implies that the instrument should have the character of a flow reactor, rather than a batch reactor, in which the gas conditions would be changing continually. The characteristic refresh time of the reactor is determined by the reactor-volume-to-gasflow ratio, whereas the chemical resolution in the gas detection is determined by the sample-surface-to-gasflow ratio. For a given sample size and chemical resolution one would thus like to make the volume of the reactor small. This requirement obviously conflicts with the relatively large volume that is required for the sample preparation.

The reactor wall material needs to be a low Z material, e.g. beryllium, aluminium, or Kapton, to allow the x-rays to pass through. When the reactor is closed, no part of the setup, except for the beryllium window, is allowed to exceed the height of the sample, guaranteeing access to the full 2π hemisphere of incoming and diffracted photons. Since the setup is intended to be used for synchrotron based SXRD and GISAXS experiments, it should be designed to fit and move on a six-circle diffractometer. To make optimal use of expensive synchrotron beamtime a quick sample exchange mechanism is also required.

2.3 Design

In this section, we discuss the general architecture of the new setup, the design of its individual components, and the underlying considerations for specific design choices.

2.3.1 UHV Chamber

The combination of all the mentioned requirements suggests a setup which combines two compartments with a transport mechanism in between: a reactor part and a UHV part. Typically one would transport the sample after preparation from UHV to the reactor. For the x-ray diffraction experiments this would mean that one would have to realign the sample after every preparation cycle. For experiments at a synchrotron, this would imply an additional loss of valuable beamtime with every preparation cycle, a very undesirable situation. Instead of using a sample transfer mechanism we chose to keep the sample fixed inside the setup and to move the upper part of the setup around the sample. The design of the novel flow setup is shown in Fig. 2.1. The chamber consist of two steel plates connect by a bellow. The lower plate is mounted on a 5-axis positioning system that is part of a six-circle diffractometer [32]. The lower plate holds the sample holder, the quadrupole mass spectrometer (QMS) and the turbopump. The top plate holds the ion gun and evaporator and can be translated vertically. If the bellow is completely extended as shown in Fig. 2.1a, the setup is in the sample preparation configuration, in which the sample can be sputtered, annealed, and metal can be deposited on the sample. After preparation, the top part of the chamber can be lowered over the sample, as shown in Fig. 2.1b. This is achieved by compressing the bellow between the top and bottom plates by means of a chain drive mechanism, until the top flange lands on the sample holder support. In the latter geometry, the small volume around the sample is fully separated from the UHV in the remainder of the system, which consists of the compressed bellow and the sample preparation tools. The upper part of this small reactor volume is defined by a beryllium dome [33–35] with good transparency for the x-rays. The reactor walls (top flange and dome) are actively cooled by a water flow through the top flange as shown in Fig. 2.1a. This is done to prevent reactant gasses from reacting on and/or with the reactor walls at high temperatures. Both effects are highly undesirable.
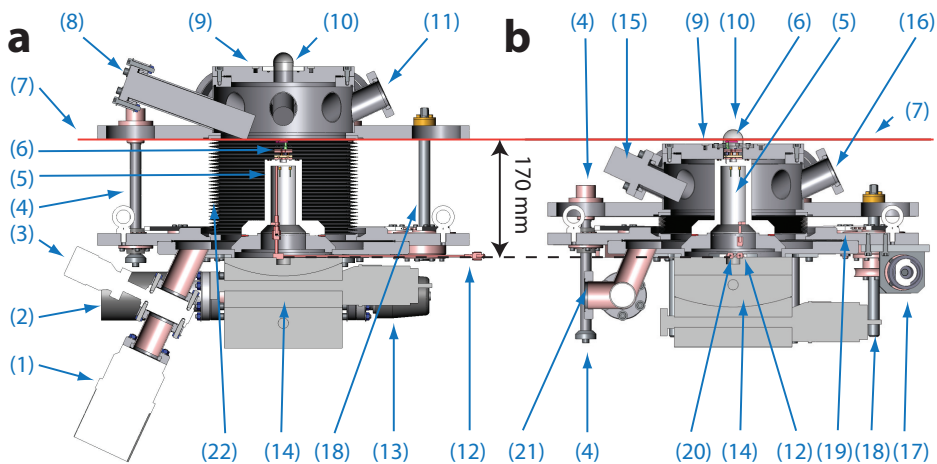
Figure 2.1: a) Cut view of the setup in the UHV sample preparation geometry. **b)** Cut view of the setup with closed reactor, 90° rotated with respect to the view of Fig. 2.1a. The beam is located 170 mm above the diffractometer sample stage surface. The labels denote: (1) turbo pump, (2) quadrupole mass spectrometer, (3) manual UHV valve, (4) guiding rods for vertical movement of top part of the chamber, (5) sample holder foot, (6) sample holder, (7) x-ray beam height, (8) evaporator port, (9) water-cooled top flange, (10) $180° \times 360°$ beryllium dome, (11) ion gun port, (12) reactor gas exhaust line, (13) UHV leak valve, (14) Huber five-axis positioning system, (15) cold cathode pressure gauge, (16) blind flange, (17) electromotor and drive shaft, (18) threaded drive rods for vertical movement of top part of the chamber, (19) chain drive mechanism for vertical movement, (20) gas entry line, (21) UHV vent valve, and (22) steel bellow.

The top flange seals the reactor from the UHV by a so-called V-seal®, that is normally intended for use in jet engines, cryogenic applications, etc. [36]. The V-seals are made of a gold coated nickel alloy, they seal UHV tight ($<$ 10^{-10} mbar l s^{-1} He) and are re-usable up to 30 times. The gold coating protects the seal from the reactants and guarantees its inertness. We prefer these V-seals over traditional elastomer seals, as the latter ones can only be used up to typically 500 K and they contain materials that might either influence the reaction or be influenced by the reactants.

Gasses are mixed in a gas system and transported to and from the reactor by two capillaries coming from under the sample holder support. Gas analysis was designed to be performed by dosing gas from the reactor exhaust pipe via a leak valve into the UHV part of the chamber, which is equipped with a QMS.

When the sample is in UHV the gas lines are closed with two Swagelok® manual valves. The sample mounting plane of the standard sample holder is situated 4 mm above the top flange.

The setup is currently equipped with the following UHV components:

- Varian V-81-M turbomolecular pump with a pumping speed of 50 l/s for N_2 and a compression ratio of 5×10^8 [37] ;

- Omicron EFM3 evaporator mounted under a 20° angle relative to the sample horizon [38];

- SPECS IQE 11/35 ion gun mounted under a 25° angle relative to the sample horizon [39];

- Arun Microelectronics cold cathode pressure gauge [40];

- MKS Instruments Micro Vision Plus QMS [41];

- Pfeiffer all metal regulating valve UDV 146. This valve is used for back-filling the chamber for ion bombardment of the sample [42];

- Beryllium dome with a radius of 14 mm and a wall thickness of 0.4 mm [33], or an aluminium dome with the same radius and a wall thickness of 1 mm.

Both the evaporator and the ion gun were slightly modified to minimize the blocking of the x-ray beam due to parts of these devices that would otherwise protrude above the sample surface.

2.3.2 Sample Holder

Figure 2.2a shows a cut view of the top part of the system, with the top flange in its lower position, so that the sample holder is fully enclosed by the reactor part of the setup. The x-ray beam height is shown in red. The sample holder is shown in Fig. 2.2b. It is easily removable from the sample support, by unscrewing the Be dome and pulling the holder out of the electrical connections, thus enabling rapid sample exchange (see below).

The materials that make up both the reactor and the sample holder have been chosen carefully not to be catalytically active. They can all withstand both oxygen and hydrogen at a pressure of 1 bar and a sample temperature of 950 K. The
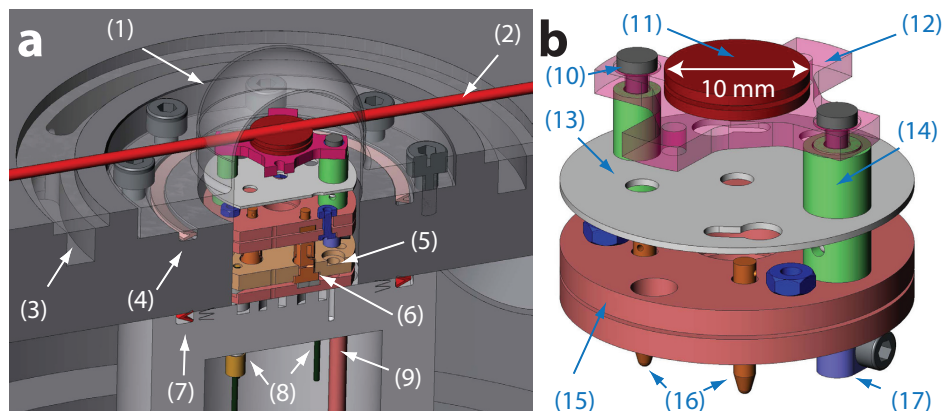
Figure 2.2: a) Top part of the setup with the top flange in the lower position and with the sample holder in the reactor part of the system. **b)** Sample holder. The labels denote: (1) beryllium dome, (2) x-ray beam height, (3) water cooling channel, (4) V-seal between the reactor and the external atmosphere, (5) alumina plate, (6) female electrical connection, (7) V-seal between UHV and high pressure in the reactor, (8) electrical feedthroughs, (9) gas entry line, (10) tungsten rod, (11) sample, (12) bora-electric heater, (13) heat shield, (14) alumina cylinder, (15) alumina plates, (16) male electrical connections, (17) stainless steel clamps.

sample is heated by a graphite heating element embedded in boron nitride [43], which is electrically and mechanically connected by two tungsten rods. These rods are clamped with stainless steel clamps from underneath the holder. Further electrical connection to the outside is made by two male/female connections and a feedthrough. The temperature of the sample is measured by a type C thermocouple (tungsten 95% rhenium 5% tungsten 74% rhenium 26%). Note, that thermocouples containing Cu, Pt or Ni cannot be used. Pt is a highly active catalyst for CO oxidation, Ni forms carbonyls with CO, resulting in Ni deposition on the sample, and Cu is an active catalyst for methanol synthesis. The thermocouple is either spot-welded to, or pressed against the sample by two clips mounted on the heater (not shown in the figure). Unfortunately, feedthroughs are not available in thermocouple material (W, Re). Feedthroughs do exist of compensation material, equivalent to a type C thermocouple. However, these contain Ni and Cu, which cannot be tolerated. Therefore, we have chosen to equip the sample holder support with stainless steels feedthroughs and calibrate the temperature drop over the feedthroughs under various operating conditions of the reactor.

The exposed hot parts of the heater are protected from oxidation by a layer of BN coating (COMBAT® Boron Nitride Coatings [44]). The sample fixation is chosen on a per-experiment basis. Usually Ta clips are used in oxidizing conditions and Mo clips in hydrogen-rich conditions. Ta is more resistant to oxidation than Mo, but will eventually also oxidise at high temperatures. Ta, however, forms hydrides in hydrogen-rich conditions, whereas Mo does not.

2.3.3 Gas System

Figure 2.3 shows a schematic drawing of the gas system. It consists of four mass flow controllers (Bronkhorst EL-FLOW, 50 ml$_n$ min^{-1} [45])* calibrated for different gasses. The common output is connected to the reactor via a flexible UHV-compatible PEEK (polyether ether ketone) tube (1.57 mm inner diameter, Sigma Aldrich [46]). A pressure controller (Bronkhorst EL-PRESS, 1200 mbar [45]) is mounted on the reactor exhaust. This geometry allows us to independently set the reactor pressure, the gas composition and the total mass flow. The pressure difference that is required to obtain a continuous flow of gas between the outlet of the mass flow controllers and the inlet of the pressure controller is determined by Poiseuille's law, approximated for an isothermal ideal gas:

$$\Phi = \frac{\pi D^4}{256 \eta L} \left(\frac{P_i^2 - P_o^2}{P_o} \right), \tag{2.1}$$

where Φ is the volumetric flow rate, D is the pipe diameter, η is the dynamic viscosity of the gas, L is the length of the pipe, and P_i and P_o are the inlet and outlet pressures respectively. In Fig. 2.3 the flow resistance between the mass flow controllers and the pressure controller is determined by the PEEK tube and the stainless steel piping to and from the reactor. The pressure difference between the mass flow controllers and the pressure controllers that is needed to maintain a 50 ml$_n$ min^{-1} flow of air through the reactor is calculated to be 10 mbar. This makes that the pressure as measured at the pressure controller is nearly equal to the gas pressure in the reactor.

The pressure controller can regulate the total pressure in the reactor from 100 mbar up to 1200 mbar. The flow controller can regulate the flow from 1 ml$_n$ min^{-1} up to 50 ml$_n$ min^{-1}. In a binary mixture of pure gasses at a total flow of

---

*1 ml$_n$ min^{-1} is defined as 1 ml at a gas temperature of 0 °C and a pressure of 1.013 bar
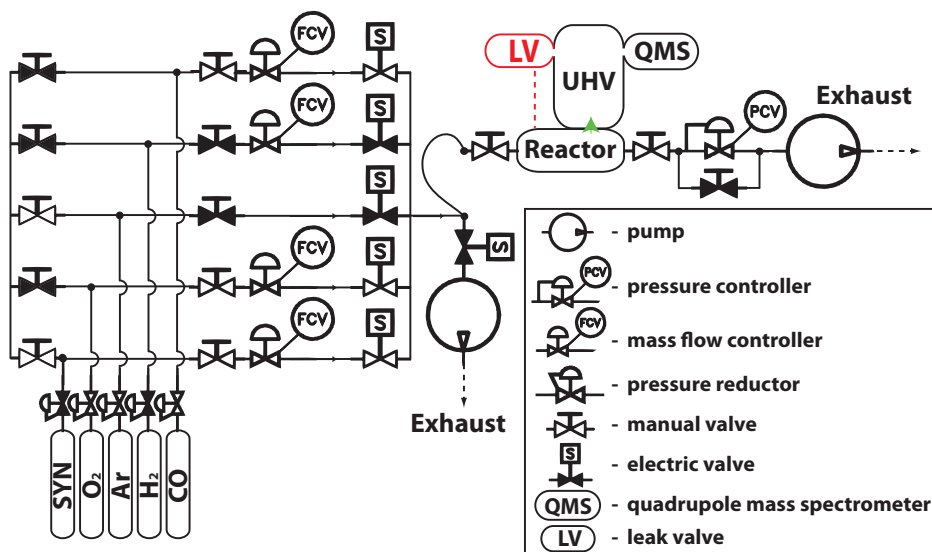
Figure 2.3: Schematic drawing of the gas system. Black valves are closed, white valves are open. In this typical configuration CO and O_2 are flowing through their respective controllers, while Argon is bypassing on the left side via the lower controller. The final mixture flows through the reactor and is pumped away by the exhaust system via a pressure controller and a scroll pump. The gas composition in the reactor is analysed by mass spectrometry. Initially a bypass line with a leak valve was designed to admit gas from the reactor to the UHV system with the mass spectrometer, but in practice we make use of a direct, tunable leak at the seal between the reactor and the UHV, symbolized here by the green arrow. A carbonyl trap is mounted optionally between the CO bottle and the CO mass flow controller.

50 ml_n min^{-1}, the lowest composition of one of the gasses in the mixture is 2%. That would for example be 1 ml_n min^{-1} of gas A mixed with 49 ml_n min^{-1} of gas B. Therefore the lowest attainable partial pressure of this gas in the reactor is 2 mbar (2% of the minimum total pressure). If necessary this value can be lowered further by using bottles which contain mixtures of gas A and gas B.

The mass flow controllers, pressure controllers, the electric valves and also the heater power supply are interfaced with SPEC, the beamline data acquisition software package [47]. This enables us to perform fully automated scanning of gas and temperature conditions and to use measurement macros with complex variations in time of all parameters, including abrupt switching of gas conditions.

All these manipulations are possible during x-ray scattering experiments, without the need to interrupt the x-ray beam. Compared to the manual gas handling on the previous batch reactor [21], this is a major improvement.

For many reactions, the catalytic conversion rate is determined by measuring the partial pressure of the reaction product by use of the QMS, in combination with accurate knowledge of the total pressure and flow in the reactor. Occasionally, however, the reaction rate will be so low that the partial pressure of the product gas is below the detection limit or below the background partial pressure of this gas in the QMS. If this is the case, the flow can be interrupted to make the reactor behave as a small batch reactor. One can then wait sufficiently long to see the partial pressure of the product increase and determine the chemical conversion rate from the rate of this increase.

2.4 Performance

The setup has been successfully tested in a number of experiments already. The results of these experiments will be published elsewhere. Here, we briefly describe the performance of several key aspects of the design and provide one example of the performance during an experiment.

2.4.1 UHV Chamber

The UHV chamber reaches a base pressure of 4×10^{-9} mbar routinely after each bake-out (24 hr at 120 °C) against the turbo-molecular pump. During reactivity measurements the temperature of the reactor wall does not exceed 333 K while the sample is at 875 K, due to the efficient water cooling on the reactor walls.

The part of the gas system that was designed to admit gas from the reactor exhaust into the UHV chamber via a leak valve was never implemented. Instead, we tune the electromotor that drives the top flange of the setup. With this, we can regulate the leak via the V-seal into the UHV, like in a leak valve. The chamber pressure can be accurately set between 10^{-9} mbar up to 10^{-3} mbar. The small leak allows for the analysis of the gas composition in the reactor with the QMS mounted in the UHV part of the chamber. A leak directly at the reactor is advantageous, because it does not introduce additional time delays or convolution effects in the detected gas composition.

2.4.2 Sample holder

With the top flange in the lower position, samples can be exchanged very quickly, e.g. within 30 min, effectively using the reactor as a load lock. In this way costly synchrotron time can be used efficiently. The base pressure for UHV sample preparation after changing sample is usually increased from 10^{-9} mbar to 10^{-8} mbar, because the reactor and the gas lines cannot be baked out separately.

A systematic error in the temperature reading of the thermocouple is made because of the temperature difference over the stainless steel feedthroughs. This systematic error was measured and carefully calibrated, resulting in an thermocouple temperature measurement accurate to within 3 K, by eliminating the systematic error.

Under UHV conditions the sample can be heated reliably up to 1500 K. In oxidizing conditions with Ta clips the sample can be heated to 950 K. Preliminary tests in which the sample was fixed to the heater by a BN coating show that the sample can reach a temperature of 1100 K in oxidizing reaction conditions. In this test the heat shield had to be removed from the sample holder as it was significantly catalysing the oxidation of methane.

2.4.3 Gas system

The lower limit of the time constant of gas composition changes in the reactor at a constant operating pressure and a constant total mass flow is given by:

$$\tau = \frac{VP_r}{F},$$
(2.2)

where V is the reactor volume, P_r is the pressure in the reactor, and F is the total mass flow through the reactor. The time constant may be longer if there are dead volumes in the reactor or the gas lines or if the gas line diameters are such that the gas in the reactor diffuses into the gas inlet and gas outlet. The reactor volume as drawn in Fig. 2.2 is calculated to be 13.3 ml. Figure 2.4 shows a decaying partial Argon pressure with a time constant of 15.8 s. On the basis of the calculated reactor volume one would expect a time constant of 12.4 s at the specified total mass flow and total pressure. We ascribe the 3.4 s difference in measured and calculated time constant to the fact that the gas in the reactor is not perfectly mixed within the characteristic refresh time. That means that part of the volume of the reactor is effectively 'dead', i.e. it is refreshed mainly by gas diffusion
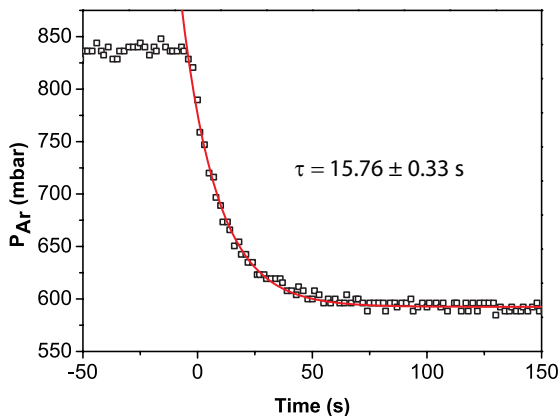
Figure 2.4: Exponential decay of the partial Ar pressure in the reactor measured by the QMS after switching the gas flow from a total rate of 64.8 ml$_n$ min^{-1} with 84.8% Ar to a flow of 59.8 ml$_n$ min^{-1} containing 58.3% Ar, while keeping the total pressure constant at 1000 mbar. The time constant of the exponential decay, τ, is determined by the fit (red line).

rather than flow or convection. The diffusion of reactor gas into the gas line is negligible, as the flow speed in the gas lines is higher than the diffusion rates of the gasses.

Similarly, the rate at which the total pressure in the reactor can change at constant flow is given by the ratio of the total mass flow and the total gas system volume, i.e. the volume of the complete system, from the mass flow controllers to the pressure controller, including the reactor and the tubing. Figure 2.5 shows the pressure evolution in time at two fixed total flows for three different pressure jumps. From these measurements, the volume of the gas system is determined to be 57.4 ± 0.6 ml. Since the intermixing of gas from the reactor into the inlet and outlet was negligible, the only disadvantage of the relatively large volume of the total gas system compared to the reactor is the introduction of a time delay between setting a new gas composition (at constant total pressure) and arrival of the gas in the reactor. At a total flow of 50 ml$_n$ min^{-1} and a total pressure of 1000 mbar the time delay is 20 ± 3 s.

The time delay in product gas detection is estimated as the time that CO_2, produced at the sample during a CO oxidation experiment, needs to diffuse through
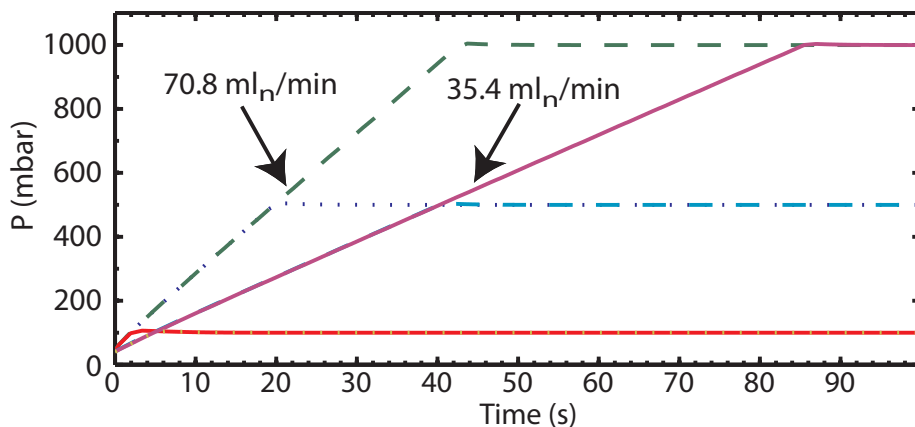
17

Figure 2.5: Reactor pressure as a function of time for different flow and pressure settings, starting from an evacuated reactor. The dashed green line, the dotted purple line and the dashed red line show the pressure evolution for a total flow of 70.8 ml_n min^{-1} of Ar up to a total set pressure on the pressure controller of 1000 mbar, 500 mbar and 100 mbar respectively. The solid purple line, the dashed blue line and the solid green line show the evolution for a flow of 35.4 ml_n min^{-1} of Ar and a total set pressure of 1000 mbar, 500 mbar and 100 mbar respectively.

the gas in the reactor to the V-seal. The diffusion length, L, is given by:

$$L = 2\sqrt{Dt}, \tag{2.3}$$

where D is the diffusion constant and t is the elapsed time. This is calculated ignoring convection and turbulence, which would mix the gasses in the reactor more efficiently and therefore make the delay in product detection even smaller. The diffusion constant of CO_2 through air at room temperature is 0.16 cm^2 s^{-1} [48]. Using above determined time constant for reactor refreshment of 15.8 s, i.e. the average residence time of a molecule in the reactor, we find a diffusion length of 3.1 cm. As the dimensions of the reactor are in the order of 3.2 cm we can be sure that the products will be relatively well mixed, except for the dead volumes in the sample holder, even in the absence of convection and turbulence. Variations of the reaction rate that occur on a timescale faster than the average residence time of a molecule in the reactor are averaged out in the gas detection.
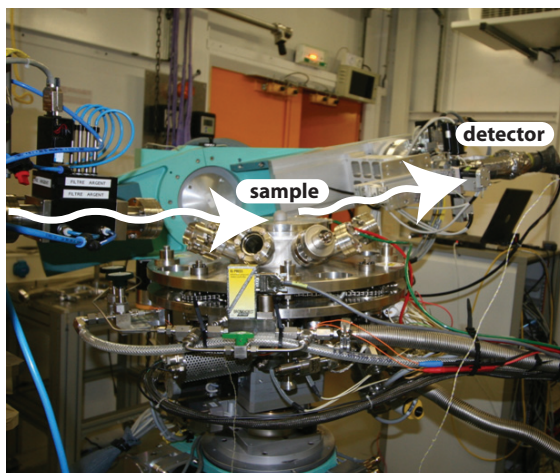
Figure 2.6: Photograph of the setup installed on the ID03 six-circle diffractometer. The x-ray beam enters from the left and photons scattered from the sample are collected in the detector (white arrows). The setup is shown in the configuration with the reactor closed, like in Figure 2.1b.

2.4.4 First Experiment

Figure 2.6 shows a photograph of the setup mounted on the six-circle diffractometer [32] at the ID03 beamline at the ESRF. During the first test experiment, a Pd(111) sample was mounted in the reactor and cleaned by cycles of 1000 V Ar$^+$ ion bombardment and annealing up to 1150 K. The sample was first aligned in UHV, i.e. with the Be dome lowered over the sample, but without the reactor closed on the seal. After this alignment, the reactor was fully closed and the alignment of the sample was checked.

Figure 2.7a shows that the vertical position of the sample moves down by 27 μm as a result of the force applied on the sample holder support. Also a minor tilt of the crystal of 0.03° was observed. Figure 2.7b shows the variation in vertical position of the sample upon heating. The vertical position of the sample moved up by 28 ± 8 μm, due to thermal expansion of the sample and sample holder. The loss of intensity at 260 °C is caused by a slight accompanying tilt of the crystal by 0.05°. After cooling down, the sample returned to its original, aligned orientation. The alignment is remarkably stable and only modest refinements are necessary when performing experiments over a large temperature range
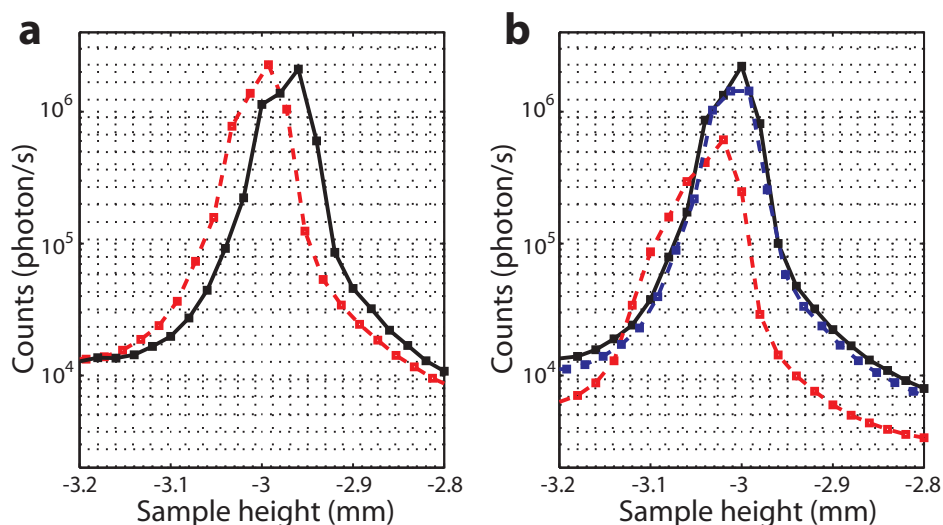
Figure 2.7: a) alignment of the vertical position of the sample surface with the detector at an anti bragg position of a Pd(111) crystal truncation rod (CTR), with the sample in UHV, .i.e. with the reactor open (red) and with the sample in the closed reactor (black). **b)** alignment of the vertical position of the sample surface on a surface peak at room temperature in UHV, before heating (black) and after heating and cool-down (blue) and hot at 260 °C (red).

of several hundreds of degrees.

In a later stage a Pd(100) sample was mounted. The surface was cleaned by cycles of 1000 V Ar^+ ion bombardment and annealing up to 1150 K. The surface was subsequently oxidized in a mixture of 50% O_2 and 50% Ar at a total pressure of 1200 mbar and a temperature of 456 K. A bulk-like PdO structure, like the one reported in ref. [49], was found to be present on the surface. The oxide was reduced again by removing O_2 from and adding CO to, the mixture. Afterwards a gas mixture was flown through the reactor containing 50% O_2 and variable amounts of Ar and CO. The experiment was performed at a constant temperature of 456 K and a total pressure of 1200 mbar. A typical example of the data that was obtained in this experiment is shown in Fig. 2.8. A characteristic peak showing the presence of the bulk-like PdO is monitored as a function of time while the partial CO pressure in the reactor is varying and while the rate of CO_2 production is measured simultaneously. The presence of a bulk-like oxide on the Pd(100)
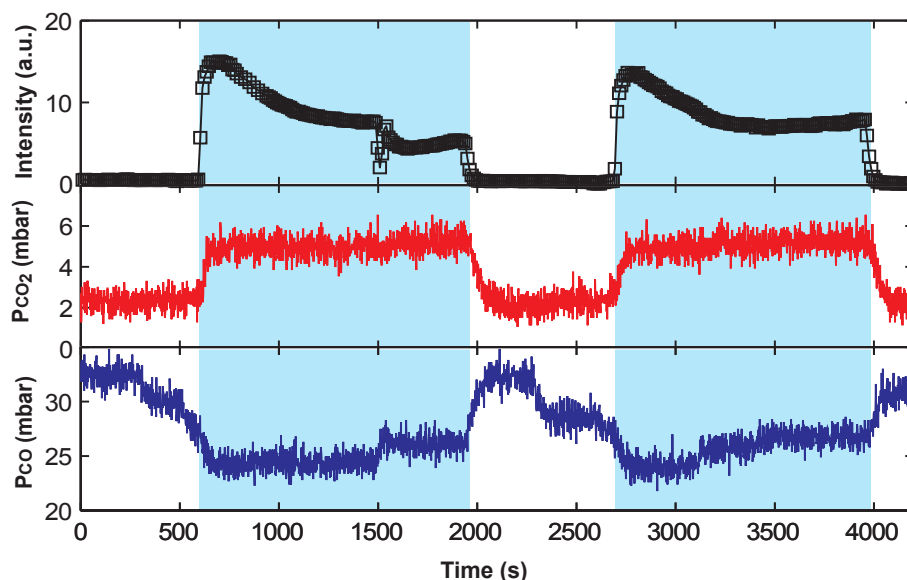
Figure 2.8: Simultaneous measurement of the intensity of a characteristic PdO diffraction peak (top panel) and the CO_2 production (red line, middle panel) in a CO oxidation experiment on the Pd(100) surface. The CO partial pressure was varied during this experiment (bottom panel), while a compensating amount of inert Ar was mixed in. in this way, the total flow (50 mln/min), the partial oxygen pressure (600 mbar), and the total pressure (1200 mbar) in the reactor were kept constant during the experiment. The sample temperature was 456 K. A high value for the CO_2 production rate can be observed simultaneous with the presence of the PdO signal (light blue regions).

surface is shown to correlate with a high CO_2 production rate. This result is in full agreement with previous results obtained in SXRD and STM [50, 51].

The new setup has also been successfully used for GISAXS experiments on oxide-supported Pd nanoparticles. The results of these experiments are shown in Chapter 5.

2.5 Additional Possibilities

The flexible and open design of the new flow setup allows for the integration of other surface sensitive techniques. The beryllium dome can be replaced by a

custom shape made in any material that is transparent to x-rays and suitable as a reactor wall. This opens the possibility to combine the x-ray scattering/diffraction experiments with in situ AFM or IR spectroscopy. The setup, being easily transportable, can in principle be used on other beamlines, specialized on other x-ray techniques, for example EXAFS. The setup has become commercially available from Leiden Probe Microscopy [52].

Chapter 3

Surface structure and reactivity of Pd(100) during CO oxidation near ambient pressure

The surface structure of Pd(100) during CO oxidation was measured using a combination of a flow reactor and in situ surface x-ray diffraction coupled to a large-area 2-dimensional detector. The surface structure was measured for P_{O_2}/P_{CO} ratios between 0.6 and 10 at a fixed total gas pressure of 200 mbar and a fixed CO pressure of 10 ± 1 mbar. In conjunction with the surface structure the reactivity of the surface was also determined. For all P_{O_2}/P_{CO} ratios the surface was found to oxidise above a certain temperature. Three different types of oxides were observed: the $(\sqrt{5} \times \sqrt{5})R27°$ surface oxide, an epitaxial layer of bulk-like PdO, and a non-epitaxial layer of bulk-like PdO. As soon as an oxide was present the reactivity of the surface was found to be mass transfer limited by the flux of CO molecules reaching the surface.

3.1 Introduction

Detailed knowledge of the atomic structure of catalytically active surfaces under operating conditions is of paramount importance for the full understanding of heterogeneous catalysis on the atomic scale. Since a real catalyst is a complex combination of materials working under high-temperature and high-pressure conditions, it is difficult to measure the surface structure of the active part of the catalyst and thus to obtain an atomic scale understanding of the catalytic process in a straightforward way. Instead, single-crystal surfaces have been used as model systems resulting in significant insight in adsorbate-adsorbate and adsorbate-substrate interactions, especially under ultrahigh vacuum (UHV) conditions [13].

Thanks to a growing number of available experimental techniques developed to study surfaces in ambient pressure environments, atomic scale insight is nowadays also obtained under semi-realistic operating conditions [14, 16, 23]. Examples of techniques bridging the so-called pressure gap are transmission electron microscopy (TEM) [53], high-pressure scanning tunnelling microscopy (STM) [54], x-ray photoelectron spectroscopy (XPS) [55], sum frequency generation (SFG) [56], and surface x-ray diffraction (SXRD) [57]. Each of these techniques has different abilities in probing either the reactants on the surface or the surface structure of the active catalytic material. SXRD is inherently sensitive to the atomic scale surface structure, also at gas pressures beyond several bars, making it an excellent technique to study phase changes in the catalyst under realistic reaction conditions.

Pd is an important oxidation catalyst, e.g., in the cleaning of automotive exhaust gases and in methane combustion [58, 59]. Modern low-fuel-consumption automotive engines operate under oxygen excess, resulting in oxygen-rich exhaust gases reaching the Pd-based catalyst, which has increasingly motivated studies of the oxidation of Pd under these oxygen rich conditions.

It has been shown that two different oxide phases may form on the Pd(100) surface, depending on the pressure and temperature conditions. One phase is a well-ordered purely 2-dimensional (2D) structure, the $(\sqrt{5} \times \sqrt{5})R27°$ phase and the second a 3D epitaxial bulk-like PdO film [49, 60–66]. The experimental determination of the surface phase diagram in pure oxygen indicates that the surface oxide kinetically hinders the formation of the bulk oxide at low temperatures [67]. It was also shown experimentally that the appearance of oxide structures

coincides with an increase in activity of the surface towards CO oxidation as compared to the reactivity on the non oxidized surface [51]. DFT calculations confirm the stability and the activity towards CO oxidation of PdO [68, 69] and the $(\sqrt{5} \times \sqrt{5})$R27° surface oxide [70, 71]. The thermodynamic phase diagram as calculated by DFT shows that under the experimental pressure and temperature conditions applied in this study the thermodynamically stable phase is the $(\sqrt{5} \times \sqrt{5})$R27° surface oxide, whereas bulk PdO only becomes the thermodynamically stable phase at extremely high P_{O_2}/P_{CO} ratios [70]. Moreover the bulk-like PdO layer was shown to play an important role in spontaneous reaction oscillations [72]. However the recent suggestion that the CO oxidation reaction is most efficient, even 'hyperactive', when the surface is in a metallic state that is transient in nature [73], provoked a lively discussion [74–76].

Here we present a high-pressure SXRD study mapping out the structure of the Pd(100) surface under various mildly to very oxidizing P_{O_2}/P_{CO} ratios and different temperatures, realistic conditions for CO oxidation. A combination of a flow reactor and in situ SXRD employing a 2D pixel detector was used. The experiments were conducted under steady state flow conditions, ruling out any transient effects. This allowed us to map out the stability of the metallic Pd(100) surface and the oxide phases under the variety of gas pressures and temperature conditions and under the influence of the catalytic reaction. The mapping resulted in a concise diagram that will be compared to theoretical predictions and other experimental data. In addition to the surface structure we also monitored the CO_2 production at each point in the phase diagram. We observe the highest CO_2 production when an oxide phase is present on the Pd(100) surface. Conclusions about differences in the reactivity of the different oxides could not be drawn and we will explain that this is due to limitations of mass transfer of CO to the sample.

3.2 Experimental methods

The experiments were carried out at the ID03 beamline of the European Synchrotron Radiation Facility (ESRF) [77]. The beamline is equipped with a combined UHV-high pressure flow setup that can be mounted on a six-circle diffractometer [78]. This setup allows for the cleaning of samples in UHV combined with flow experiments in a 13 ml flow cell at reactant pressures up to 1200 mbar.

A beryllium dome functions as part of the reactor wall allowing for entrance and exit of the x-rays. The sample was subjected to several cycles of 1000 eV Ar^+ ion bombardment for 45 minutes and annealing up to 1300 K for 10 minutes. A focused x-ray beam of 18 keV (2×10^{12} photons/s, 80 mA ring current) impinging on the surface under a 1° incidence angle was used for the diffraction experiments. We describe the Pd crystal lattice with a tetragonal unit cell with two vectors in the surface plane ($|\vec{a_1}| = |\vec{a_2}| = a_0/\sqrt{2}$) and one perpendicular to the surface plane ($|\vec{a_3}| = a_0$) where $a_0 = 3.89$ Å. A maxipix 2D pixel detector was used to collect the diffracted x-rays [79–81], allowing for the detection of an area of reciprocal space without having to scan the detector. Each image required less than one second of exposure time and a readout time of 0.29 ms.

A ball model of the two oxide structures is shown in Fig. 3.1a. The ($\sqrt{5} \times \sqrt{5}$)R27° phase is described in ref. [61] as a 2D structure, i.e. a single oxide layer, which is essentially a distorted PdO(101) plane. The bulk-like PdO structure usually grows 2-3 nm thick under our experimental conditions with the PdO(101) plane epitaxial to the Pd(100) surface and is thus a 3D structure [49, 62, 64].

One domain of the in-plane reciprocal lattices of both oxide structures is shown in Fig. 3.1b. Due to the p4mm symmetry of the Pd(100) surface and the pm symmetry of the oxide phases, eight domains of orientation of both oxide phases exist on the Pd(100). From Fig. 3.1b one sees that both structures have diffraction features at the (0.4, 0.8, L) and equivalent positions in reciprocal space . Due to the 3D nature of the PdO overlayer one expects a diffraction peak in the L directions at the (0.4, 0.8, 0.74) position of the Pd(100) reciprocal lattice [67]. By choosing this position for the 2D detector we record a region on the Ewald sphere around this position, see Fig. 3.2a. If the 2D ($\sqrt{5} \times \sqrt{5}$)R27° structure is present, we expect no peaks along the L direction, but rather a truncation rod of slowly decaying intensity as L is increasing. Figure 3.2b,c show the characteristic signal of the different oxide phases on the detector, confirming these expectations. Note that the peak in Fig. 3.2c for the bulk-like oxide is extended in the L direction compared to the field of view of the 2D detector due to the fact that the layer is just nanometers thick. Under some conditions a third phase was observed consisting of a regular PdO layer that had partially lost its epitaxial orientation to the surface, resulting in PdO powder ring diffraction on the detector, as shown in Fig. 3.2d.

The stability diagram was determined as follows. The clean sample was exposed to a flow as 50 mln/min consisting of a mixture of CO, O_2 and Argon at
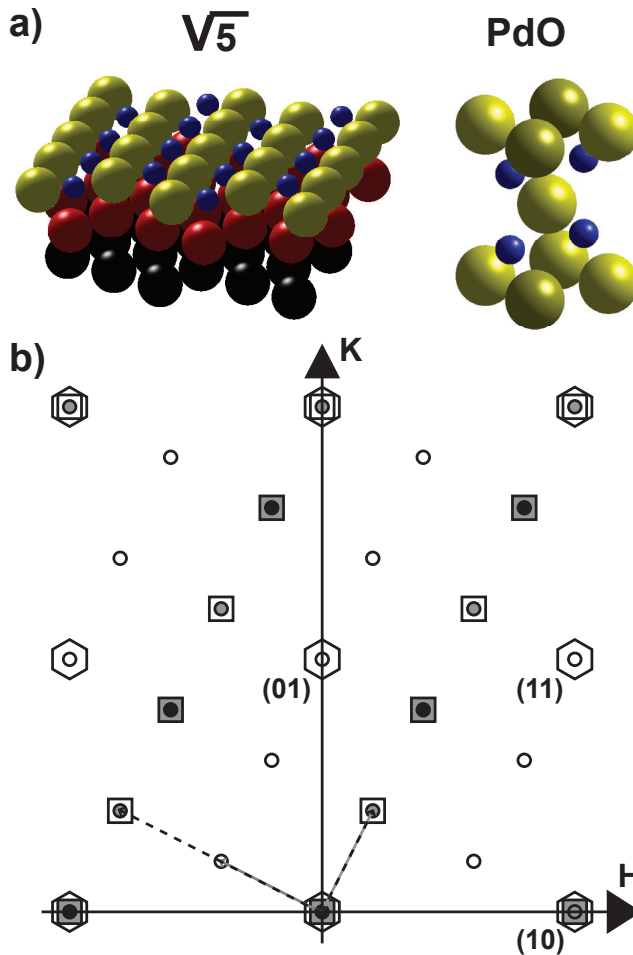
Figure 3.1: a) Left: Ball model of the $(\sqrt{5} \times \sqrt{5})R27°$ phase, blue balls indicate O atoms, yellow, red and black are the first second and third layer of Pd atoms, respectively. Right: Bulk PdO unit cell, blue balls indicate the O atoms and yellows balls indicate Pd atoms.**b)** In-plane reciprocal lattice expressed in reciprocal lattice units of the Pd(100) surface unit cell. Hexagons denote the in-plane reciprocal lattice positions of Pd truncation rods, squares denote the in plane reciprocal lattice of PdO with the PdO(101) face epitaxial to the Pd(100) surface (filled grey squares indicate truncation rods with high intensity reflections, empty squares indicate truncation rods with lower intensity reflections), circles show the in plane reciprocal lattice of the $\sqrt{5} \times \sqrt{5})R27°$ phase (open circles denote negligible intensity, filled grey circles denote measurable intensity, filled black circles show the strongest intensity)
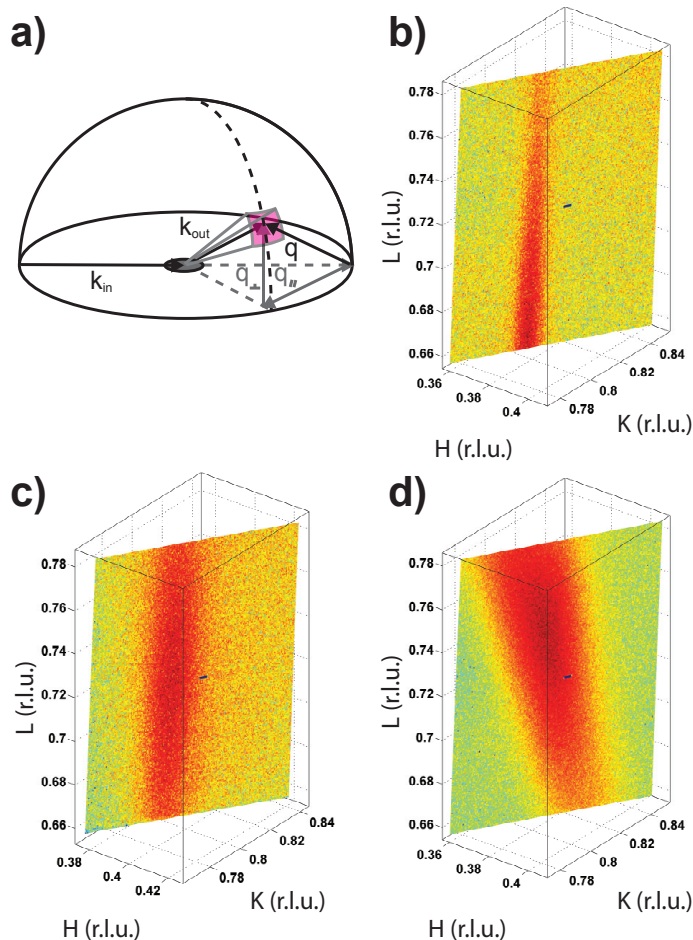
Figure 3.2: a) Surface x-ray diffraction geometry. Note that a spatially resolved diffraction signal is recorded over part of the Ewald sphere by using a 2D detector [81]. The specific cut that the detector makes in reciprocal spaces depends on the incoming X-ray wavelength (radius of the Ewald sphere) and the position of the detector. **b)** Typical intensity profile on detector signifying the presence of the $(\sqrt{5} \times \sqrt{5})R27°$ phase, the peak has a small FWHM in the HK plane, indicating the long range order in the plane. **c)** Typical intensity profile associated with an epitaxial bulk-like PdO(101) layer. The relatively broad peak indicates this structure is less well ordered than the $(\sqrt{5} \times \sqrt{5})R27°$ phase. **d)** Intensity profile of a bulk-like PdO(101) layer that partly lost epitaxy to the underlying surface. The H, K, and L coordinates are expressed in reciprocal lattice units (r.l.u.) of the underlying Pd(100) surface.

a pressure of 200 mbar, while being heated to the desired temperature. The partial pressure of CO, P_{CO} was kept constant at 10 ± 1 mbar. The Argon and O_2 pressures were varied to obtain the desired P_{O_2}/P_{CO} ratio, while keeping the total pressure constant. The total pressure was kept constant using Argon to keep the diffusion constant of CO and the heat conduction properties of the gas stream as constant as possible over the whole range of experimental conditions. The surface was allowed to stabilize for several minutes while the diffraction features at the (0.4, 0.8, 0.74) were monitored. Upon obtaining a stable structure, the gas flow was stopped, effectively turning the flow reactor into a batch reactor. The initial slope of the increase of the signal at a mass of 44 amu (the mass of CO_2) in the quadrupole mass spectrometer (QMS) was used to determine the reaction rate of the sample. Subsequently the flow was started again with $P_{CO}=P_{Ar}=100$ mbar and $P_{O_2}=0$ mbar to reduce any oxides that might have formed. After confirming that any oxides were reduced, the experiment was repeated for other P_{O_2}/P_{CO} ratios and temperatures.

3.3 Results and discussion

Figure 3.3 shows the resulting stability diagram. By comparing the diffraction features in the image with the three examples in Fig. 3.2, several trends can be observed. First of all the black line marking the metal/oxide stability boundary slopes to the right, i.e. at lower temperature one needs a higher P_{O_2}/P_{CO} ratios to form an oxide on the surface. Second, the $(\sqrt{5} \times \sqrt{5})R27°$ surface oxide forms at high temperatures and low P_{O_2}/P_{CO} ratio, while at higher P_{O_2}/P_{CO} ratios the bulk-like PdO oxide forms. This observation is in agreement with studies using pure oxygen to oxidise the Pd(100) surface [67]. However DFT indicates that the bulk-like oxide should not be observed at all under the present conditions [70]. We speculate that this discrepancy is due to the reaction-induced roughness [72] that may locally stabilize the bulk oxide under conditions for which on a flat surface the $(\sqrt{5} \times \sqrt{5})R27°$ structure would have the lower energy. Third, the surface tends to form a relatively perfect structure (small FWHM of the peak in the image) $(\sqrt{5} \times \sqrt{5})R27°$ at low P_{O_2}/P_{CO} ratios and high temperatures. The FWHM of the oxide is relatively large at high P_{O_2}/P_{CO} compared to lower P_{O_2}/P_{CO} ratios, showing that there is only short-range order present in this PdO layer. In addition, at high P_{O_2}/P_{CO} ratios a PdO film is formed that partly
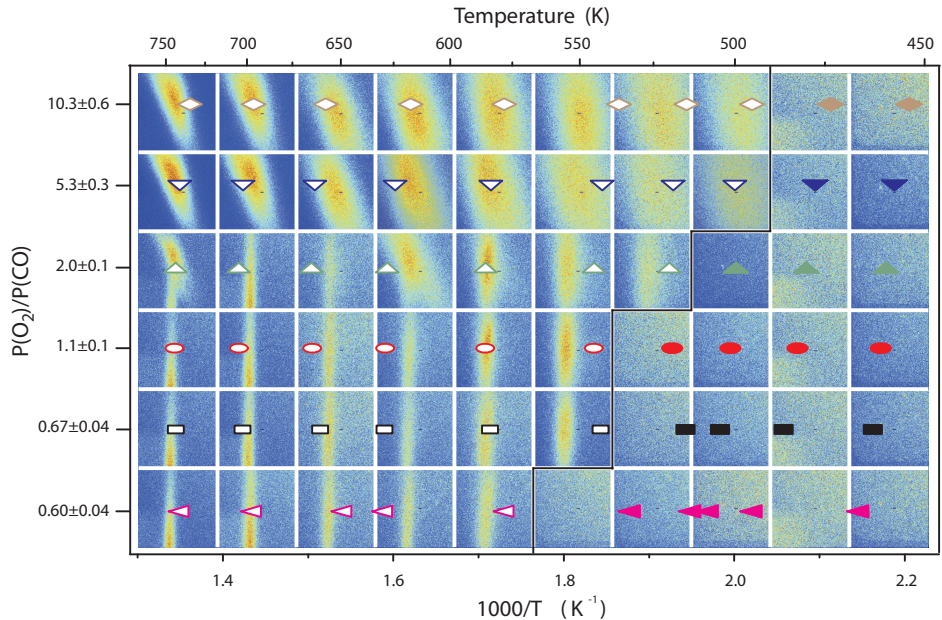
Figure 3.3: Recorded diffraction signal as a function of P_{O_2}/P_{CO} ratio and sample temperature. The total gas pressure in the reactor was kept constant at 200 mbar, the partial CO pressure was kept constant at 10 ± 1 mbar. Oxygen and Argon where mixed in the flow to obtain the desired P_{O_2}/P_{CO} ratio. The different oxides signals introduced in Fig. 3.2 can be recognized. The overlaying symbols indicate the precise temperatures at which the underlying images were obtained. The corresponding values for the CO_2 production are plotted using the same symbols in Fig. 3.4. Open symbols denote the presence of an oxide, filled symbols denote that the surface was metallic in nature. The thick black line indicates the boundary between the metallic and oxidic phases.

lost epitaxy to the substrate. The fact that the $(\sqrt{5} \times \sqrt{5})R27°$ structure exhibits a well-ordered 2D structure while the bulk PdO oxide is poorly ordered is in agreement with previous oxidation studies [64, 65]. Fourth, we clearly observe the coexistence of the $(\sqrt{5} \times \sqrt{5})R27°$ structure and the bulk-like PdO film that lost epitaxy to the surface for example at T=750 K and T=625 K and P_{O_2}/P_{CO}=2 in Fig. 3.3. The gradual transition from the epitaxial bulk-like oxide of Fig. 3.2c to the $(\sqrt{5} \times \sqrt{5})R27°$ of Fig. 3.2b that can be seen in the stability diagram in Fig. 3.3 in the range $600 < T < 650$ and $P_{O_2}/P_{CO} \leq 1.1$ is evidence for the coexistence of these two phases in that pressure and temperature range. The phase
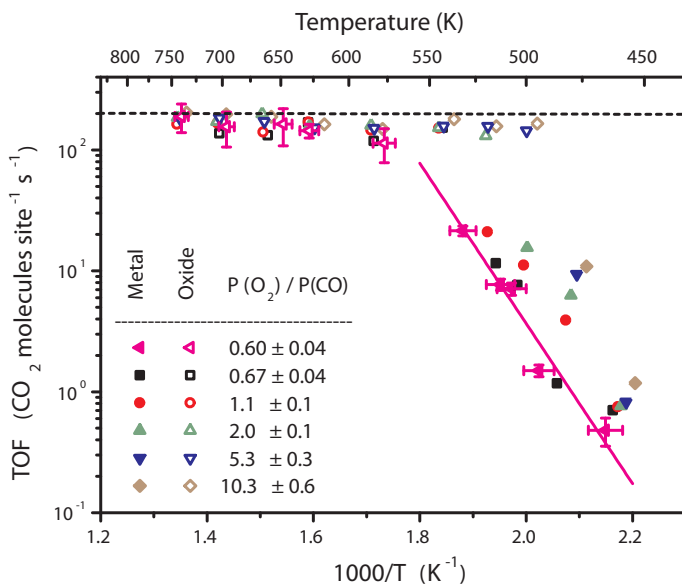
Figure 3.4: Arrhenius plot of the CO_2 production rate over Pd(100) at different P_{O_2}/P_{CO} ratios. The total gas pressure in the reactor was kept constant at 200 mbar, the partial CO pressure was kept constant at 10 ± 1 mbar. Oxygen and Argon where mixed in the flow to obtain the desired P_{O_2}/P_{CO} ratio. Representative error bars and a fit of the Arrhenius behavior are shown for the P_{O_2}/P_{CO}=0.6 data set. The surface structure was determined simultaneously with the TOF by surface x-ray diffraction. Open symbols denote where the SXRD measurements showed the presence of an oxide (surface oxide, bulk-like oxide, or powder pattern) and solid symbols indicate under which conditions SXRD measured an oxide-free metal surface.

coexistence is likely not a pure thermodynamical coexistence, but may extend over a large range due to the presence of kinetic effects (reduction of PdO by CO, diffusion, kinetic hindrance). Also note that for higher temperatures ($\sim$1100 K) than obtainable in this study one would expect the oxides to become thermodynamically unstable again, even in the presence of pure oxygen.

The turnover frequency (TOF) corresponding to the data in Fig. 3.3 are shown in Fig. 3.4 in Arrhenius form. The data splits up into two sets of data points. The first set are the filled symbols were the surface was metallic in nature and the TOF increased with increasing temperature. The second set are the open symbols were the TOF has reached a plateau and does not vary with temperature. The

activation energy on the metal, as determined from the slope of the Arrhenius plot for the P_{O_2}/P_{CO} ratio of 0.6, is 1.32 ± 0.16 eV, in agreement with the value found previously [82]. The data also shows that the TOF was always at the maximum when the surface was oxidized. Our diffusion calculations indicate that the reactivity in this regime was not determined by the intrinsic reactivity of the catalyst, but by the rate at which reactant molecules could be supplied to the catalyst, i.e. by the mass transfer limitation (MTL) of the flow reactor. A first-principles calculation confirms the importance of heat and mass transfer effects [83]. Since our P_{O_2}/P_{CO} ratio was larger than 0.5 and almost all the CO is consumed once the TOF reaches the MTL, the P_{O_2}/P_{CO} ratio at the sample was higher than what was set upstream. This effect is always present, but can be mitigated to a small extent by using small samples, a large flow, or by mixing the gas in the reactor efficiently. Our efforts to increase the flux of CO molecules impinging on the surface by reducing the sample size from a 7 mm diameter to a 1 mm diameter resulted in an oxidation of the surface at a $\sim$50K higher temperature. The MTL was reached again for this small sample as soon as an oxide was present on the surface. The exact conditions under which the sample oxidises thus moderately depend on sample size via the MTL associated with this sample size. This raises the question if the oxidation is the *cause* of the higher reactivity or merely the *effect* of the changing P_{O_2}/P_{CO} ratios at the surface as the temperature is increased and the metallic surface becomes more reactive. The present data does not allow us to directly conclude either way, but we may conclude that all oxides were reactive enough to sustain a mass transfer limited TOF. Since the gas conditions at the sample are net oxidizing the oxide is the thermodynamically stable termination of the Pd(100) surface, as confirmed by DFT calculations [71]. We therefore think it is highly unlikely that any other non-oxidic phase (chemisorbed oxygen, bare metal) would still be present under these conditions, and be responsible for the observed reactivity.

Our observation of the $(\sqrt{5} \times \sqrt{5})$R27° structure at P_{O_2}/P_{CO} ratios from .6 to 1.1 in the stability diagram supports the theoretical predictions that this phase is indeed stable up to stoichiometric reactant feeds [70, 71]. This observation is at odds however, with the claimed absence of the surface oxide in IRAS experiments under similar gas and temperature conditions [73, 76]. This discrepancy raises the question if the $(\sqrt{5} \times \sqrt{5})$R27° phase can be clearly observed in IRAS experiments, either indirectly through the stretch frequency of adsorbed CO or directly through a perpendicular component of the Pd-O vibration, a question also

asked by the authors of ref. [76]. The fact that our CO_2 production is mass transfer limited when the $(\sqrt{5} \times \sqrt{5})R27°$ phase is present supports the prediction that this phase is 'clearly not 'inactive'' towards CO oxidation' [71]. The high activity of all the observed oxide phases is in line with recent DFT calculations activation energies and efficient reaction pathways on various terminations of PdO [69].

In summary we have shown that the Pd(100) surface oxidizes above a certain temperature under reaction conditions at all P_{O_2}/P_{CO} ratios between 0.6 and 10 at a total gas pressure of 200 mbar. The 2D detector used in our SXRD measurement allowed for relatively fast mapping of reciprocal space, enabling a structural separation between surface, bulk-like and non-epitaxial Pd oxides. Although these oxides appear more reactive than a metallic Pd(100) surface, the MTL of our experimental setup inhibits the detection of differences in the reactivity of the oxides. The good agreement between experimental and theoretical studies however supports a high activity for CO oxidation on the PdO surface.

Chapter 4

Spontaneous reaction oscillations on Pd(100): a new role for steps in catalysis

Atomic steps at the surface of a catalyst play an important role in heterogeneous catalysis, for example as special sites with increased catalytic activity. Under the influence of the reactants, entirely new structures may form at the catalyst surface under reaction conditions. These may dramatically influence the reaction, by poisoning it or by rather acting as the catalytically active phase. For example, thin metal oxide films have been identified to be highly active structures that form spontaneously on metal surfaces during the catalytic oxidation of carbon monoxide. Here we present operando surface x-ray diffraction experiments on a palladium surface during this reaction, which reveal that a high density of steps strongly alters the stability of the thin, catalytically active palladium oxide film. We show that this new stabilizing and destabilizing role of steps is at the heart of the well-known reaction rate oscillations during CO oxidation at atmospheric pressure.

4.1 Introduction

Atomic steps on catalyst surfaces are often considered as special, active sites for heterogeneous catalytic reactions [84]. Due to their reduced coordination, step sites can offer enhanced binding of reactant molecules [12, 85, 86] and exhibit enhanced activity for bond breaking [87–90]. Catalytic nanoparticles contain a high density of steps and the steps may dominate their activity. Steps also play a key role in many other surface processes, for example as the natural locations for crystal growth and erosion and as the source for mobile surface adatoms. In this chapter, we show that steps on surfaces may play a role in catalysis not only by serving as active sites, but also by changing the stability of the catalytically active phase.

Recent experiments and theory show that oxides form on the surface of precious metal catalysts such as Ru, Pt, Pd and Rh during oxidation catalysis at atmospheric pressure under oxygen-rich conditions [14, 23, 67, 91, 92]. Experiments performed under these conditions using operando techniques, which simultaneously provide information on the state of the catalyst and on the reaction kinetics, indicate that these oxides are catalytically more active than the bare metal surfaces [23, 91], although this is still the subject of ongoing debate [73]. The reason for the formation of the oxides is simply that at high oxygen pressures it is thermodynamically more favourable to incorporate oxygen atoms in the surface in oxygen-rich phases (oxides) than in the low-coverage chemisorption structures typical for low oxygen pressures.

Whether a catalyst operating in an oxidizing mixture of reactants prefers a mere chemisorption structure or an oxide [70, 92] depends on the partial pressures of the reactants. The transition of the catalyst surface from the metal phase to the oxide phase dramatically changes the catalytic reaction mechanism. Whereas on the metal surface both reactants first adsorb and then react to form the product (Langmuir-Hinshelwood mechanism), the more active oxidized surface serves as an intermediate product from which oxygen atoms are easily extracted by the other reactant (for example CO) after which the resulting oxygen vacancies are refilled with oxygen from the gas phase. This is similar to the Mars-Van Krevelen mechanism, in which gas molecules react with the lattice oxygen from the metal oxide to form the product while the redox process is completed by oxygen that diffuses through the oxide to fill up the oxygen vacancies that are caused by this reaction [10].

Previously we found that reaction rate oscillations can occur during CO oxidation under conditions where both the oxide and the metal phase can exist [51, 93]. Spontaneous and self-sustained oscillations in the rate of CO oxidation have been extensively studied both at low pressures (e.g. 10^{-6} mbar) and at atmospheric pressure [94, 95]. The low-pressure oscillations are due to atomic-scale restructuring of the surface of a catalyst (e.g. Pt or Pd) or the formation of a subsurface oxygen layer, as was shown beautifully in the work of G. Ertl et al [94]. By contrast, our earlier in situ scanning tunneling microscopy studies show that at atmospheric pressure the oscillations in the reaction rate are due to the spontaneous, periodic switching from a low-activity metal surface to a high-activity oxide surface [51, 93]. In this chapter we show that there is an important influence of the step density (roughness) on the stability of the metal and oxide phases of the catalyst's surface and that the steps thereby regulate the self-sustained reaction oscillations during CO oxidation on Pd(100) at atmospheric pressure.

4.2 Results

Figure 4.1 shows that the CO_2 production rate and the CO pressure inside a flow reactor spontaneously oscillated under steady state conditions and a constant feed of CO and O_2. The CO pressure oscillated in anti-phase with the CO_2 pressure as a result of the varying CO consumption in the reaction, which for the high rate is mass transfer limited [93]. Figure 4.1 shows surface x-ray diffraction (SXRD) data of the (h, k, l) = (1, 0, 2) diffraction peak of Pd(100) during oscillating CO oxidation at 447 K and $P_{CO} = 25$ mbar and $P_{O_2} = 500$ mbar in a 17 ml flow cell. The details of the experiment are given in the Methods section and the Supplementary Information. Movies are available online that show the oscillatory variations in the SXRD signals and the partial pressures of the reactant and product gasses (Supplementary Movie S1 and S2 of [72]).

In the low-reaction-rate phase ($P_{CO_2} = 2$ mbar) there was high intensity at the (h, k, l) = (1, 0, 2) diffraction peak, which shows that the surface was metallic. The inverse value of the full width of the diffraction peak at half the maximum intensity, $\mathrm{FWHM}_{\mathrm{metal}}^{-1}$, increased with time during this part of each oscillation. In the metal phase the $\mathrm{FWHM}_{\mathrm{metal}}^{-1}$ is a direct measure of the smoothness of the surfaces, in terms of the average terrace width, or, equivalently, the inverse of the step density [96]. The increase in $\mathrm{FWHM}_{\mathrm{metal}}^{-1}$ shows that the surface smoothened
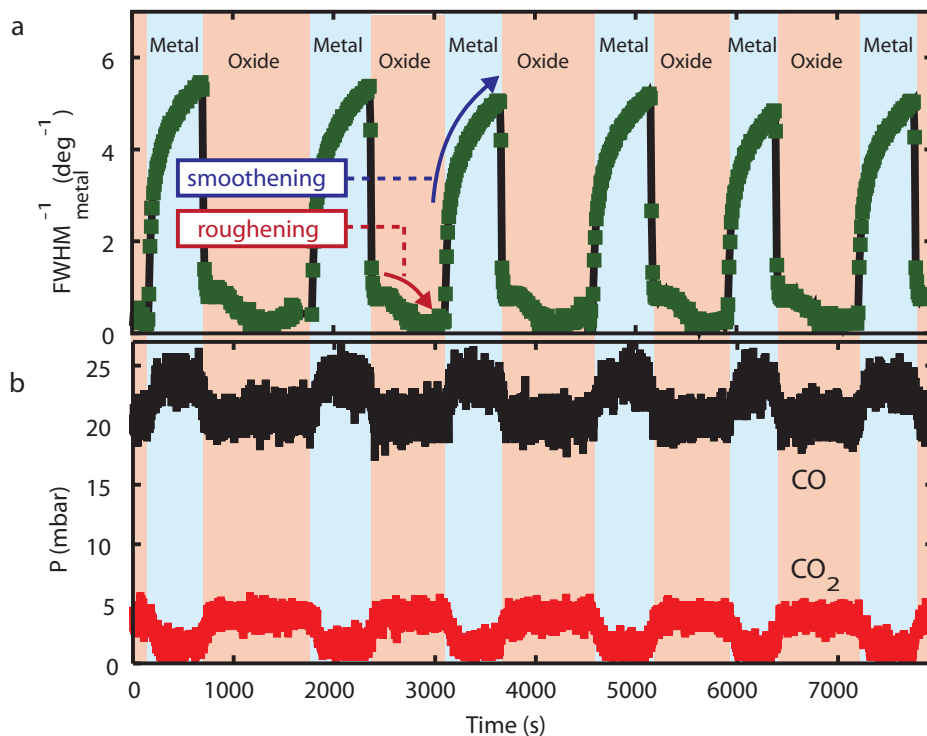
Figure 4.1: Spontaneous oscillations in the CO oxidation rate on Pd(100) as measured by SXRD and mass spectrometry. Measurements were performed at a temperature of 447 K in a constant flow of a $CO/O_2/Ar$ gas mixture with an oxygen pressure of 500 mbar, an argon pressure of 675 mbar and a CO pressure of 25 mbar flowing at 50 ml_n min^{-1}. **a)** The $FWHM_{metal}^{-1}$ (inversely proportional to the step density and a measure of the smoothness of the surface) of the diffraction peak at (h, k, l) = (1, 0, 2). **b)** The partial pressure in the reactor of CO and CO_2 pressures as measured by mass spectrometry. At high CO partial pressures P_{CO}, the diffraction pattern shows that the surface structure is close to a bulk-like truncation of the Pd crystal (the reaction kinetics indicate that this metal surface is covered by a mixture of O atoms and CO molecules). At low P_{CO}, new diffraction peaks are found that correspond to a thin PdO(101) layer (e.g. (h, k, l) = (0.8, 0.4, 0.73) see Fig. 4.4). The colors indicate whether the SXRD intensities identify the Pd(100) surface to have a metal structure (light blue) or to be covered by a thin oxide film (light red).

by reducing its step density until the transition to the high-reaction-rate state occurred ($P_{CO_2} = 4.5$ mbar) and the Pd(100) (1, 0, 2) diffraction peak practically disappeared.

After the transition we observed a new diffraction peak at (h, k, l) = (0.8, 0.4, 0.73) (Fig. 4.4, Movie S2 of [72])), which we have determined to correspond to the presence of a 1.9 ± 0.5 nm thick PdO(001) film, similar to what has been found for Pd(100) in pure oxygen [49]. Additional, high-speed SXRD measurements show that this oxidation starts with the abrupt appearance of an ultrathin surface oxide with the well-known $(\sqrt{5} \times \sqrt{5})$R27° periodicity [49], which is replaced after typically 5 seconds by the epitaxial, bulk-like PdO film. The diffracted PdO intensity increased during ~ 7 seconds, which probably signifies the lateral closing of the bulk like PdO layer.

After this ~ 7 s period, the oxide layer thickness exhibits a power-law growth ($L \propto t^p$) with an exponent of $p = 0.28$ [97]. The transition to the high reaction rate coincided with the introduction of the $(\sqrt{5} \times \sqrt{5})$R27° structure and remained unchanged as the PdO film formed. In the oxide phase the $\text{FWHM}_{\text{metal}}^{-1}$ of the (low) intensity at (1, 0, 2) that remained is a measure of the smoothness of the interface between the metal Pd(100) substrate and the PdO(001) film covering it. The fact that the $\text{FWHM}_{\text{metal}}^{-1}$ decreased with time shows that the interface became rougher. The evolution of the PdO(101) (h, k, l) = (0.8, 0.4, 0.73) diffraction peak (that is, $\text{FWHM}_{\text{oxide}}^{-1}$) is shown in Fig. 4.4 and movie S2 in ref. [72].

The roughening in the oxide phase and the smoothing behaviour in the metal phase observed with SXRD are consistent with our high pressure scanning tunneling microscopy observations [93] (see Supplementary Information). Our interpretation is that during the Mars-Van Krevelen redox reaction on the oxide a small fraction of the metal atoms in the oxide becomes sufficiently strongly undercoordinated with oxygen to become mobile and diffuse out of their original positions until they are re-oxidized and immobilized on top of the oxide [14, 91]. The lack of mobility of the oxide at the low operation temperature prevents the resulting roughness from decaying before further roughness is added by the same process. As a result, roughness gradually accumulates, approximately linearly with the total amount of produced CO_2. In the metallic phase we observe high surface mobility and the reaction does not cause further roughening, so that the surface roughness decays with time.

When we consider the timescales of the stages of an oscillation cycle we see that the metal-to-oxide and oxide-to-metal transitions are practically 'instanta-

neous'. The ultrathin surface oxide appears within 2 s and the PdO disappears exponentially with a typical timescale of 6 s. However, the smoothening of the metal and roughening of the oxide are slower processes. Therefore we propose that the variation of the roughness, i.e. the step density, induces both transitions and thereby regulates the oscillations to have periods on the order of 1000 s.

To prove that indeed the roughness is responsible for inducing the phase transition we performed separate SXRD experiments in a 2-liter batch reactor that we pre-filled each time with a specific mixture of oxygen and CO. This mode of operation does not lead to spontaneous self-sustained oscillations, which enables us to separate cause and effect of the oscillations. These experiments allow us to derive the stability diagram of Fig. 4.2, which shows the minimum partial pressure of CO, at which the metal is stable against oxidation, as a function of the surface roughness, $FWHM_{metal}$. In order to use the roughness of the metal surface as a control parameter, we "prepared" the surface in each experiment by keeping it in the metal phase for a different amount of time, a longer time resulting in a smoother surface (lower $FWHM_{metal}$). In practice, this was done by starting each batch experiment at a different partial pressure of CO, at a fixed initial O_2 pressure. The details of this procedure are given in the Supplementary Information.

In each experiment, the two reactants were slowly converted to CO_2, thereby reducing the ratio between P_{CO} and P_{O_2}. During this stage the initially rough metal surface slowly smoothened as we determined from the decreasing FWHM of the $(1, 0, 0.2)$ diffraction peak, which is close to equivalent to the $(1, 0, 2)$ peak of Fig. 4.1. The smoothening continued until the metal-to-oxide transition took place, which was accompanied by a tenfold increase in the CO_2 production rate and the appearance of the diffraction peak at $(0.8, 0.4, 0.73)$ of the PdO(101) film. We performed this procedure four times, each time for a different initial value of P_{CO}. This resulted in the four curves of P_{CO} versus $FWHM_{metal}$ in Fig. 4.2. The lowest CO pressure in each curve, P_{CO}^* , indicates the conditions at which the metal-to-oxide transition took place. Figure 4.2 fully confirms our suspicion that roughness has a dramatic influence on the stability of the metal with respect to oxidation. The critical CO pressure, P_{CO}^*, shows a one-to-one correspondence with the step density. A significantly more oxidizing CO/O_2 mixture is required to oxidise a rough surface than a smooth surface. From a kinetic point of view this is unexpected since steps actually facilitate oxidation [98], but we argue below that it is a thermodynamic effect.
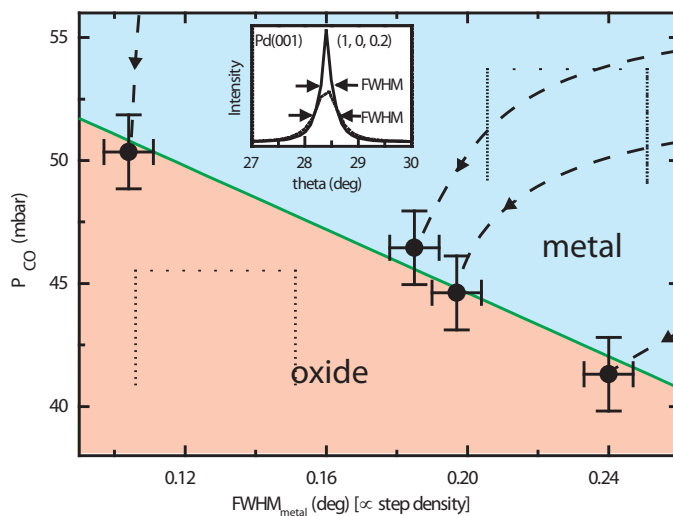
Figure 4.2: Stability diagram of the Pd(100) surface measured with surface x-ray diffraction. Measurements were performed at a temperature of 460 K in a CO/O$_2$ gas mixture with a fixed oxygen partial pressure of P_{O_2} = 0.48 bar in a batch reactor. The parameter along the horizontal axis of the main figure is the FWHM$_{metal}$ of the diffraction peak on the metal surface with reciprocal coordinates (h, k, l) = (1, 0, 0.2) immediately prior to the metal-to-oxide transition. This peak width is a sensitive measure of the density of steps on the metal surface. The trajectories of (FWHM$_{metal}$,P_{CO} approaching the metal-oxide transition are indicated by the four dashed curves. The error margins reflect the maximum variations observed in the peak width and the CO pressure at the transition. The inset shows two diffraction peaks on a trajectory at different FWHM$_{metal}$.

4.3 Discussion

Thermodynamically, the first-order metal-oxide transition of a smooth, step-free surface takes place when the free energies of the two competing structures, namely the metal surface with a chemisorbed layer of reactants and the oxide surface, are equal. The presence of steps shifts this balance because steps on both phases cost different amounts of (free) energy. This shift can go either way, but there are two arguments why steps could work in favour of the metal phase and make it stable down to a lower CO pressure (P_{CO}^*). First, on many metal surfaces CO molecules adsorb significantly more strongly at steps than on terraces [12, 85, 86]. For a metal surface in contact with CO, this reduces the effective step free energy

and under special circumstances can even lead to the spontaneous formation of steps [99]. We anticipate that this enhanced bonding effect is stronger for CO molecules than for O atoms adsorbed at steps on Pd(100) [100]. We propose that this reduction of the effective step free energy by CO adsorption stabilizes a rough metal phase with respect to a rough oxide phase. Secondly, steps make the metal surface a bad template for the PdO(101) structure, since they necessarily lead to dislocations in the oxide. The effect of the step density on the metal-oxide transition is reminiscent of the role of steps in the phase transition from the 7×7 surface reconstruction to the 1×1 phase on Si(111), for which the transition temperature depends on step density [101].

The combination of all experimental observations leads to a simple scenario for the self-sustained reaction oscillations (Fig. 4.3). Each cycle **(A)→(B)→(C)→(D)** contains the following four stages.

1. **(A)→(B)**: comprises a decrease in metal surface roughness. The cycle starts with a rough metal surface. The reaction follows the Langmuir-Hinshelwood (gas adsorption and reaction) mechanism, resulting in a low reaction rate R_{metal}. In the metal phase the surface smoothens, which shifts the conditions towards the metal-oxide phase transition (P_{CO}^* increasing towards P_{CO}).

2. **(B)→(C)**: represents the metal-to-oxide transition. When the step density decreases enough and $P_{CO}^* = P_{CO}$, then the surface oxidizes. The reaction rate changes abruptly to the Mars-van-Krevelen (oxide reduction and re-oxidation) mechanism with the high reaction rate R_{oxide}. Now that more CO is being consumed, P_{CO} is reduced in the vicinity of the active surface by an amount ΔP_{CO}, which further stabilizes the oxide. Note, that in this description we do not distinguish between the observed oxide structures (($\sqrt{5} \times \sqrt{5}$) and PdO), as the reaction rate is equally high for both of them.

3. **(C)→(D)**: comprises an increase in oxide roughness. The Mars-Van Krevelen reaction mechanism leads to a slow build-up of surface roughness. This, in turn, reduces P_{CO}^* towards P_{CO} towards.

4. **(D)→(A)**: comprises the oxide-to-metal transition. When the oxide has become sufficiently rough that $P_{CO}^* = P_{CO}$, the system switches back to a (rough) metal surface. The reaction changes abruptly to the Langmuir-Hinshelwood mechanism again, reducing the reaction rate to R_{metal}, thus
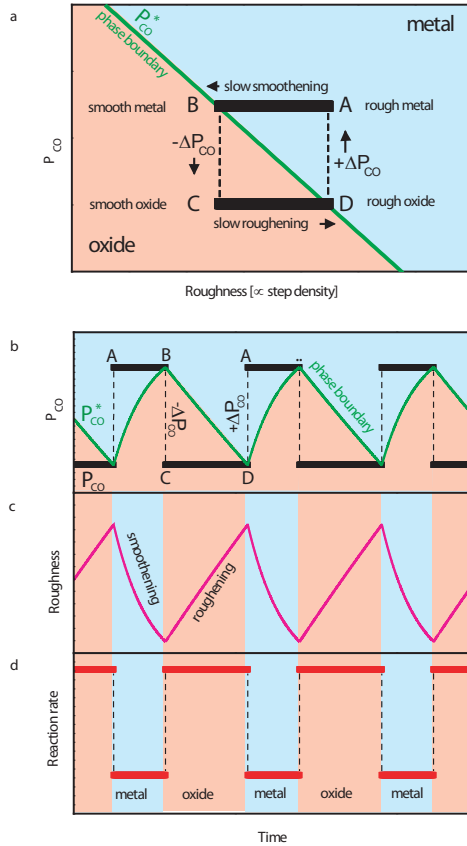
Figure 4.3: Generic model for the reaction rate oscillations. Each cycle takes the surface through stages **(A)** rough metal, **(B)** smooth metal, **(C)** smooth oxide, and **(D)** rough oxide, after which the next cycle starts again at **(A)**. **a)** The metal-oxide stability diagram (cf. Fig. 4.2), in which the phase boundary is determined by the roughness and the CO partial pressure, P_{CO}^*. Per cycle the surface crosses this boundary twice (at **B** and at **D**). **b-d)** The variations in roughness, P_{CO}, and reaction rate (P_{CO_2}) during three complete cycles. In the oxide phase, the surface becomes progressively rough, whereas it smoothens in the metal phase **b)**. As can be read off from **a)**, these variations in roughness introduce corresponding variations in the P_{CO}^* value of the metal-oxide transition, which are indicated by the green line in **b)**. At points **B** and **D** in the cycle, this critical P_{CO}^* value becomes equal to the actual CO pressure P_{CO} (black lines in **b)**) and the phase transition takes place. Since the reaction rate on the oxide is higher than that on the metal **d)**, the CO pressure in the reactor switches up or down by ΔP_{CO} every time the surface is reduced or oxidized (black lines in **b)**).

increasing P_{CO} by ΔP_{CO} and further stabilizing the metal phase. This restores the starting conditions and closes the cycle.

The period of the oscillation is determined by the magnitude of ΔP_{CO} and by the smoothening and roughening rates in the metal and oxide phases.

With the exception of the effect of the oxide roughness on the oxide-to-metal transition all characteristics of this scenario are based on experimental observations. These characteristics include increasing and decreasing oxide and metal roughness respectively; the dependence of P_{CO}^* on roughness; the different reaction mechanisms and rates; and the resulting changes in local P_{CO}.

We have also tested the scenario in a simple numerical calculation, in which we modelled the roughness evolution and the dependence of P_{CO}^* on roughness with first-order differential equations. The results of the calculation, under steady state conditions, are shown in Fig. 4.3 (for the details of this calculation see the Methods section and the Supplementary Information). Although the model is too crude to faithfully describe all details of the CO oxidation reaction on Pd(100), it fully captures the essence of the observed oscillations, such as the influence of P_{CO} on the oscillation period and on the ratio between the metal and oxide parts of the oscillations.

Our observations and interpretation of reaction oscillations are at variance with existing models for reaction oscillations during CO oxidation on Pt-group metals. We observed that the system oscillates between a metal surface with O and CO chemisorbed (low reaction rate) and the thin oxide layer (high reaction rate). The periodic transition between the metal and the oxide is caused by the formation and decay of roughness (steps). By contrast, at low pressures ($< 10^{-6}$ mbar) oscillations are caused by variations in the concentration of the chemisorbed reactants, periodically switching between two stable sates of Langmuir-Hinshelwood kinetics: a chemisorbed O-dominated (high reaction rate) and a CO-dominated metal surface (low reaction rate), coupled to adsorbate induced restructuring of the metal surface or the insertion of subsurface oxygen species [94]. At atmospheric pressures -the regime discussed here- oxides play a role and according to the widely accepted model proposed by Sales et al. the switching between chemisorbed O-dominated (high reaction rate) and CO-dominated (low reaction rate) metal surface is caused by the slow formation of a catalytically inactive oxide [95, 102].

Based on our model and simple diffusion and reaction-rate considerations, we

predict that the oscillation period should be a strong function of temperature, with higher temperatures leading to much shorter periods. Vicinal surfaces, which have high step densities by themselves, are expected to oxidise at lower CO pressures compared to low-index surfaces. In addition, the period of the metal phase of an oscillation cycle on a vicinal surface should be short as the length over which atoms have to move to restore the initial (high) step density is short. Another important element is hidden in the design of the reactor and, in particular, in the flow resistance of the gas line between the CO pressure regulator and the reactor, since this resistance determines the strength ΔP_{CO} of the pressure variations. This quantity dictates how wide or narrow the window is of pressures for which the system will exhibit spontaneous reaction oscillations and it also has a direct influence on the oscillation period. This aspect may be responsible for the large variation in oscillation behaviour found for the same reaction systems between different instruments or different research groups [95].

Our scenario presents a new mechanism for oscillatory oxidation reactions at atmospheric pressure. It is not specific for Pd(100); we have observed similar oscillations in CO oxidation on several other Pd and Pt surfaces [103]. Equivalent oscillation mechanisms, again involving the role of steps, may be at play in other catalytic reaction systems, e.g. other oxidation reactions or reactions involving the formation of other surface species, such as carbides, sulphides or nitrides.

The new role identified here for roughness in heterogeneous catalysis may serve as a specific target for future catalyst design; think of new structural promoters that inhibit the formation of steps or enhance surface mobility and thus increase the decay rate of the roughness.

4.4 Methods and supplementary information

The surface x-ray diffraction (SXRD) experiments were performed at the ID03 beamline of the European Synchrotron Radiation Facility (ESRF) in two separate set-ups. One is a combined ultrahigh vacuum - high pressure SXRD chamber (10^{-10} mbar - 2 bar), which has a volume of $\sim 2\,l$ and was equipped with a 360°cylindrical beryllium window for entrance and exit of the x-rays [21]. The other set-up is a combined UHV-high pressure (10^{-9} mbar - 1.2 bar) flow reactor, which has a volume of 17 ml [74, 77]. The top part of the reactor is a beryllium dome allowing for entrance of the incident and exit of the diffracted x-ray beam.

The chambers were mounted on a z-axis diffractometer with the crystal surface in a horizontal plane. We have used a focused beam of monochromatic, 17 keV or 20 keV x-rays, impinging on the surface at a grazing angle of typically 1°.

High-pressure scanning tunneling microscopy (HP-STM) measurements were performed in a dedicated Reactor-STM, which combined preparation and characterization of the surface under ultrahigh vacuum conditions with STM experiments in an integrated flow-reactor cell (volume 0.4 ml) at temperatures up to 500 K and pressures up to 5 bar [104, 105].

All instruments are equipped with a gas manifold with pressure regulators and flow controllers, with which the pressure, composition and flow rate of high-purity mixtures of O_2 and CO could be prepared. In the experiments a quadrupole mass spectrometer was used for online analysis of the gas composition in the reactor. In all experiments a mechanically polished, (001) oriented, Pd crystal was used that was prepared in situ, under ultrahigh vacuum conditions. In each setup, the temperature of the Pd was measured with a thermocouple and regulated to within $\Delta T = 2$ K. Only in the batch reactor, the exothermic reaction led to a temperature increase higher than this, when the surface switched from metal to oxide, but all measurements combined in Fig. 4.2 were taken in the metal phase and were not affected by this.

In all experiments a mechanically polished, (001) oriented, Pd crystal was used that was prepared in situ, under ultrahigh vacuum conditions. Several cycles were necessary of a standard procedure, involving Ar^+ ion bombardment and annealing, in order to obtain a well-ordered Pd(100) surface with a low step density, as was verified with SXRD, low-energy electron diffraction and STM.

In the numerical model used to calculate the graphs shown in Fig. 4.3 each of the two phases of the surface, metal and oxide, is characterized by two rates, namely the reaction rate of CO oxidation and the rate of change of the surface roughness (see Supplementary Information). The condition for the surface to be either in the oxide or the metal phase was $P_{CO} < P_{CO}^*(\rho)$ for the oxide and $P_{CO} > P_{CO}^*(\rho)$ for the metal, with P_{CO} the CO pressure in the reactor near the surface and $P_{CO}^*(\rho)$ the critical CO pressure at which the transition takes place, which depends on the roughness ρ as $P_{CO}^*(\rho) = P_{CO}^*(0) - d\rho P_{CO}^*(0)$, where $P_{CO}^*(0)$ is the critical CO pressure for zero roughness, d is a positive constant and the normalized roughness is $0 \leq \rho < 1$. In the model the roughness increases in the oxide phase, proportional to the reaction rate. In the metal phase the roughness decays exponentially with time.

4.4.1 SXRD in flow cell: oscillations

After closing the reactor, a constant 50 ml_n min^{-1} gas flow composed of 675 mbar Ar, 500 mbar O_2, and 25 mbar CO was admitted in the reactor. A direct leak from the reactor into the UHV allowed us to analyze the gas composition in the reactor. To obtain optimal time resolution for the SXRD (~ 1 s) the diffraction signal was recorded using the Maxipix 2D pixel detector [79, 106].

In two separate experiments two diffraction signals were recorded during the spontaneous oscillations: the Pd(100) (h, k, l) = (1, 0, 2) anti-Bragg position (Fig. 4.1) and the (h, k, l) =(0.8, 0.4, 0.73) position characteristic of the approximately 1.9 nm thick bulk-like PdO overlayer. Figure 4.4 shows the inverse FWHM of the oxide diffraction peak, $FWHM_{oxide}^{-1}$. In Fig. 4.4 one can clearly see the decrease of the domain size of the PdO overlayer, indicating the roughening of the layer. Peak widths $FWHM_{metal}$ and $FWHM_{oxide}$ were obtained from fitting a Lorentzian peak shape to the diffraction signals as shown in Movie S1 (1, 0, 2) and Movie S2 (0.8, 0.4, 0.73) of the supplementary material of [72].

Pd(100) does not reconstruct and therefore the correlation length of the x-ray diffraction, given by the inverse of the full width at half of the maximum intensity $FWHM_{metal}^{-1}$ of the (h, k, l) = (1, 0, 2) diffraction peak, is equivalent to the average terrace width (it is the same for the (h, k, l) = (1, 0, 0.2) peak used in the batch experiment described below). The presence of roughness (steps) reduces the average terrace width causing a broadening of the diffraction peak. Strain may also broaden the diffraction peaks, but based on the STM observations (see below) we conclude that roughness is dominating the $FWHM_{metal}$ values.

4.4.2 STM in flow cell: oscillations

To complement our SXRD data with real space microscopic information we show scanning tunneling microscopy data that were recorded on a Pd(100) surface inside a micro-flow reactor during oscillatory CO oxidation at a total pressure of 1.2 bar, a flow of 4 ml_n min^{-1} and a temperature of 408 K. The combination of the mass spectrometry signals and the STM images are shown in Fig. 4.5. Figure 4.5a shows that the CO oxidation rate on Pd(100) in a constant reactant flow at atmospheric pressure spontaneously oscillates between two distinct levels, R_{oxide} and R_{metal}. The oscillations in the CO pressure in the reactor are in anti-phase with the variations in CO_2 production and are caused by the difference in CO
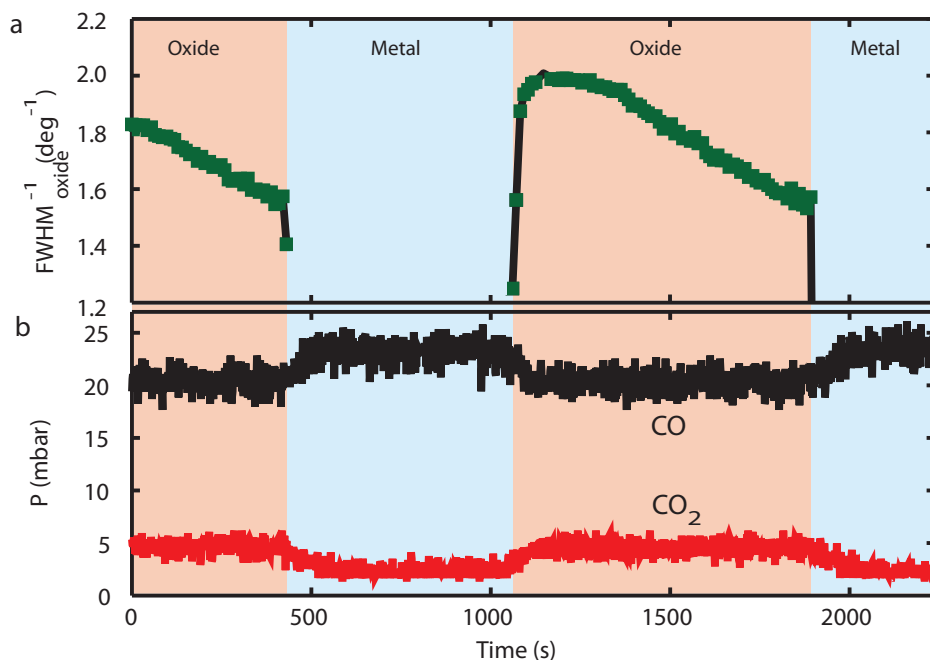
Figure 4.4: Oxide diffraction peak during oscillations in the CO oxidation rate on Pd(100). Measurements were performed at a temperature of 447 K in a $CO/O_2/Ar$ gas mixture with an O_2 pressure of 500 mbar, an Ar pressure of 675 mbar and a CO pressure of 25 mbar flowing at 50 ml_n min^{-1}. **a)** The $FWHM_{oxide}^{-1}$ (proportional to the domain size) of the PdO diffraction peak at (h, k, l) = (0.8, 0.4, 0.73). **b)** The partial CO and CO_2 pressures in the reactor as measured simultaneously by mass spectrometry.

consumption at the two reaction rates. Figure 4.5 shows STM images that were recorded during these self-sustained reaction oscillations. They were recorded in 100 s per image and therefore contain both spatial and temporal information of the topography. Scan lines of the images were synchronized with the mass spectrometry data along the horizontal time axis. In our earlier high-pressure STM studies we had already found that the oscillations are the periodic switching between the low-activity metal phase and the high-activity oxide and these changes in structure can be recognized also in Fig. 4.5 [51]. The metal phase is characterized by height variations of multiples of the step height of Pd(100) and step
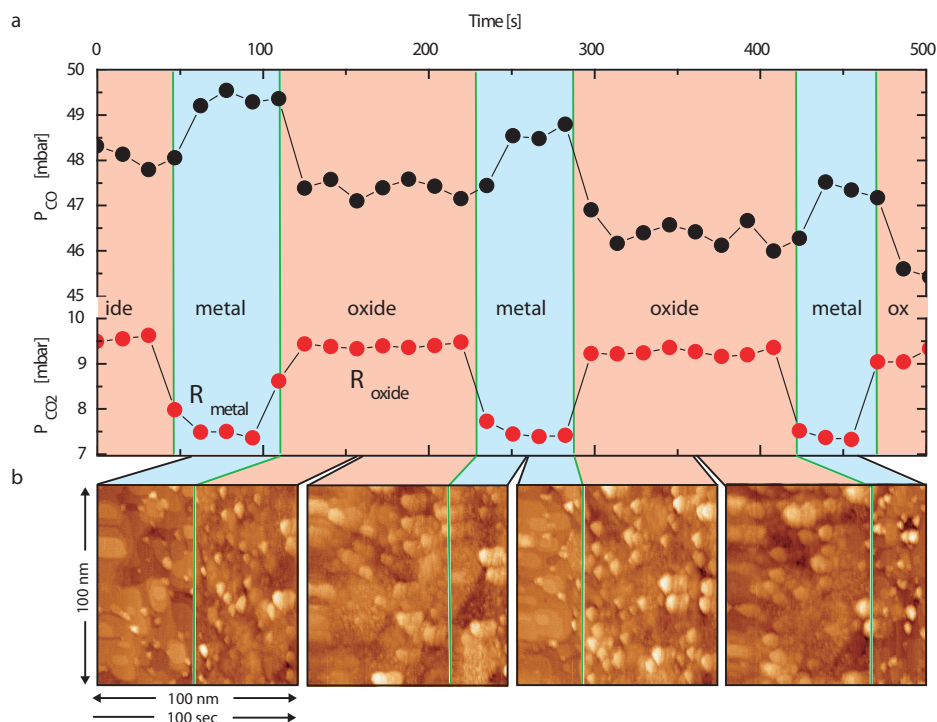
Figure 4.5: Scanning tunneling microscopy during oscillations in the CO oxidation rate on Pd(100). **a)** The reaction rate (P_{CO_2}) and the CO pressure (P_{CO}), observed in a flow reactor at a constant O_2 pressure of P_{O_2} 1.2 bar and a temperature of 408 K. **b)** The scanning tunneling microscopy images ($V_t = 100$ mV, $I_t = 0.2$ nA, image size: 100 nm×100 nm, slow scan direction along the time axis) have been recorded simultaneously with the CO_2 and CO pressures and show that the oscillations are accompanied by the oxidation and reduction of the Pd surface. The metal phase exhibits characteristic terrace-and-step configurations with the well-defined step height of Pd(100), while the oxide is rougher and shows no such order.

49

and island structures are visible. The experiment started with a smooth Pd(100) surface with a typical initial step density of 0.03 step nm^{-1} measured in the fast scan direction. During the oscillations shown in Fig. 4.5 the step density on the metal varied from 0.2 step nm^{-1} to 0.1 step nm^{-1} determined along the fast scan direction. The oxide surface is dominated by roughness with no repeating height unit. From the changes both in the reaction rates and in the STM images we see that the metal-oxide and oxide-metal transitions take only a fraction of a second, while the period of the oscillations can be many minutes. The STM data illustrate the presence and the variations of roughness during the oscillations.

4.4.3 SXRD in batch reactor: pulse experiment

The four (FWHM$_{metal}$, P_{CO}^*) data points of the phase diagram of Fig. 4.2 were taken from Fig. 4.6, which in (a) shows the partial pressures of CO, O_2, and CO_2 in the reaction chamber during CO oxidation experiments at a temperature of 460 K. Figure 4.6 shows a series of rocking scans of the Pd(100) crystal truncation rod (surface diffraction peak) at (h, k, l) = (1, 0, 0.2) that had been recorded simultaneously. The reaction chamber was operated in batch mode, which means that we added CO at t_1, t_3, t_5, t_7 to restart the reaction, each time after all previously admitted CO had been converted to CO_2. By also adding O_2 we kept the oxygen pressure constant over the duration of the experiment. The reaction product CO2 gradually accumulated in the chamber. (Note that whenever we introduced gas to the chamber there were transients in all the mass spectrometer signals at $t = 10, 12, 56, 60, 98, 107, 140, 169$ min. These transients are related to our gas sampling and detection and not to the reaction kinetics.)

The experiment started at t_0 in 480 mbar O_2 and 230 mbar CO_2, left over from a previous reaction cycle. Under these conditions we observed a diffraction peak at (0.8, 0.4, 0.74), corresponding to palladium oxide, i.e. PdO(101) (Fig. 4.6). There was no intensity at the metal Pd(100) position (1, 0, 0.2). At $t = 10$ min. we added O_2 to the chamber through a leak valve to increase P_{O_2} to 500 mbar. At t_1 we added 52 mbar of CO to the chamber. The CO reacted with O_2 to the reaction product CO_2, as shown by the linear decrease of the CO and O_2 pressures and the increase in the CO_2 pressure in Fig. 4.6 for $t_1 < t < t_2$. Figure 4.6 shows that as soon as we introduced the CO at t_1 the Pd(100) diffraction peak appeared at (1, 0, 0.2). The PdO(101) peak had vanished completely. The CO pressure increase had induced the oxide-to-metal transition.
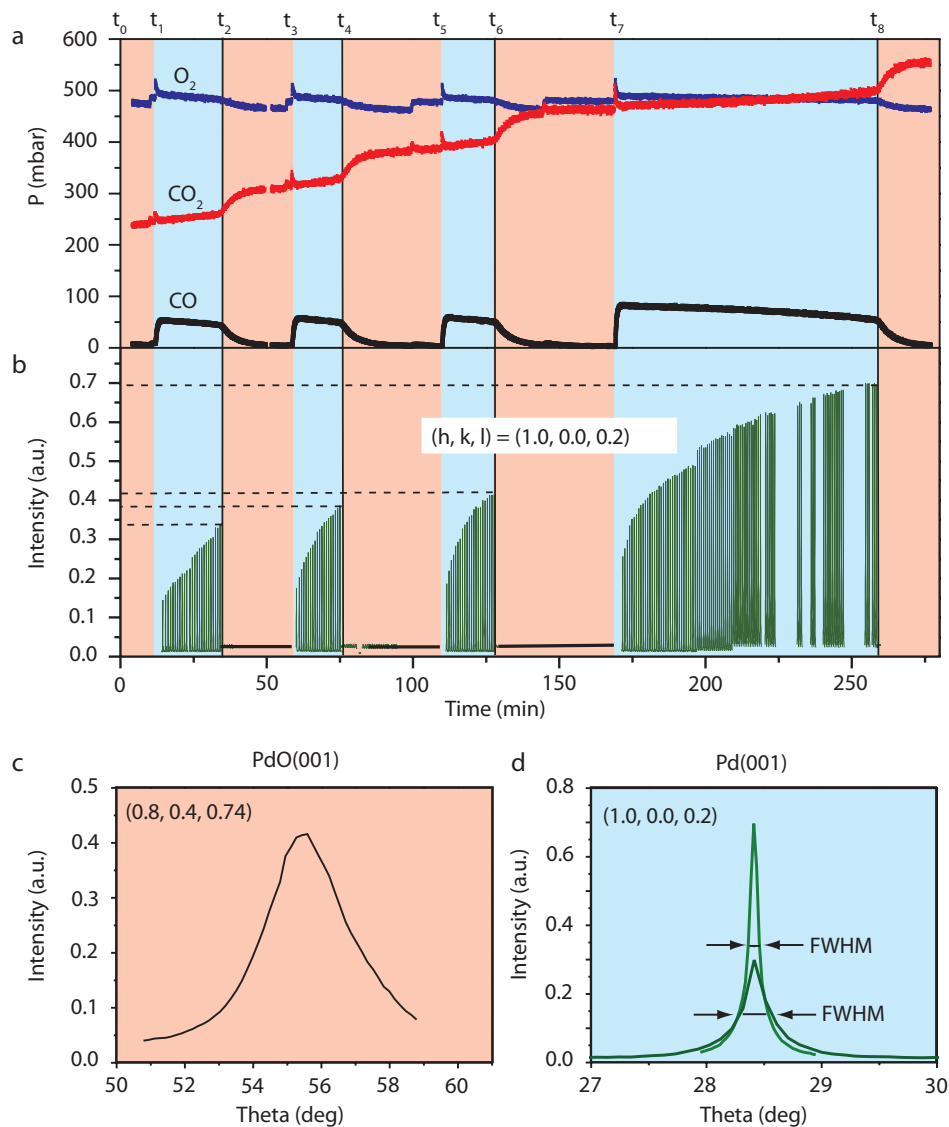
Figure 4.6: Cycles of spontaneous oxidation and forced reduction of the Pd(100) surface during CO oxidation at 460 K in a batch reactor. **a)** Partial pressures of the reactants CO and O_2 and the reaction product CO_2. **b)** Series of rocking scans of the Pd(100) surface diffraction peak at (h, k, l) = (1, 0, 0.2). **c)** Rocking scan of the PdO(001) peak of the oxidized palladium surface at (h, k, l) = (0.8, 0.4, 0.74). **d)** Individual rocking scan of the (1, 0, 0.2) crystal truncation rod of Pd(100) from the series in **(b)**.

In the metal phase the height of the Pd(100) peak increased with time. As the integrated intensity of the peak remained constant, the increase in height directly implies that the $FWHM_{metal}$ decreased. The $FWHM_{metal}$ of the Pd(100) diffraction peak is inversely proportional to the coherence length of the Pd surface structure, which is equivalent to the average terrace width. The $FWHM_{metal}$ is therefore a direct measure of the step density. The decrease of the $FWHM_{metal}$ with time reflects the slow smoothening of the Pd(100) surface by reduction of the step density. At t_2 the (1, 0, 0.2) diffraction peak spontaneously disappeared on a timescale of less than one second. Simultaneously, the reaction rate increased by a factor of 10. In this reaction cycle we recorded only the diffraction peak of Pd(100) at (1, 0, 0.2), but from other cycles we know that at t_2 the PdO(101) peak at (0.8, 0.4, 0.74) instantly reappeared, as shown in Fig. 4.6c. The spontaneous event observed at t_2 was the metal-oxide phase transition of the palladium surface. After all CO had been consumed we again added oxygen, followed by a 55 mbar CO pulse at t_3, which started the second cycle. At each new cycle we increased the amount of CO added, which increased the time needed for the reaction on the metal surface to reduce the CO pressure in the chamber by reaction to CO_2 to the critical CO pressure P_{CO}^*. This delayed the metal-to-oxide transition and therefore allowed the metal surface more time to smoothen. The combinations of the critical $FWHM_{metal}$ value of the (1, 0, 0.2) diffraction peak and the critical CO pressure at the metal oxide transitions at t_2, t_4, t_6, and t_8 define the metal-oxide phase boundary in Fig. 4.2. This experimental procedure used to determine the stability diagram ($FWHM_{metal}$, P_{CO}^*) did not allow us to perform a similar analysis of ($FWHM_{oxide}$, P_{CO}^*) for the oxide-to-metal transition.

4.4.4 Numerical model for reaction rate oscillations

In our model, each of the two phases of the surface, metal and oxide, is characterized by two rates, namely the reaction rate of CO oxidation and the rate of change of the surface roughness. These rates are summarized in Table 4.1. The reaction rate R_{metal} on the metal (Eq. (4.1)) corresponds to 'text-book' Langmuir-Hinshelwood kinetics in which O_2 adsorbs dissociatively and CO molecularly. The constants k_1 and k_2 are ratios of the rate constants for adsorption and desorption of O_2 and CO respectively. The reaction rate on the oxide (Eq. (4.3)) reflects our observation that R_{oxide} is proportional to the CO pressure and independent of P_{O_2} [104].

Table 4.1: Rate equations for the numerical model.

	Reaction rate		Rate of change in roughness	
Metal	$R_{\mathrm{metal}} = \dfrac{\sqrt{k_1 P_{O_2}} k_2 P_{CO}}{\left(\sqrt{k_1 P_{O_2}} + k_2 P_{CO} + 1\right)^2}$	(4.1)	$\dfrac{d\rho}{dt} = -a\rho$	(4.2)
Oxide	$R_{\mathrm{oxide}} = k_3 P_{CO}$	(4.3)	$\dfrac{d\rho}{dt} = b(1-\rho) R_{\mathrm{oxide}}$	(4.4)

We express the roughness of the surface in a dimensionless parameter ρ, which can vary between 0 (completely smooth surface) and 1 (maximally rough surface). On the metal surface there are several competing diffusion mechanisms that reduce the step density, each with its own non-trivial scaling behaviour with time. In the SXRD experiments, however, we find that the net result is very well described by exponential decay of the roughness. In the model this is introduced by making the rate of roughness change proportional to $-\rho$ (Eq. (4.2)). On the oxide, roughness is observed as a 'by-product' of the reaction. For the oxide on Pt(110) we have measured by STM that roughness was produced approximately proportional to the amount of produced CO_2 [104]. For Pd(100) we have not been able to perform a similar analysis, but we nevertheless assume that the rate of reaction-induced roughening on the oxide is proportional to R_{oxide} (Eq. (4.4)). The extra factor $(1-\rho)$ in the oxide's roughening rate limits the roughness to the interval $[0;1)$. The constants and a and b in Eqs. (4.2) and (4.4) are both positive.

An important element in the model is the change $\pm\Delta P_{CO}$ in local CO pressure when the surface oxidizes or reduces. This change is directly proportional to the change in reaction rate

$$\Delta P_{CO} = c\left(R_{\mathrm{oxide}} - R_{\mathrm{metal}}\right) \qquad (4.5)$$

where c is a positive constant. For oscillations under steady-state conditions R_{oxide} and R_{metal} are constant and so is ΔP_{CO}.

Finally and most importantly, we need to specify the relation between the CO pressure P_{CO}^* at which the metal-oxide phase transition takes place and the surface roughness ρ. As we have seen experimentally in Fig. 4.2 we can describe this by a linear relation

$$P_{CO}^*(\rho) = P_{CO}^*(0) - d\rho, \qquad (4.6)$$

where d is a positive constant. When P_{CO} is higher than $P_{CO}^*(\rho)$, the surface is in the metallic phase with the reaction rate and roughness variation being prescribed

$$P_{CO}, \rho$$

time$_n$

$$P_{CO} < P_{CO}^*(\rho) \qquad\qquad P_{CO} \geq P_{CO}^*(\rho)$$

oxide

$$P_{CO} = P_{CO}^{input} - \Delta P_{CO}^{oxide}$$

$$R = R_{oxide}(P_{CO})$$

$$\rho_{n+1} = \rho_n + b(1-\rho_n)R_{oxide}$$

metal

$$P_{CO} = P_{CO}^{input} - \Delta P_{CO}^{metal}$$

$$R = R_{metal}(P_{CO})$$
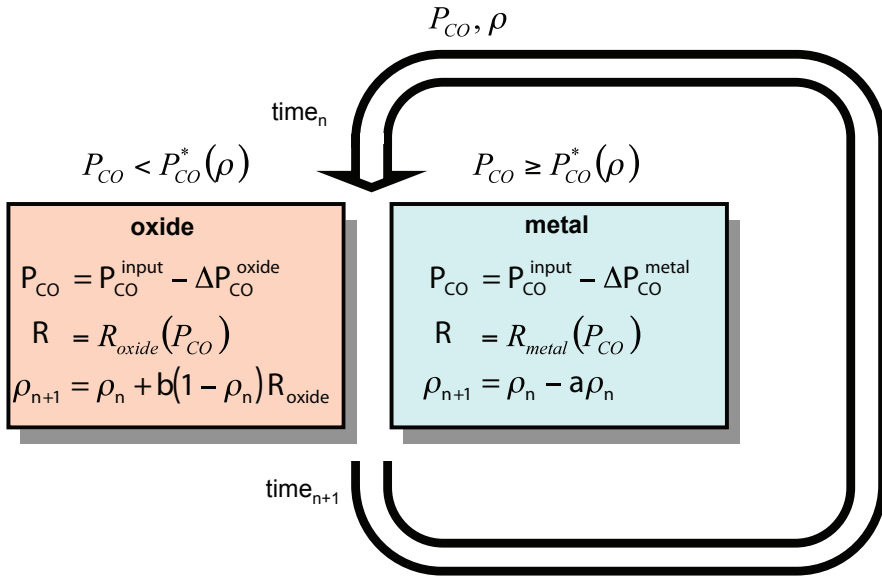
$$\rho_{n+1} = \rho_n - a\rho_n$$

time$_{n+1}$

Figure 4.7: Scheme of the numerical model for self-sustained oscillations at constant oxygen pressure. At the beginning of each numerical time step the local CO pressure P_{CO} and the roughness ρ determine (through P_{CO}^*) whether the surface is in the metal phase or in the oxide phase. If the system is in the metal phase the local CO pressure is equal to $P_{CO} = P_{CO^{input}} - \Delta P_{CO}$, close to the partial pressure of CO in the supplied gas flow ($P_{CO^{input}}$), the reaction rate follows Eq. (4.1), and the roughness decreases from ρ_n to ρ_{n+1} according to Eq. (4.2). In the oxide phase the local CO pressure is reduced by $\Delta P_{CO} = \Delta P_{CO}^{oxide} - \Delta P_{CO}^{metal}$ as a result of the higher reaction rate. The reaction rate follows Eq. (4.3), and the reaction induced roughness increases at a rate proportional to the reaction rate, as given by Eq. (4.4).

by Eqs. (4.1) and (4.2). When it is below $P_{CO}^*(\rho)$, the surface is in the oxide phase and the rates are given by Eqs. (4.3) and (4.4).

Together, Eqs. (4.1) to (4.6) successfully describe the characteristics of the self-sustained oscillations experimentally observed under steady-state reaction conditions as well as the transient oscillations observed during slow ramps in the CO partial pressure. The numerical scheme, based on Eqs. (4.1) to (4.6), which we used to calculate the reaction rate oscillations of Fig. 4.3 is shown in Fig. 4.7.

Equations (4.2), (4.4) and (4.6) only use a single roughness parameter to describe the roughness of both the metal and the oxide. Accordingly the roughness

shows no discontinuity at the phase transition in Fig. 4.3. However, the density of Pd atoms in the oxide is different from the density in the metal. As a consequence, the formation of the oxide on an initially flat Pd(100) surface leads to approximately 20% of the oxidized surface being covered by islands of expelled (and subsequently oxidized) Pd. This introduces an abrupt increase in step density when the surface oxidises. When the surface is reduced again, we do not observe an equivalent, abrupt decrease in the step density, simply because the Pd adatom islands (see Fig. 4.5) require some time to disintegrate. Actually, the density difference leads to the introduction of vacancy islands when the surface is reduced, which contributes a small, abrupt increase to the step density. Continued cycles of oxidation and reduction further reduce the magnitude of these abrupt effects, but the trends stay for the roughness to decrease in the metal phase and increase in the oxide phase. Irrespective of these 'offsets' in step density introduced by the above, abrupt effects, we see that there is a one-to-one correspondence between the step density on the metal surface immediately prior to oxidation and the roughness on the surface oxide immediately after the transition and there is a similar one-to-one correspondence between the roughness on the surface oxide immediately prior to reduction and the step density on the metal surface immediately after the transition. It is evident that the effects described here will influence the energetics, but they will not change the qualitative picture. From the two roughnesses (metal and oxide), we show in Fig. 4.3 only that of the metal surface ($\text{FWHM}_{\text{metal}}$ at P_{CO}^*), just prior to the switching event. For simplicity we did not include these offsets in the numerical model.

Chapter 5

CO oxidation and reaction oscillations on Pd nanoparticles

In this chapter we describe the results of a structure and reactivity study of supported Pd nanoparticles under conditions relevant for CO oxidation. Observations of reaction oscillations on these Pd nanoparticles are extensively discussed. We show that the reaction rate oscillations on the nanoparticles follow a similar oxidation-reduction mechanism as those on the extended Pd(100) single-crystal surface. We also show that interface compounds between the particles and the substrates are present.

5.1 Introduction

Reaction rate oscillations are known to occur in many different systems in homogeneous as well as heterogeneous reactions. The Belousov-Zhabotinsky reaction and the Briggs-Rauscher reaction are the most famous examples in the case of homogeneous reactions in a solution, due to the spectacular spontaneous colour changes of the solution [107, 108]. In the case of heterogeneous catalysis one can also find oscillating reactions, a famous example being the work by Ertl on the self-sustained oscillations in the CO oxidation rate on metal surfaces, at both low and high pressures [94]. Reaction oscillations are not restricted to single-crystal surfaces [72], but also occur on supported nanoparticle catalysts [109]. For the latter systems, oscillations have mainly been measured using gas analysis and spectroscopic techniques [110]. It was also shown that oscillations occur in a real car catalyst [111].

Supported nanoparticles make up a much more intricate system than single crystal model catalysts. Even on a single face of a single crystal, multiple oxides can exist, as shown in Chapter 3. A nanoparticle exposes multiple facets to the reactant gases, but also edges and corners. The relative densities of these different sites change with particle size. Furthermore, a nanoparticle can also have a significant interaction with the supporting material. All these extra ingredients can have an influence on the thermodynamics and kinetics of oxide formation.

Several detailed studies have been performed of the oxidation of epitaxially aligned Pd and Rh particles [25, 112]. Size-dependent oxidation of Pd supported on Fe_3O_4 has been studied using molecular beams and STM [113]. Oxidation of Al_2O_3 supported Pd nanoparticles has been studied using FTIR, XRD and DFT [114]. The role played by the different oxides in the activity of the particles towards CO oxidation remains a topic of discussion also for Pt and Pd particles [110, 114–118].

In this chapter we will analyse the shape and crystal structure of supported Pd nanoparticles in situ and during spontaneous reaction oscillations. We use XRD to determine whether (bulk) PdO is present under various P_{O_2}/P_{CO} ratios and at different temperatures relevant for CO oxidation. Simultaneously, we monitor the CO_2 production by mass spectrometry. Then, we study the particles while the CO_2 production shows spontaneous oscillations under constant temperatures and gas flow. We again use XRD to determine the presence of PdO during the oscillations. We use GISAXS as an additional tool to determine the average particle

dimensions during the oscillations [11].

5.2 Experimental methods

Pd nanoparticles with a radius of 15 nm were created using a spark discharge method followed by size selection and annealing [119]. Subsequently the particles were deposited on two different substrates, SiO_2 and α-Al_2O_3(0001). This sample preparation ensures a narrow size distribution of the particles with a relative standard deviation of $\frac{\sigma_R}{R} = 0.05$, allowing us to accurately determine the average particle size. The number density of the particles was approximately $7 \times 10^2 \, \mu m^{-2}$. However the particles are deposited at random positions on the substrate and their crystal structure is not epitaxially aligned with the substrate crystal structure. This is different from the case of epitaxial Pd nanoparticles obtained by Pd deposition on MgO(100) [25, 120, 121].

The samples were used in the XRD and GISAXS experiment in the flow setup without further preparation steps. Samples were mounted on a tungsten plate supported on a bora-electric heater described in Chapter 2. A type-C thermocouple was pressed against the tungsten plate supporting the sample.

All experiments were performed at the ID03 beamline at the ESRF. We used a focused beam of 18 keV x-rays (5×10^{12} photons s^{-1}, 200 mA ring current). For the GISAXS experiments, 500 μm anti-scattering slits were placed just before the Be dome. Ideally one would use a beamstop between the sample and the Be exit windows to prevent scattering from the exit window. The small space between the Be dome and the sample forced us to perform the GISAXS experiments at a relatively high incidence angle of 0.7° instead. Note that by using this high incidence angle we effectively used the sample and supporting tungsten plate as a beamstop. The XRD experiments were performed at a 0.5° incidence angle. A maxipix 2D pixel detector was used to collect the diffracted x-rays [79–81].

5.3 Results and discussion

5.3.1 Reactivity and crystal structure

Figure 5.1 shows an Arrhenius plot of the reaction rate of the 15 nm Pd particles supported on SiO_2. For each P_{O_2}/P_{CO} ratio the reaction rate was measured

twice: once after pre-exposing the sample to pure oxygen for 45 s and once af-
ter pre-exposing the sample to pure CO 45 s. After the pre-exposure the sample
was exposed to the desired P_{O_2}/P_{CO} for 250 s the gasflow through the reactor
was stopped, turning the reactor into a batch reactor. Subsequently the reaction
rate was determined from the initial slope of the mass 44 signal in the QMS.
Since the difference between the pre-reduced and pre-oxidized datasets is small,
we conclude that the pre-exposure has little influence on the active phase of the
catalyst under the supplied reaction conditions. Note that for each reaction rate
measurement at a specific temperature in Fig. 5.1 we pre-exposed the sample
at that same specific temperature. Pre-exposing at a much higher temperature
(≥ 1073 K) might give very different results due to full oxidation of the parti-
cles [114]. For comparison with the data in Chapter 3 the turnover frequency
(TOF) on the vertical axis of Fig. 5.1 is calculated by assuming that the sample
has the same amount of reactive sites as a Pd(100) surface. The actual num-
ber of active sites on the particle sample can of course be very different. The
apparent activation energy is changing over the low end of the measured tem-
perature range in Fig. 5.1 from 0.71 eV at 650 K to 0.15 eV at 550 K for the pre-
reduced dataset at $P_{O_2}/P_{CO} = 0.6$. This changing activation energy was reported
in earlier studies [122, 123]. At high temperatures the TOF reaches a plateau at
≈ 200 molec site^{-1} s^{-1}. This value is precisely the same for the measurements
on the Pd(100) crystal shown in Fig. 3.4 and corresponds to the mass transfer
limit (MTL). We do observe however that the mass transfer limited reaction rate
is reached for each P_{O_2}/P_{CO} ratio at a higher temperature for the particles than
for the Pd(100) single-crystal surface. This can have two causes: firstly the real
number of active sites on our NP sample is lower than on a single-crystal and
secondly the temperature measurement might have a systematic error. This error
in the temperature measurement is caused by the fact that the thermocouple ac-
tually measures the temperature of the plate supporting the sample. The sample
temperature will thus be overestimated in case of a bad thermal contact between
the plate and the sample.

  Accompanying every data point in Fig. 5.1 we recorded the powder diffraction
pattern from the particles. These patterns are shown in Fig. 5.2. The scans indi-
cate that bulk PdO was only present at the highest temperatures at a P_{O_2}/P_{CO} of 2
and 10 and only if the sample was pre-oxidized. Based on our measurements on
single-crystal Pd(100) in Chapter 3 we expect a surface oxide to be present on the
particles in the other cases where the reactivity reaches the MTL. The detection
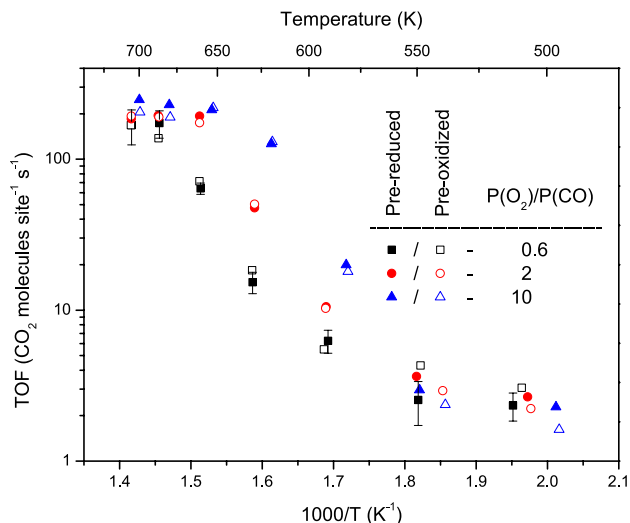
Figure 5.1: Arrhenius plot of the TOF for CO oxidation of the SiO_2-supported Pd nanoparticles of 15 nm diameter. For comparison with Fig. 3.4 the number of sites per unit of sample area is assumed to be equivalent to the number of sites on Pd(100). Data are shown for three different ratios between the partial pressure of O_2 and CO and for particles pre-exposed to either O_2 or CO prior to the TOF measurement. Representative error bars are shown for the pre-reduced dataset at $P_{O_2}/P_{CO} = 0.6$

of surface oxides remains challenging and this type of XRD scan is not sensitive to surface oxides. One could resort to epitaxially aligned nanoparticles for detection of surface oxides [112].However, in a first series of attempts with Pd particles on MgO(100) we have found that under catalytically relevant conditions the epitaxy of the particles was quickly lost.

Interestingly at lower temperatures ($< 550\,\mathrm{K}$) we observe a decrease of the 2θ angle for the Pd(111) reflection if the nanoparticles are pre-reduced with CO. This points to a lattice expansion of the nanoparticles, likely caused by carbon dissolution [124–126].
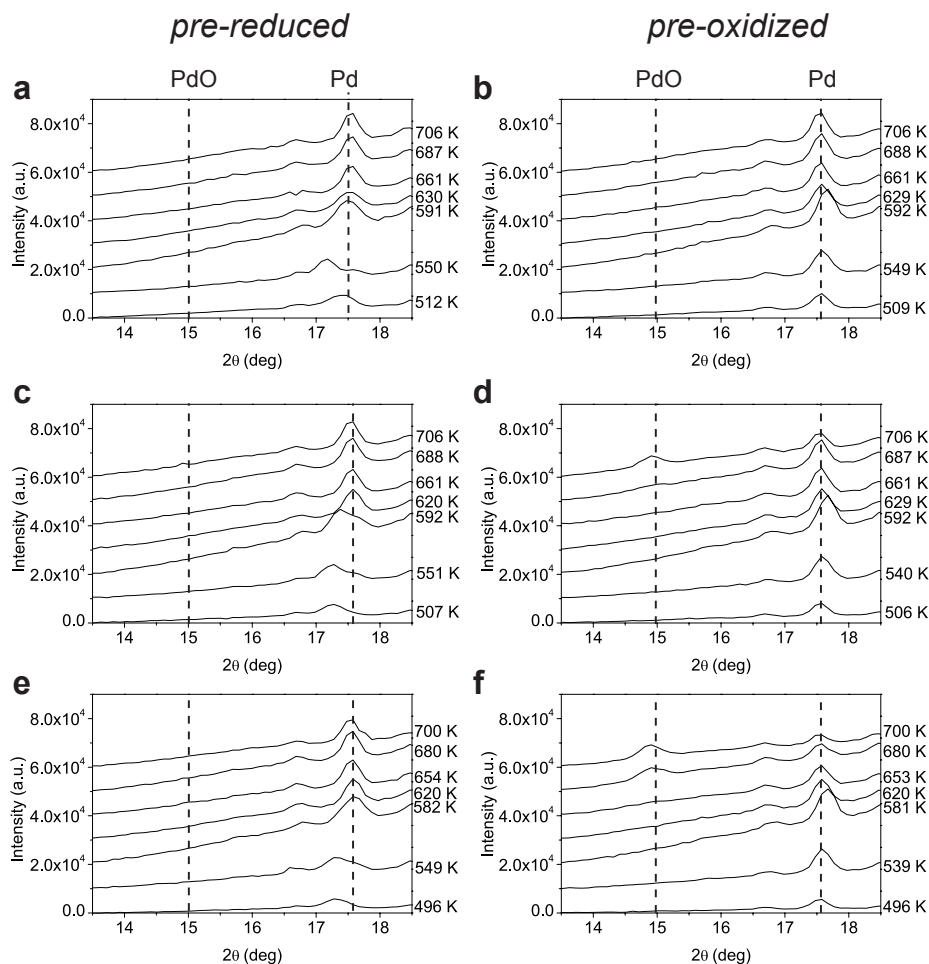
Figure 5.2: Powder diffraction patterns from the 15 nm Pd particles on SiO$_2$ for different temperatures at different gas conditions. **a)**,**c)**, and **e)** show the results after the pre-reducing the particles with pure CO and then supplying $P_{O_2}/P_{CO} = 0.6, 2$, and 10 respectively. **b)**, **d)**, and **f)** show results after the pre-oxidizing the particles and then supplying at $P_{O_2}/P_{CO} = 0.6$, 2, and 10 respectively. Dotted lines indicate the theoretical position of the PdO(101) reflection at 15° and the Pd(111) reflection at 17.6°. We have not been able to identify the small peak at 16.7°, but it is likely coming from the substrate. Subsequent curves are offset by 10^4 a.u. for clarity.

5.3.2 Spontaneous reaction oscillations

SiO$_2$ support

Spontaneous oscillations of the reaction rate can be seen in Fig. 5.3. The diffracted intensity was measured at a 2θ angle of 17.6°. It shows that the amount of metallic Pd was oscillating with less metallic Pd present in the high CO_2 producing phase of the oscillations. Figure 5.4 shows the intensity of the PdO at a 2θ angle of 15° which is oscillating in antiphase with the Pd signal, confirming that a part of the Pd is converted to PdO. However during the oscillations on the particles the amount of PdO never reduces to zero during the low CO_2 production regime. This is different from the situation on extended Pd(100) surfaces where the oxide is compeletely reduced during the low CO_2 production part of the oscillation cycle. The explanation for this difference could be a size dependent oxidation of the Pd nanoparticles [113, 127]. The larger particles reduce more easily than the smaller particles in this scenario, causing the larger particles to participate in the oscillations and small particles to remain oxidized. This scenario is unlikely because for particles of 15 nm in diameter no significant size effect is observed in ref. [113]. Another more likely explanation is the formation of an interface oxide between the SiO_2 and the Pd nanoparticles [113, 127]. A scenario where this interface oxide is not participating in the oscillations could then explain the remaining PdO intensity in our measurements. We observed that the remaining PdO was reduced in a pure CO atmosphere after the oscillations.

The apparent size of the particles during the reaction oscillations can be determined from the Scherrer equation:

$$\tau = \frac{K\lambda}{\beta_{\text{FWHM}}\cos(\theta)}, \tag{5.1}$$

where τ is a linear dimension of the particles, K is the Scherrer constant, λ is the x-ray wavelength, β_{FWHM} is the FWHM of the diffraction peak in radians, and θ is the Bragg angle [128]. The Scherrer constant K relates the apparent particle size given by:

$$\varepsilon = \frac{\lambda}{\beta_{\text{FWHM}}\cos(\theta)}, \tag{5.2}$$

to a linear dimension of the particle τ via a volume average of the thickness of the particle as measured perpendicular to the reflecting planes [128]. The Scherrer constant K thus depends on the shape of the particle, but it also depends on

the size distribution of the particles [129] and on the way the peak width is determined. Since the shape and the size distribution during the measurement is not accurately known we choose to show only the apparent size of the particles. This apparent size of the metallic part of the particles can be seen to oscillate between 11.5 nm and 12.5 nm. The systematic error in the determination of the apparent size is 0.8 nm. The Scherrer constant for converting apparent size as determined from using β_{FWHM} to the particle diameter, assuming a spherical shape, is 0.84. Also accounting for the width of the size distribution determined after the experiment (Fig. 5.5) would change the Scherrer constant to 0.77. The real size of the (metallic core of the) particles can thus differ substantially from the apparent size. The 1 nm variation in apparent size is converted to a 0.77 nm variation of the particle size. Note that we measured the thickness off the particles in the direction 8.5° off the surface normal of the SiO_2 support. The intensity variations in Fig. 5.3 and Fig. 5.4 together with the assumption of spherical particles with an average radius of 7.5 nm are consistent with the a formation and reduction of a 0.8 nm PdO shell during the oscillations.

The the measurements are thus consistent with the interface oxide scenario where the particles are metallic with an interface oxide underneath the particles in the regime of low CO_2 production and they adopt the form of a smaller metallic core within an oxide shell and an interface oxide underneath the particles in high CO_2 production regime. Apart from the remaining oxide the presence of an interface oxide, this scenario is analogous to that on the extended Pd(100) surface.

It is likely that the synchronization of the oscillations over the whole sample is caused by concentration changes in the CO pressure close to the sample. If one particle switches from the metallic to the more active oxidic phase, locally the CO pressure drops and the surrounding particles are also forced to oxidise. Conversely, if all the particles are oxidized, and one particle switches to the metallic phase the CO pressure locally increases, thereby forcing the surrounding particles to reduce.

Since the oxidation of the particles could be accompanied by shape changes, GISAXS measurements were performed to obtain information on the dimensions of the particles during the oscillations. However a narrowly peaked size distribution is of paramount importance for obtaining an accurate GISAXS fit of the average particle radius and height. Figure 5.5 shows a SEM image of the particles supported on SiO_2 after the experiments described above. The exposure of
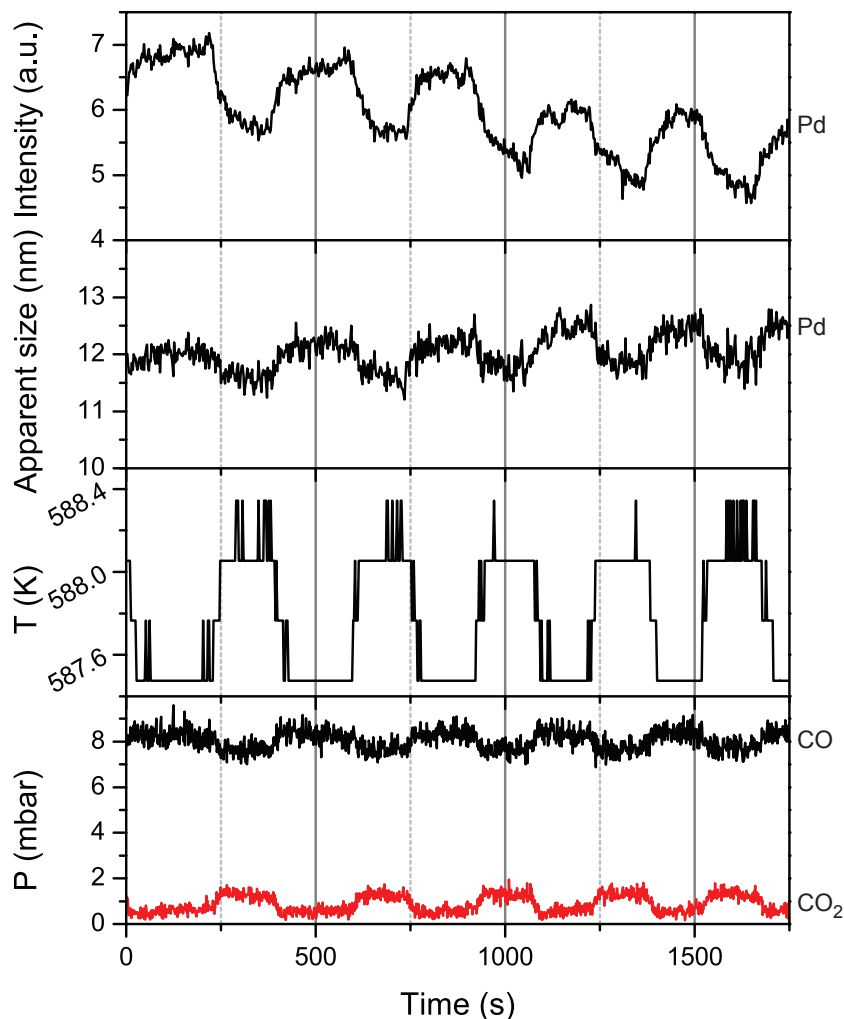
Figure 5.3: Spontaneous oscillations during CO oxidation on the 15 nm diameter Pd particles supported on SiO_2. Measurements were performed in a constant flow of a $CO/O_2/Ar$ gas mixture with an O_2 pressure of 210 mbar, an argon pressure of 281 mbar and a CO pressure of 9 mbar flowing at 50 ml_n min^{-1}. The mass spectrometry signals from CO and CO_2 show that the reaction rate oscillates (lower panel), which in turn makes the temperature vary (third panel). Note that the temperature variations amount to just a few times the least significant bit of the digitized temperature scale. The top two panels show the diffracted intensity from the Pd particles ($2\theta = 17.6°$) and the apparent Pd nanocrystal size, derived from the diffraction line widths.
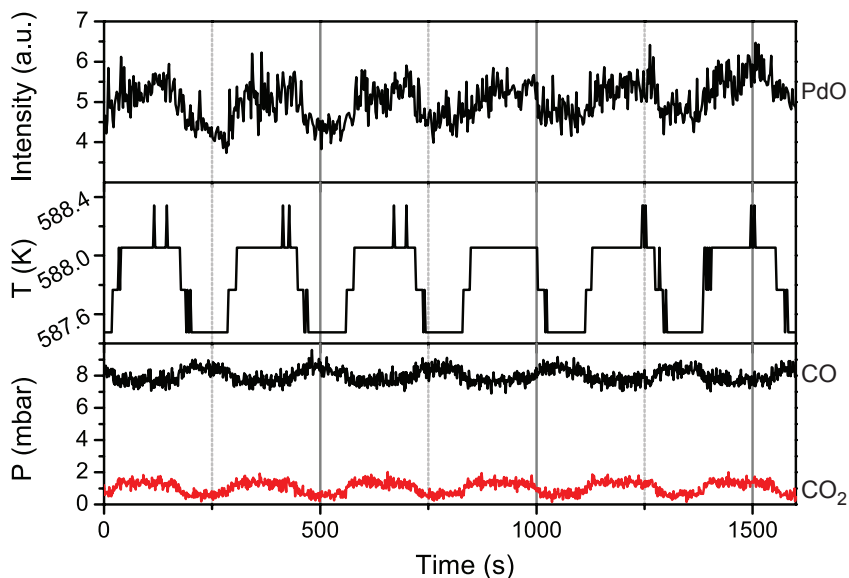
Figure 5.4: Spontaneous oscillations in the CO oxidation rate on the 15 nm diameter Pd particles supported on SiO_2 as measured by XRD and mass spectrometry. Measurements were performed in a constant flow of a $CO/O_2/Ar$ gas mixture with an O_2 pressure of 210 mbar, an argon pressure of 281 mbar and a CO pressure of 9 mbar flowing at 50 ml_n min^{-1}. The mass spectrometry signals from CO and CO_2 show that the reaction rate oscillates (lower panel), which in turn makes the temperature vary second panel). Note that the temperature variations amount to just a few times the least significant bit of the digitized temperature scale. The top panel shows the diffracted intensity from PdO ($2\theta = 14.9°$).

the sample to reactant gasses at high temperatures led to a significant widening of the size distribution from $\frac{\sigma_R}{R} = 0.05$ to $\frac{\sigma_R}{R} = 0.19$, see Fig. 5.5b. Widening of the size distribution can be caused by two effects [130, 131]. The first effect is Ostwald ripening where large particles grow at the expense of smaller particles due to higher vapour pressure of the smaller particles as described by the Gibbs-Thomson equation. The second effect is called Smoluchowski ripening or dynamic coalescence and describes the coarsening caused by diffusion and coalescence of complete particles [132]. From our size distribution we conclude that both Ostwald ripening and Smoluchowski ripening have been important. The importance of Ostwald ripening can be inferred from the fact that we see many par-
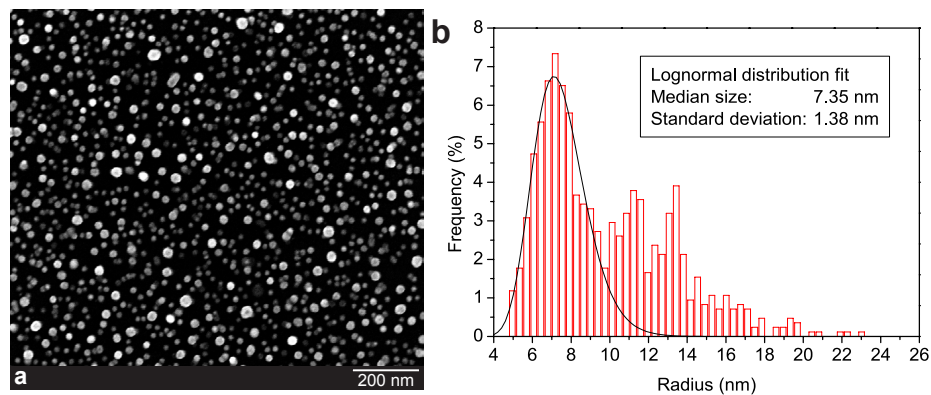
Figure 5.5: a) SEM image of the 15 nm Pd particles deposited on SiO_2. This image was taken after the sample had been in the reactor for the experiments of Figs. 5.1 to 5.4. **b)** Size distribution of the particles as determined from 854 particles in the SEM data after the reaction oscillations.

ticles with a smaller radius than the monodisperse 7.5 nm with which we started. The importance of Smoluchowski ripening can be inferred from the fact that we see multiple peaks in our size distribution at radii that one would expect for either 2, 3, or 4 particles with a 7.5 nm radius coalescing. Fits of the GISAXS for the average particle size for the sample shown in Fig. 5.5 give very large uncertainty in the average radius and height due the the wide size distribution.

Al_2O_3 support

Spontaneous reaction oscillations where also observed for the case of 15 nm Pd particles on Al_2O_3. The intensity variation of the diffracted intensity at a 2θ angle of 17.6° are shown in Fig. 5.6. Assuming the particles are perfectly spherical, the variations in intensity are consistent with the formation and reduction of a 1.0 nm oxide shell during the oscillations. The apparent size is measured 8.5° from the surface normal of the Al_2O_3 and is thus a good measure for the average height of the metallic part of a particle if multiplied by the appropriate Scherrer constant. Assuming the Scherrer constant for a perfect sphere (0.84) the height of the metallic part of a particle varies between 8.8 nm and 9.7 nm. The systematic error in the apparent size determination is 0.8 nm. Intensity variations in the PdO (not shown) signal at $2\theta = 15°$ show the presence of PdO in the high CO_2
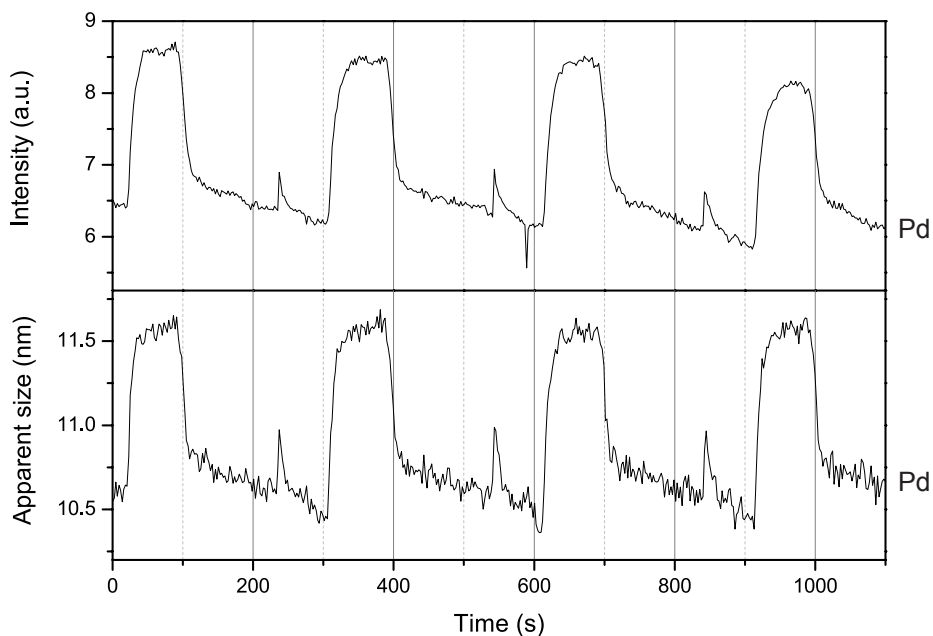
Figure 5.6: Spontaneous oscillations in the CO oxidation rate on the 15 nm diameter Pd particles supported on Al_2O_3. Measurements were performed in a constant flow of a $CO/O_2/Ar$ gas mixture with an O_2 pressure of 210 mbar, an Ar pressure of 281 mbar and a CO pressure of 9 mbar flowing at 50 ml_n min^{-1}. The two panels show the diffracted intensity from the Pd particles ($2\theta = 17.6°$) and the apparent Pd nanocrystal size, derived from the diffraction line widths.

production regime, but PdO is not observed in the low CO_2 production regime.

The size distribution of the 15 nm Pd particles supported on Al_2O_3 remained narrower ($\frac{\sigma_R}{R} \approx 0.1$) during the oscillations and thus resulted in a more meaning-ful fit of the particle dimensions than for the particles supperted on SiO_2. The non-conducting Al_2O_3 substrate however, caused charging of the particles in the scanning electron microscope preventing a determination of the size distribution by SEM. Figure 5.7 shows reaction oscillations of the Pd nanoparticles supported on Al_2O_3. At four points in this scan GISAXS data were analysed: (1) just be-fore the switch to low CO_2 production, (2) directly after the switch from high to to low CO_2 production, (3) just before the switch to high CO_2 production,(4) directly after the switch to high CO_2 production.
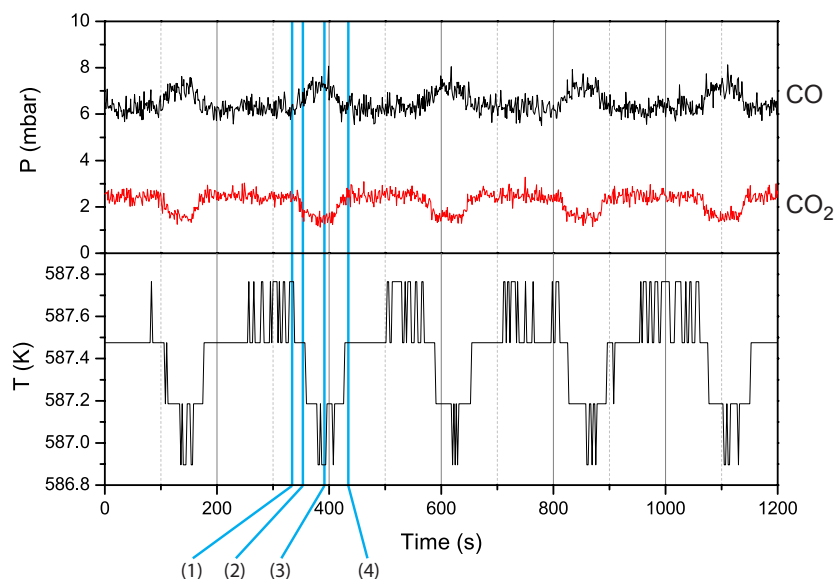
Figure 5.7: Top panel: spontaneous oscillations in the CO oxidation rate on the 15 nm diameter Pd particles supported on Al_2O_3 as measured by mass spectrometry. Bottom panel: sample temperature. Measurements were performed in a constant flow of a $CO/O_2/Ar$ gas mixture with an O_2 pressure of 210 mbar, an Ar pressure of 281 mbar and a CO pressure of 9 mbar flowing at 50 ml_n min^{-1}.

A selection of the GISAXS data and the GISAXS fits are shown in Fig. 5.8. The fits were made using the IsGISAXS progam [133]. The fit of the particle dimensions was made assuming that the particles consist fully of Pd in both phases. From the diffraction data we know that this assumption is not completely justified, since some part of the Pd in the particles is transformed to PdO. In principle we would like to know whether an oxide shell exists around the particles and how thick this shell is, or where the oxide is located otherwise. Ideally we would prefer to base our fits on a geometry in which the PdO is added as a layer of homogeneous thickness on a Pd core, while the amount of Pd is conserved. Such a non-linear constraint is difficult to impose using the IsGISAXS program, so instead we chose to make a fit of the dimensions of the particles, assuming the particles are truncated spheres and a have constant density throughout. The
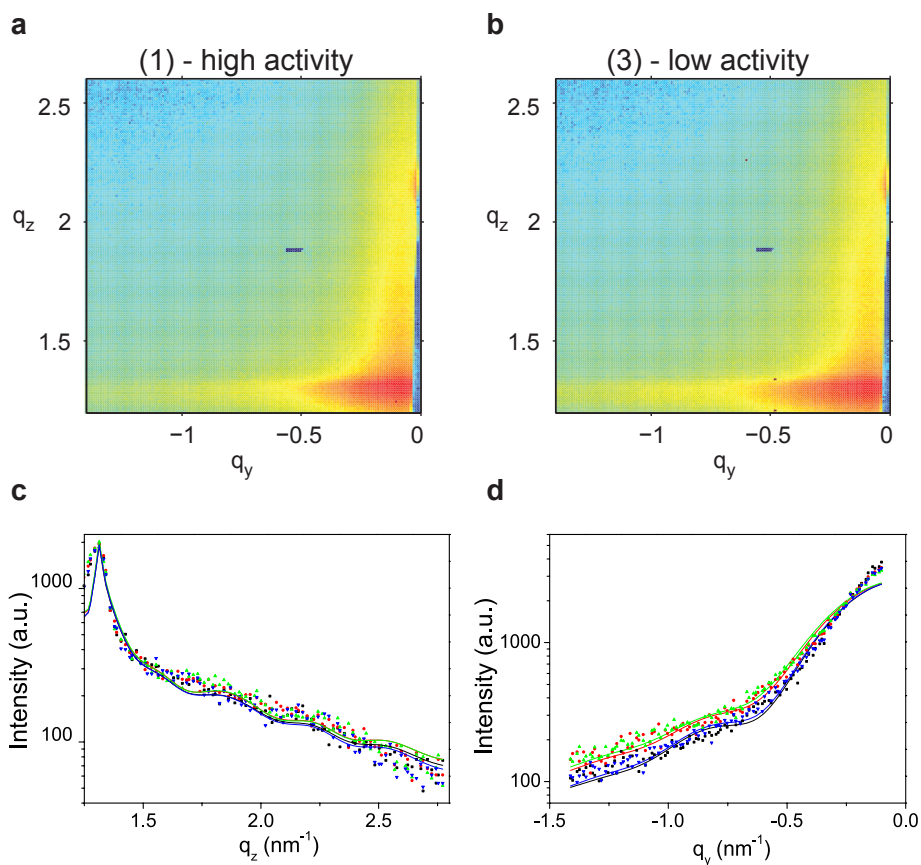
Figure 5.8: GISAXS data and fits at the times indicated in Fig. 5.7. **a)** GISAXS data taken in the high CO_2 production phase at (1) in Fig. 5.7, **b)** GISAXS data taken in the low CO_2 production phase at (3) in Fig. 5.7. **c)** Perpendicular cross section of GISAXS data (1)-black, (2)-red, (3)-green, (4)-blue and fits **d)** Parallel cross section of GISAXS data (1-4) and fits.

GISAXS patterns change most during the switch from high to low CO_2 production and back. Most change is visible in the extent of the Yoneda peak in the q_y direction, which is reduced in the high-activity phase. This change can be fitted well width a modest change of the average particle radius. The best-fit parameters are shown in Table 5.1. H is not a fit parameter, but is calculated from H/R and R. The particles are slightly larger in the high CO_2 production phase. This is consistent with a scenario where the particles are partly oxidized in the high reactivity regime, because the partial oxidation should cause a volume increase of the particles. Note that a radius increase of the particle by 0.16 nm between (3) and (4) in Table 5.1 means that the oxide is a factor $\rho_{Pd}/(\rho_{Pd} - \rho_{PdO}) \approx 3$ thicker. The 0.16 nm increase in radius from the GISAXS fits thus indicates that a ~ 0.5 nm thin oxide exists on the particle during the high CO_2 production, that thickness corresponds to two layers of PdO(101). We note that the uncertainty in the determination of the radius is much larger than this 0.16 nm and interpret the radius increase merely as a qualitative effect.

Assuming a spherical shape, these fit results also seem to suggest that the contact angle of the particles with the Al_2O_3 substrate is slightly smaller in the high reactivity regime. We would like to stress that what we measure and fit is the average behaviour of the ensemble of particles. The measurements do not exclude a scenario in which for example small particles are covered in a thicker oxide than large particles.

Table 5.1: GISAXS parameters for the fits in Fig. 5.8 to the data obtained at the four times (1)-(4) indicated in Fig. 5.7. R is the average particle radius, σ_R the standard deviation of the radius and H the average height.

	R (nm)	$\frac{\sigma_R}{R}$	H (nm)	$\frac{H}{R}$
(1)	7.49 ± 0.88	9.63×10^{-2}	13.41 ± 2.40	1.79 ± 0.11
(2)	7.40 ± 1.03	9.94×10^{-2}	13.47 ± 2.54	1.82 ± 0.09
(3)	7.32 ± 1.11	1.02×10^{-1}	13.40 ± 2.69	1.83 ± 0.09
(4)	7.48 ± 0.87	9.51×10^{-2}	13.46 ± 2.31	1.80 ± 0.10

When we compare the height of the particles of (13.4 ± 2.4) nm as determined by GISAXS with the height from the diffraction line widths of (9.7 ± 0.8) nm we find a discrepancy of 3.7 nm. The existence of an interface compound consisting could account for this discrepancy. Since we do not detect PdO in the diffraction
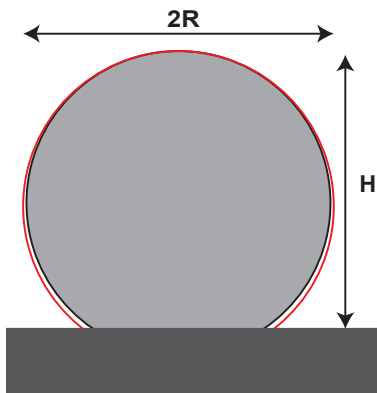
Figure 5.9: Black: average shape of the Pd particles in the low CO_2 production phase as determined by GISAXS. Red: average shape of the partly oxidized Pd particles in the high CO_2 production phase as determined by GISAXS.

data in the low CO_2 production regime, we suspect that we are dealing with Pd aluminate interface compound.

Furthermore we observed an influence of the presence of the x-ray beam on the period of the oscillations. Removal of the x-ray beam during the oscillations resulted in an increase of the oscillation period from 3.0×10^2 s to 7.0×10^2 s. We also observe a temperature decrease of $1.2\,°C$ after removal of the beam and an increase in the temperature amplitude of the oscillations from $0.7\,°C$ to $1.2\,°C$. Changing the temperature by this amount without removing the beam did not result in a change of the oscillation period. The x-rays thus have a real effect on the speed of the oscillations. The increase in the temperature amplitude suggests a larger difference in reactivity between the high and low CO_2 production parts of an oscillation period. The high CO_2 production part of the oscillation period is mass transfer limited, so we only expect to see slightly lower CO_2 signal in the low CO_2 production part of the period, compared to the situation with presence of the x-ray beam. Such an effect is indeed visible in the mass spectrometer.

5.4 Conclusion

We have shown that significant amounts of bulk-like PdO are only present on supported 15 nm particles if we pre-oxidise the particles, before doing the steady state reactivity measurements and that the detection of surface oxides on nanoparticles under catalytic conditions remains a challenge.

We have also shown that 15 nm Pd particles supported on Al_2O_3 and SiO_2 show self sustained reaction oscillations. During these oscillations the particles go from a metallic to a partly oxidized state and they change radius. The measurements are consistent with the formation and reduction of a 0.5 nm to 1.0 nm thick PdO shell around a Pd core. A marked difference between the oscillations exhibited by the nanoparticles supported on SiO_2 with the oscillations on single-crystal Pd(100) is that on the nanoparticle samples part of the PdO is not reduced in the low CO_2 production regime. An interface oxide between the particles and the substrate could explain this difference. For the Pd particles supported on Al_2O_3 an interface compound between the particle and the substrate also seems to be present, but the structure of this compound could not be determined. The driving mechanism for the oscillations could be similar to the roughening mechanism on the Pd(100) single crystal. Unfortunately probing the roughness, or perhaps more appropriately, the degree of imperfection, of and oxide covering a particle, remains an experimental challenge. We believe that the use of supported monodisperse nanoparticles in combination with XRD and GISAXS constitutes a powerful method of studying the in situ shape of nanoparticles.

Appendix A

On the possible hyperactivity of metal surfaces for CO oxidation

This appendix covers part of the ongoing discussion about active surface phases and the role of oxide for CO oxidation on Pd. The discussion arose as a result of the apparently irreconcilable difference between STM and SXRD measurements [23, 51, 91, 105] and PM-IRAS measurements [73, 134–136]. A consistent interpretation of our SXRD and STM data and the PM-IRAS results of Goodman is presented.

Recently, Goodman and co-workers [73, 134–136] have challenged our interpretation [23, 51, 91, 105] of catalytic CO oxidation at atmospheric pressures, namely that at high O_2/CO pressure ratios Pd and Pt surfaces switch from a metallic structure to a surface oxide with a higher catalytic activity. On the basis of turnover frequencies (TOFs) and polarization modulation infrared absorption spectroscopy (PM-IRAS), Goodman et al. claim that an intermediate metallic phase dominated by chemisorbed oxygen is chemically even more active. In this comment we provide a natural, alternative explanation for the observations in refs [73, 134–136], which we support with new TOF data and structural measurements obtained with surface x-ray diffraction (SXRD).

In refs [73, 134–136], metal crystals were heated inside a large batch reactor, filled with an O_2/CO mixture. Figure A.1 reproduces Figure 5 of ref [73], showing the TOF on Pd(100), obtained from the decay rate of the total pressure for several initial O_2/CO ratios. Consistent with our scanning tunneling microscopy (STM) [51, 91, 105] and SXRD [23] observations, the low temperature branches in Fig. A.1 are identified in ref [73] as the regime where Pd(100) is metallic with adsorbed CO and O [51]. The TOF increased with temperature up to a plateau, which is taken as the signature of a mass-transfer limited regime, in which the flux of CO molecules diffusing to the surface directly determines the observed TOF. Our observations had shown such plateaus to concur with the presence of an oxide at the surface and we had argued that this would change the reaction mechanism [23, 51, 91, 105].

The arrows indicate transient peaks in reaction rate, occurring immediately before the TOF settled at the plateau and showing that temporarily Pd(100) was able to convert more CO than the mass-transfer limit of the plateaus. In ref [73], this is taken as evidence for an intermediate surface structure. The PM-IRAS data show no signal from adsorbed CO during the TOF peaks from which ref [73] concludes that the intermediate structure should be metallic Pd(100) with an O-dominated adsorption layer.

In Fig. A.1b, we have repeated these TOF measurements in a flow-reactor setup [78] that combines mass spectrometry and SXRD. Our results were obtained under steady-state conditions with the temperatures and O_2/CO ratios carefully following those in Fig. A.1a. In Fig. A.1b, all plateaus are at the same TOF since we added argon to keep the total pressure constant, thereby keeping the diffusion coefficient of CO through the gas mixture at the same value for all O_2/ CO ratios. Transient peaks are absent under the steady-state conditions of Fig. A.1b;
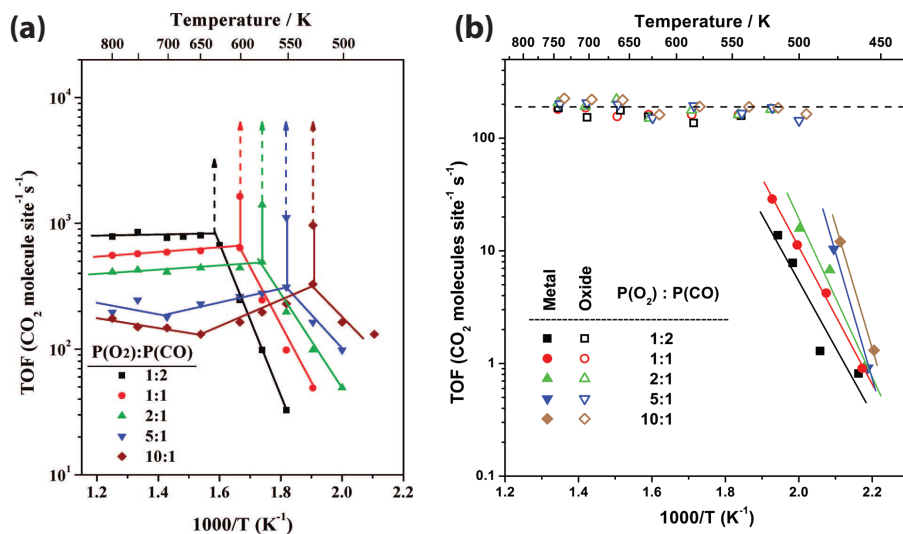
Figure A.1: a) Arrhenius plots of the CO_2 formation rate measured by Gao et al. [73] for several O_2/CO mixtures over Pd(100), each mixture starting from an initial CO partial pressure of 8 Torr. Transient reaction rate jumps are indicated with arrows. Data reprinted from ref. [73]. **b)** Equivalent data set, measured in a flow reactor-SXRD setup. The CO pressure was 8 Torr for all ratios, but argon was added to the gas mixture to keep the total pressure constant at 152 Torr. The surface structure was determined simultaneously with the reactivity by surface x-ray diffraction. Open symbols denote where the SXRD measurements showed the presence of an oxide (surface oxide, bulk oxide, or powder pattern) and solid symbols indicate under which conditions SXRD measured an oxide-free metal surface.

they only occur during the transition from metal to oxide, as was the case in Fig. A.1a. We note, that transient peaks have also not been observed in any of the measurements of refs [73, 134–136] in the reverse direction, when the oxide was reduced. Our SXRD measurements identify the structure of the Pd(100) surface at each of the conditions in Fig. A.1b. We have resolved a variety of oxide structures at detailed account of which is provided in Chapter 3; in Fig. A.1b all oxide structures are indicated by open symbols. The solid symbols are for conditions where all Pd atoms were on regular Pd lattice positions, that is, for a metallic surface. We see that the oxide and metal structures separate in a very simple way; all cases with a mass-transfer limited TOF correspond to an oxide,

while all lower-temperature observations of temperature dependent TOF values correspond to metallic Pd(100). In search for an intermediate structure, we have driven the surface many times through the metal-oxide phase transition by changing either the temperature or the O_2/CO ratio. Using a pixel camera, the time for the SXRD structure identification was reduced to 1 s and even at this time scale we find the increase in TOF to correlate with the appearance of an oxide without any sign of an intervening structure.

We suggest an alternative explanation for the transient TOF peaks. In the limit of zero reactivity, the concentration profile of CO in the reactor is completely flat, while in the limit of infinite reactivity, there is a strong gradient with a zero local CO concentration at the surface. Therefore, when the surface switches from slow to fast CO consumption, the concentration profile must change from a weak to a strong gradient. This naturally leads to transient TOF behavior, precisely of the type in refs [73, 134–136]. As long as the new profile has not been established fully, the CO concentration in the gas close to the surface has not yet reduced fully to its new, lower value and the flux of CO impinging and reacting to CO_2 is exceedingly high. The excess TOF over the full transient adds up to the reduction in total amount of CO in the reactor between the profiles before and after the switch. This scenario not only explains the transient peaks when switching from a low to a high TOF, but also the absence of transient peaks in the reverse direction. Then, the CO concentration near the surface is initially lower than the appropriate concentration for the new, lower-reactivity metal phase, so that a negative transient should occur with an even lower TOF. Within the experimental noise, the TOF-plots in refs [73, 134–136] are fully consistent with this.

The duration of the transient peaks reflects the settling time for the new profile, which is either dictated by the system's mass-transfer properties or by the intrinsic reactivity of the catalytic surface. We estimate that in refs [73, 134–136], the characteristic diffusional mass-transfer time should be below 1 s. The significantly longer durations observed, for example, 8 s in Figure 11 of ref [73], suggest that they stem from the combination of the high surface reactivity of the newly formed oxide, the significant overshoot in temperature resulting from the reactivity jump, and the correspondingly strong convective gas flow.

Finally, we compare the PM-IRAS observations of adsorbed CO, which Goodman and co-workers used to obtain information on the catalyst's surface structure, with direct SXRD. When the TOF was low and temperature-dependent, PM-IRAS showed CO adsorbed in bridge sites on metallic Pd(100), consistent

with our SXRD observation of a well ordered metal surface. Under most gas mixtures at higher temperature, during the transient TOF-peak and on the subsequent plateau, no adsorbed CO was detected in the infrared spectra, indicating high catalytic activity. Figure A.1b shows oxidic surfaces under all these conditions. Low CO coverages have been found on oxidized Pt particles in the in situ measurements of [117]. Only for highly oxygen-rich mixtures infrared signals of CO returned, characteristic for CO on bulk PdO [73] Under these conditions, SXRD showed a polycrystalline, bulklike PdO film, whereas we found epitaxial surface oxide structures under less oxygen rich conditions. We speculate that each of the oxides formed on Pd(100) has a different reactivity, in most cases beyond the mass-transfer limit, and that the bulk-like PdO is less active than the other oxides.

We conclude by pointing out that our own experimental findings and our interpretation of the PM-IRAS results, including those concerning the low CO coverage on the surface oxide, closely agree with recent kinetic Monte Carlo calculations with energies derived from DFT calculations [71].

Bibliography

In the digital version of this thesis the bibliography items contain hyperlinks to their online locations where possible.

[1] D. A. King, *Chemisorption on metals: a personal review*, Surface Science **299-300**, 678 (1994).

[2] H. Davy, *Some New Experiments and Observations on the Combustion of Gaseous Mixtures, with an Account of a Method of Preserving a Continued Light in Mixtures of Inflammable Gases and Air without Flame*, Philosophical Transactions of the Royal Society of London **107**, 77 (1817).

[3] J. J. Berzelius, *Considerations respecting a New Power which acts in the Formation of Organic Bodies*, Edinburgh New Philosophical Journal **21**, 223 (1836).

[4] Acmite Market Intelligence, *Market Report: Global Catalyst Market*, (2011).

[5] G. Ertl, *Reactions at surfaces: from atoms to complexity*, Nobel Lecture, (2007).

[6] C. Stampfl, M. V. Ganduglia-Pirovano, K. Reuter, and M. Scheffler, *Catalysis and corrosion: the theoretical surface-science context*, Surface Science **500**, 368 (2002).

[7] I. K. Robinson and D. J. Tweet, *Surface X-ray diffraction*, Reports on Progress in Physics **55**, 599 (1992).

[8] R. Feidenhans'l, *Surface structure determination by X-ray diffraction*, Surface Science Reports **10**, 105 (1989).

[9] I. Langmuir, *Chemical reactions at low pressures 1*, Journal of the American Chemical Society **37**, 1139 (1915).

[10] P. Mars and D. van Krevelen, *Oxidations carried out by means of vanadium oxide catalysts*, Chemical Engineering Science **3**, 41 (1954).

[11] G. Renaud, R. Lazzari, and F. Leroy, *Probing surface and interface morphology with Grazing Incidence Small Angle X-Ray Scattering*, Surface Science Reports **64**, 255 (2009).

[12] G. A. Somorjai, *Introduction to Surface Chemistry and Catalysis* (Wiley, New York, 1994).

[13] G. Ertl, H. Knözinger, and J. Weitkamp, eds., *Handbook of Heterogeneous Catalysis* (Wiley, New York, 1997).

[14] H. Over, Y. D. Kim, A. P. Seitsonen, S. Wendt, E. Lundgren, M. Schmid, P. Varga, A. Morgante, and G. Ertl, *Atomic-Scale Structure and Catalytic Reactivity of the $RuO_2(110)$ Surface*, Science **287**, 1474 (2000).

[15] N. Lopez, T. V. W. Janssens, B. S. Clausen, Y. Xu, M. Mavrikakis, T. Bligaard, and J. K. Nørskov, *On the origin of the catalytic activity of gold nanoparticles for low-temperature CO oxidation*, Journal of Catalysis **223**, 232 (2004).

[16] A. Stierle and A. Molenbroek, *Novel In Situ Probes for Nanocatalysis*, MRS Bulletin **32**, 1001 (2007).

[17] T. W. Hansen, J. B. Wagner, P. L. Hansen, S. Dahl, H. Topsøe, and C. J. H. Jacobsen, *Atomic-Resolution in Situ Transmission Electron Microscopy of a Promoter of a Heterogeneous Catalyst*, Science **294**, 1508 (2001).

[18] P. B. Rasmussen, B. L. M. Hendriksen, H. Zeijlemaker, H. G. Ficke, and J. W. M. Frenken, *The "Reactor STM": A scanning tunneling microscope for investigation of catalytic surfaces at semi-industrial reaction conditions*, Review of Scientific Instruments **69**, 3879 (1998).

[19] F. Tao, D. Tang, M. Salmeron, and G. A. Somorjai, *A new scanning tunneling microscope reactor used for high-pressure and high-temperature catalysis studies*, Review of Scientific Instruments **79**, 084101 (2008).

[20] D. F. Ogletree, H. Bluhm, G. Lebedev, C. S. Fadley, Z. Hussain, and M. Salmeron, *A differentially pumped electrostatic lens system for photoemission studies in the millibar range*, Review of Scientific Instruments **73**, 3872 (2002).

[21] P. Bernard, K. Peters, J. Alvarez, and S. Ferrer, *Ultrahigh vacuum/high pressure chamber for surface x-ray diffraction experiments*, Review of Scientific Instruments **70**, 1478 (1999).

[22] M.-C. Saint-Lager, A. Bailly, P. Dolle, R. Baudoing-Savois, P. Taunier, S. Garaudee, S. Cuccaro, S. Douillet, O. Geaymond, G. Perroux, O. Tissot, J.-S. Micha, O. Ulrich, and F. Rieutord, *New reactor dedicated to in operando studies of model catalysts by means of surface x-ray diffraction and grazing incidence small angle x-ray scattering*, Review of Scientific Instruments **78**, 083902 (2007).

[23] M. D. Ackermann, T. M. Pedersen, B. L. M. Hendriksen, O. Robach, S. C. Bobaru, I. Popa, C. Quiros, H. Kim, B. Hammer, S. Ferrer, and J. W. M. Frenken, *Structure and Reactivity of Surface Oxides on Pt(110) during Catalytic CO Oxidation*, Physical Review Letters **95**, 255505 (2005).

[24] J. Gustafson, R. Westerström, A. Mikkelsen, X. Torrelles, O. Balmes, N. Bovet, J. N. Andersen, C. J. Baddeley, and E. Lundgren, *Sensitivity of catalysis to surface structure: The example of CO oxidation on Rh under realistic conditions*, Physical Review B: Condensed Matter and Materials Physics **78**, 045423 (2008).

[25] N. Kasper, A. Stierle, P. Nolte, Y. Jin-Phillipp, T. Wagner, D. de Oteyza, and H. Dosch, *In situ oxidation study of MgO(100) supported Pd nanoparticles*, Surface Science **600**, 2860 (2006).

[26] H. Over, O. Balmes, and E. Lundgren, *Direct comparison of the reactivity of the non-oxidic phase of Ru(0001) and the RuO_2 phase in the CO oxidation reaction*, Surface Science **603**, 298 (2009).

[27] K. C. Taylor, *Nitric Oxide Catalysis in Automotive Exhaust Systems*, Catalysis Reviews: Science and Engineering **35**, 457 (1993).

[28] C. Stegelmann, N. Schiødt, C. Campbell, and P. Stoltze, *Microkinetic modeling of ethylene oxidation over silver*, Journal of Catalysis **221**, 630 (2004).

[29] R. Pitchai and K. Klier, *Partial Oxidation of Methane*, Catalysis Reviews: Science and Engineering **28**, 13 (1986).

[30] J. Wieckowska, *Catalytic and adsorptive desulphurization of gases*, Catalysis Today **24**, 405 (1995).

[31] G. P. van der Laan and A. A. C. M. Beenackers, *Kinetics and Selectivity of the Fischer-Tropsch Synthesis: A Literature Review*, Catalysis Reviews: Science and Engineering **41**, 255 (1999).

[32] HUBER Diffraktionstechnik GmbH, www.huber.de.

[33] Brush Wellman Beryllium Products, www.berylliumproducts.com.

[34] D. E. Nowak, D. R. Blasini, A. M. Vodnick, B. Blank, M. W. Tate, A. Deyhim, D.-M. Smilgies, H. Abruna, S. M. Gruner, and S. P. Baker, *Six-circle diffractometer with atmosphere- and temperature-controlled sample stage and area and line detectors for use in the G2 experimental station at CHESS*, Review of Scientific Instruments **77**, 113301 (2006).

[35] O. Sakata, Y. Tanaka, A. M. Nikolaenko, and H. Hashizume, *Ultrahigh-Vacuum Facility for High-Resolution Grazing-Angle X-ray Diffraction at a Vertical Wiggler Source of Synchrotron Radiation*, Journal of Synchrotron Radiation **5**, 1222 (1998).

[36] Jetseal, Inc., www.jetseal.com.

[37] Varian S.p.A., www.varianinc.com.

[38] Omicron NanoTechnology GmbH, www.omicron.de.

[39] SPECS GmbH, www.specs.de.

[40] Arun Microelectronics Limited, www.arunmicro.com.

[41] MKS Instruments France, www.mksinst.com.

[42] Pfeiffer Vacuum France, www.pfeiffer-vacuum.fr.

[43] Métaux Céramiques Systèmes Engineering, www.mcse.fr.

[44] Saint-Gobain Advanced Ceramics, www.bn.saint-gobain.com.

[45] Bronkhorst High-Tech B.V., www.bronkhorst.com.

[46] Sigma-Aldrich Chimie S.a.r.l., www.sigmaaldrich.com.

[47] Certified Scientific Software, www.certif.com.

[48] D. R. Lide, ed., *CRC Handbook of Chemistry and Physics* (CRC, Boca Raton, 1994).

[49] A. Stierle, N. Kasper, H. Dosch, E. Lundgren, J. Gustafson, A. Mikkelsen, and J. N. Andersen, *A surface x-ray study of the structure and morphology of the oxidized Pd(001) surface*, The Journal of Chemical Physics **122**, 044706 (2005).

[50] M. D. Ackermann, *Operando SXRD: A New View on Catalysis*, Ph.D. thesis, Leiden University (2007).

[51] B. L. M. Hendriksen, Ş. C. Bobaru, and J. W. M. Frenken, *Oscillatory CO oxidation on Pd(100) studied with in situ scanning tunneling microscopy*, Surface Science **552**, 229 (2004).

[52] Leiden Probe Microscopy B.V., www.leidenprobemicroscopy.com.

[53] P. Gai, E. Boyes, S. Helveg, P. Hansen, S. Giorgio, and C. Henry, *Atomic-Resolution Environmental Transmission Electron Microscopy for Probing Gas-Solid Reactions in Heterogeneous Catalysis*, MRS Bulletin **32**, 1044 (2007).

[54] B. L. M. Hendriksen and J. W. M. Frenken, *The Reactor-STM: A Real-Space Probe for Operando Nanocatalysis*, MRS Bulletin **32**, 1015 (2007).

[55] H. Bluhm, M. Hävecker, A. Knop-Gericke, M. Kiskinova, R. Schlögl, and M. Salmeron, *In Situ X-Ray Photoelectron Spectroscopy Studies of Gas-Solid Interfaces at Near-Ambient Conditions*, MRS Bulletin **32**, 1022 (2007).

[56] G. Rupprechter, *Sum Frequency Laser Spectroscopy during Chemical Reactions on Surfaces*, MRS Bulletin **32**, 1031 (2007).

[57] S. Ferrer, M. Ackermann, and E. Lundgren, *In Situ Investigations of Chemical Reactions on Surfaces by X-Ray Diffraction at Atmospheric Pressures*, MRS Bulletin **32**, 1010 (2007).

[58] J. Kašpar, P. Fornasiero, and N. Hickey, *Automotive catalytic converters: current status and some perspectives*, Catalysis Today **77**, 419 (2003).

[59] M. Lyubovsky and L. Pfefferle, *Methane combustion over the [alpha]-alumina supported Pd catalyst: Activity of the mixed Pd/PdO state*, Applied Catalysis, A: General **173**, 107 (1998).

[60] M. Todorova, E. Lundgren, V. Blum, A. Mikkelsen, S. Gray, J. Gustafson, M. Borg, J. Rogal, K. Reuter, J. N. Andersen, and M. Scheffler, *The Pd(100)-R27°-O surface oxide revisited*, Surface Science **541**, 101 (2003).

[61] P. Kostelník, N. Seriani, G. Kresse, A. Mikkelsen, E. Lundgren, V. Blum, T. Sikola, P. Varga, and M. Schmid, *The surface oxide: A LEED, DFT and STM study*, Surface Science **601**, 1574 (2007).

[62] N. Seriani, J. Harl, F. Mittendorfer, and G. Kresse, *A first-principles study of bulk oxide formation on Pd(100)*, The Journal of Chemical Physics **131**, 054701 (2009).

[63] G. Zheng and E. I. Altman, *The oxidation mechanism of Pd(100)*, Surface Science **504**, 253 (2002).

[64] J. Wang, Y. Yun, and E. Altman, *The plasma oxidation of Pd(100)*, Surface Science **601**, 3497 (2007).

[65] J. Han, D. Y. Zemlyanov, and F. H. Ribeiro, *Interaction of O_2 with Pd single crystals in the range 1-150 Torr: Surface morphology transformations*, Surface Science **600**, 2730 (2006).

[66] R. Westerström, M. E. Messing, S. Blomberg, A. Hellman, H. Grönbeck, J. Gustafson, N. Martin, O. Balmes, R. van Rijn, J. N. Andersen, K. Deppert, H. Bluhm, Z. Liu, M. Grass, M. Hävecker, and E. Lundgren, *Oxidation and reduction of Pd(100) and aerosol-deposited Pd nanoparticles*,

Physical Review B: Condensed Matter and Materials Physics **83**, 115440 (2011).

[67] E. Lundgren, J. Gustafson, A. Mikkelsen, J. N. Andersen, A. Stierle, H. Dosch, M. Todorova, J. Rogal, K. Reuter, and M. Scheffler, *Kinetic Hindrance during the Initial Oxidation of Pd(100) at Ambient Pressures*, Physical Review Letters **92**, 046101 (2004).

[68] J. Rogal, K. Reuter, and M. Scheffler, *Thermodynamic stability of PdO surfaces*, Physical Review B: Condensed Matter and Materials Physics **69**, 075421 (2004).

[69] J. T. Hirvi, T.-J. J. Kinnunen, M. Suvanto, T. A. Pakkanen, and J. K. Nørskov, *CO oxidation on PdO surfaces*, The Journal of Chemical Physics **133**, 084704 (2010).

[70] J. Rogal, K. Reuter, and M. Scheffler, *CO oxidation at Pd(100) : A first-principles constrained thermodynamics study*, Physical Review B: Condensed Matter and Materials Physics **75**, 205433 (2007).

[71] J. Rogal, K. Reuter, and M. Scheffler, *CO oxidation on Pd(100) at technologically relevant pressure conditions: First-principles kinetic Monte Carlo study*, Physical Review B: Condensed Matter and Materials Physics **77**, 155410 (2008).

[72] B. L. M. Hendriksen, M. D. Ackermann, R. van Rijn, D. Stoltz, I. Popa, O. Balmes, A. Resta, D. Wermeille, R. Felici, S. Ferrer, and J. W. M. Frenken, *The role of steps in surface catalysis and reaction oscillations*, Nature Chemistry **2**, 730 (2010).

[73] F. Gao, Y. Wang, Y. Cai, and D. W. Goodman, *CO Oxidation on Pt-Group Metals from Ultrahigh Vacuum to Near Atmospheric Pressures. 2. Palladium and Platinum*, The Journal of Physical Chemistry C **113**, 174 (2009).

[74] R. van Rijn, O. Balmes, R. Felici, J. Gustafson, D. Wermeille, R. Westerström, E. Lundgren, and J. W. M. Frenken, *Comment on 'CO Oxidation on Pt-Group Metals from Ultrahigh Vacuum to Near Atmospheric Pressures. 2. Palladium and Platinum'*, The Journal of Physical Chemistry C **114**, 6875 (2010).

[75] F. Gao, Y. Wang, and D. W. Goodman, *Reply to "Comment on 'CO Oxidation on Pt-Group Metals from Ultrahigh Vacuum to Near Atmospheric Pressures. 2. Palladium and Platinum' "*, The Journal of Physical Chemistry C **114**, 6874 (2010).

[76] M. Chen, X. V. Wang, L. Zhang, Z. Tang, and H. Wan, *Active Surfaces for CO Oxidation on Palladium in the Hyperactive State*, Langmuir **26**, 18113 (2010).

[77] O. Balmes, R. van Rijn, D. Wermeille, A. Resta, L. Petit, H. Isern, T. Dufrane, and R. Felici, *The ID03 surface diffraction beamline for in-situ and real-time X-ray investigations of catalytic reactions at surfaces*, Catalysis Today **145**, 220 (2009).

[78] R. van Rijn, M. D. Ackermann, O. Balmes, T. Dufrane, A. Geluk, H. Gonzalez, H. Isern, E. de Kuyper, L. Petit, V. A. Sole, D. Wermeille, R. Felici, and J. W. M. Frenken, *Ultrahigh vacuum/high-pressure flow reactor for surface x-ray diffraction and grazing incidence small angle x-ray scattering studies close to conditions for industrial catalysis*, Review of Scientific Instruments **81**, 014101 (2010).

[79] X. Llopart, M. Campbell, R. Dinapoli, D. San Segundo, and E. Pernigotti, *Medipix2: A 64-k pixel readout chip with 55 μm square elements working in single photon counting mode*, IEEE Transactions on Nuclear Science **49**, 2279 (2002).

[80] C. Ponchut, J. Clément, J.-M. Rigal, E. Papillon, J. Vallerga, D. LaMarra, and B. Mikulec, *Photon-counting X-ray imaging at kilohertz frame rates*, Nuclear Instruments and Methods in Physics Research Section A: Accelerators, Spectrometers, Detectors and Associated Equipment **576**, 109 (2007).

[81] C. Ponchut, J. M. Rigal, J. Clément, E. Papillon, A. Homs, and S. Petitdemange, *MAXIPIX, a fast readout photon-counting X-ray area detector for synchrotron applications*, Journal of Instrumentation **6**, C01069 (2011).

[82] J. Szanyi and D. W. Goodman, *CO Oxidation on Palladium. 1. A Combined Kinetic-Infrared Reflection Absorption Spectroscopic Study of Pd(100)*, The Journal of Physical Chemistry **98**, 2972 (1994).

[83] S. Matera and K. Reuter, *First-Principles Approach to Heat and Mass Transfer Effects in Model Catalyst Studies*, Catalysis Letters **133**, 156 (2009).

[84] H. S. Taylor, *A theory of the catalytic surface*, Proceedings of the Royal Society of London A **108**, 105 (1925).

[85] J. T. Yates, *Surface chemistry at metallic defect sites*, Journal of Vacuum Science & Technology A **13**, 1359 (1995).

[86] B. Hammer, O. H. Nielsen, and J. K. Nørskov, *Structure sensitivity in adsorption: CO interaction with stepped and reconstructed Pt surfaces*, Catalysis Letters **46**, 31 (1997).

[87] T. Zambelli, J. Wintterlin, J. Trost, and G. Ertl, *Identification of the "Active Sites" of a Surface-Catalyzed Reaction*, Science **273**, 1688 (1996).

[88] S. Dahl, A. Logadottir, R. C. Egeberg, J. H. Larsen, I. Chorkendorff, E. Törnqvist, and J. K. Nørskov, *Role of Steps in N_2 Activation on Ru(0001)*, Physical Review Letters **83**, 1814 (1999).

[89] J. J. C. Geerlings, J. H. Wilson, G. J. Kramer, H. P. C. E. Kuipers, A. Hoek, and H. M. Huisman, *Fischer-Tropsch technology – from active site to commercial process*, Applied Catalysis A: General **186**, 27 (1999).

[90] R. T. Vang, K. Honkala, S. Dahl, E. K. Vestergaard, J. Schnadt, E. Lægsgaard, B. S. Clausen, J. K. Nørskov, and F. Besenbacher, *Controlling the catalytic bond-breaking selectivity of Ni surfaces by step blocking*, Nature Materials **4**, 160 (2005).

[91] B. L. M. Hendriksen and J. W. M. Frenken, *CO oxidation on Pt(110): scanning tunneling microscopy inside a flow reactor*, Physical Review Letters **89**, 046101 (2002).

[92] K. Reuter and M. Scheffler, *First-principles atomistic thermodynamics for oxidation catalysis: surface phase diagrams and catalytically interesting regions*, Physical Review Letters **90**, 046103 (2003).

[93] B. L. M. Hendriksen, Ş. C. Bobaru, and J. W. M. Frenken, *Bistability and oscillations in CO oxidation studied with scanning tunneling microscopy inside a reactor*, Catalysis Today **105**, 234 (2005).

[94] R. Imbihl and G. Ertl, *Oscillatory kinetics in heterogeneous catalysis*, Chemical Reviews **95**, 697 (1995).

[95] F. Schüth, B. Henry, and L. Schmidt, *Oscillatory Reactions in Heterogeneous Catalysis*, edited by H. P. D.D. Eley and P. B. Weisz, Advances in Catalysis, Vol. 39 (Academic Press, 1993) pp. 51 – 127.

[96] I. K. Robinson, *Crystal truncation rods and surface roughness*, Physical Review B: Condensed Matter and Materials Physics **33**, 3830 (1986).

[97] C. Wagner, *The formation of thin oxide films on metals*, Corrosion Science **13**, 23 (1973).

[98] J. Klikovits, M. Schmid, L. R. Merte, P. Varga, R. Westerström, A. Resta, J. N. Andersen, J. Gustafson, A. Mikkelsen, E. Lundgren, F. Mittendorfer, and G. Kresse, *Step-Orientation-Dependent Oxidation: From 1D to 2D Oxides*, Physical Review Letters **101**, 266104 (2008).

[99] P. Thostrup, E. Christoffersen, H. T. Lorensen, K. W. Jacobsen, F. Besenbacher, and J. K. Nørskov, *Adsorption-Induced Step Formation*, Physical Review Letters **87**, 126102 (2001).

[100] Y. Zhang, J. Rogal, and K. Reuter, *Density-functional theory investigation of oxygen adsorption at Pd(11N) vicinal surfaces (N=3,5,7): influence of neighboring steps*, Physical Review B: Condensed Matter and Materials Physics **74**, 125414 (2006).

[101] E. D. Williams and N. C. Bartelt, *Thermodynamics of surface morphology*, Science **251**, 393 (1991).

[102] B. C. Sales, J. E. Turner, and M. B. Maple, *Oscillatory oxidation of CO over Pt, Pd and Ir catalysts: theory*, Surface Science **114**, 381 (1982).

[103] Ş. C. Bobaru, *High-pressure STM studies of oxidation catalysis*, Ph.D. thesis, Leiden University (2006).

[104] B. L. M. Hendriksen, *Model Catalysts in Action – High-Pressure Tunneling Microscopy*, Ph.D. thesis, Leiden University (2003).

[105] B. L. M. Hendriksen, Ş. C. Bobaru, and J. W. M. Frenken, *Looking at Heterogeneous Catalysis at Atmospheric Pressure Using Tunnel Vision*, Topics in Catalysis **36**, 43 (2005).

[106] T. Holy, J. Jakubek, S. Pospisil, J. Uher, D. Vavrik, and Z. Vykydal, *Data acquisition and processing software package for Medipix2*, Nuclear Instruments and Methods in Physics Research Section A: Accelerators, Spectrometers, Detectors and Associated Equipment **563**, 254 (2006).

[107] G. Nicolis and J. Portnow, *Chemical oscillations*, Chemical Reviews **73**, 365 (1973).

[108] T. S. Briggs and W. C. Rauscher, *An oscillating iodine clock*, Journal of Chemical Education **50**, 496 (1973).

[109] N. Hartmann, R. Imbihl, and W. Vogel, *Experimental evidence for an oxidation/reduction mechanism in rate oscillations of catalytic CO oxidation on Pt/SiO$_2$*, Catalysis Letters **28**, 373 (1994).

[110] P.-A. Carlsson, V. P. Zhdanov, and M. Skoglundh, *Self-sustained kinetic oscillations in CO oxidation over silica-supported Pt*, Physical Chemistry Chemical Physics **8**, 2703 (2006).

[111] J. Sá, D. L. A. Fernandes, F. Aiouache, A. Goguet, C. Hardacre, D. Lundie, W. Naeem, W. P. Partridge, and C. Stere, *SpaciMS: spatial and temporal operando resolution of reactions within catalytic monoliths*, Analyst **135**, 2260 (2010).

[112] P. Nolte, A. Stierle, N. Y. Jin-Phillipp, N. Kasper, T. U. Schulli, and H. Dosch, *Shape Changes of Supported Rh Nanoparticles During Oxidation and Reduction Cycles*, Science **321**, 1654 (2008).

[113] T. Schalow, B. Brandt, D. E. Starr, M. Laurin, S. K. Shaikhutdinov, S. Schauermann, J. Libuda, and H.-J. Freund, *Size-Dependent Oxidation Mechanism of Supported Pd Nanoparticles*, Angewandte Chemie International Edition **45**, 3693 (2006).

[114] K. Zorn, S. Giorgio, E. Halwax, C. R. Henry, H. Grönbeck, and G. Rupprechter, *CO Oxidation on Technological Pd-Al$_2$O$_3$ Catalysts: Oxidation State and Activity*, The Journal of Physical Chemistry C **115**, 1103 (2011).

[115] E. H. Voogt, *Pd model catalysts*, Ph.D. thesis, Utrecht University (1997).

[116] H. Borchert, B. Jürgens, V. Zielasek, G. Rupprechter, S. Giorgio, C. Henry, and M. Bäumer, *Pd nanoparticles with highly defined structure on MgO as model catalysts: An FTIR study of the interaction with CO, O$_2$, and H$_2$ under ambient conditions*, Journal of Catalysis **247**, 145 (2007).

[117] J. Singh, E. M. C. Alayon, M. Tromp, O. V. Safonova, P. Glatzel, M. Nachtegaal, R. Frahm, and J. A. van Bokhoven, *Generating Highly Active Partially Oxidized Platinum during Oxidation of Carbon Monoxide over Pt/Al$_2$O$_3$: In Situ, Time-Resolved, and High-Energy-Resolution X-Ray Absorption Spectroscopy*, Angewandte Chemie International Edition **47**, 9260 (2008).

[118] A. Iglesias-Juez, A. Kubacka, M. Fernandez-Garcia, M. Di Michiel, and M. A. Newton, *Nanoparticulate Pd Supported Catalysts: Size-Dependent Formation of Pd(I)/Pd(0) and Their Role in CO Elimination*, Journal of the American Chemical Society **133**, 4484 (2011).

[119] M. E. Messing, R. Westerström, B. O. Meuller, S. Blomberg, J. Gustafson, J. N. Andersen, E. Lundgren, R. van Rijn, O. Balmes, H. Bluhm, and K. Deppert, *Generation of Pd Model Catalyst Nanoparticles by Spark Discharge*, The Journal of Physical Chemistry C **114**, 9257 (2010).

[120] G. Renaud, A. Barbier, and O. Robach, *Growth, structure, and morphology of the Pd/MgO(001) interface: Epitaxial site and interfacial distance*, Physical Review B: Condensed Matter and Materials Physics **60**, 5872 (1999).

[121] C. Revenant, F. Leroy, R. Lazzari, G. Renaud, and C. R. Henry, *Quantitative analysis of grazing incidence small-angle x-ray scattering: Pd/MgO(001) growth*, Physical Review B: Condensed Matter and Materials Physics **69**, 035411 (2004).

[122] N. W. Cant, P. Hicks, and B. Lennon, *Steady-state oxidation of carbon monoxide over supported noble metals with particular reference to platinum*, Journal of Catalysis **54**, 372 (1978).

[123] P. J. Berlowitz, C. H. F. Peden, and D. W. Goodman, *Kinetics of carbon monoxide oxidation on single-crystal palladium, platinum, and iridium*, The Journal of Physical Chemistry **92**, 5213 (1988).

[124] N. Krishnankutty and M. A. Vannice, *The Effect of Pretreatment on Pd/C Catalysts : I. Adsorption and Absorption Properties*, Journal of Catalysis **155**, 312 (1995).

[125] M. Maciejewski and A. Baiker, *Incorporation and reactivity of carbon in palladium*, Pure & Applied Chemistry **67**, 1879 (1995).

[126] S. B. Ziemecki, G. A. Jones, D. G. Swartzfager, R. L. Harlow, and J. Faber, *Formation of interstitial palladium-carbon phase by interaction of ethylene, acetylene, and carbon monoxide with palladium*, Journal of the American Chemical Society **107**, 4547 (1985).

[127] B. Brandt, T. Schalow, M. Laurin, S. Schauermann, J. Libuda, and H.-J. Freund, *Oxidation, Reduction, and Reactivity of Supported Pd Nanoparticles: Mechanism and Microkinetics*, The Journal of Physical Chemistry C **111**, 938 (2007).

[128] A. R. Stokes and A. J. C. Wilson, *A method of calculating the integral breadths of Debye-Scherrer lines*, Mathematical Proceedings of the Cambridge Philosophical Society **38**, 313 (1942).

[129] J. I. Langford and A. J. C. Wilson, *Scherrer after sixty years: A survey and some new results in the determination of crystallite size*, Journal of Applied Crystallography **11**, 102 (1978).

[130] E. Ruckenstein and B. Pulvermacher, *Growth kinetics and the size distributions of supported metal crystallites*, Journal of Catalysis **29**, 224 (1973).

[131] M. Jak, C. Konstapel, A. van Kreuningen, J. Verhoeven, and J. Frenken, *Scanning tunnelling microscopy study of the growth of small palladium particles on TiO$_2$(110)*, Surface Science **457**, 295 (2000).

[132] M. Smoluchowski, *Drei Vorträge über Diffusion, Brownsche Molekular-bewegung und Koagulation von Kolloidteilchen*, Physikalische Zeitschrift **17**, 557 (1916).

[133] R. Lazzari, *IsGISAXS: a program for grazing-incidence small-angle X-ray scattering analysis of supported islands*, Journal of Applied Crystallography **35**, 406 (2002).

[134] F. Gao, Y. Cai, K. K. Gath, Y. Wang, M. S. Chen, Q. L. Guo, and D. W. Goodman, *CO Oxidation on Pt-Group Metals from Ultrahigh Vacuum to Near Atmospheric Pressures. 1. Rhodium*, The Journal of Physical Chemistry C **113**, 182 (2009).

[135] F. Gao, S. McClure, Y. Cai, K. Gath, Y. Wang, M. Chen, Q. Guo, and D. Goodman, *CO oxidation trends on Pt-group metals from ultrahigh vacuum to near atmospheric pressures: A combined in situ PM-IRAS and reaction kinetics study*, Surface Science **603**, 65 (2009).

[136] S. M. McClure and D. W. Goodman, *New insights into catalytic CO oxidation on Pt-group metals at elevated pressures*, Chemical Physics Letters **469**, 1 (2009).

Samenvatting

Katalysatoren zijn in onze samenleving van essentieel belang en worden in de chemische industrie gebruikt om een veelheid aan chemische reacties gunstiger te laten verlopen. Voor onder andere de ontzwaveling van benzine, de productie van plastics en van kunstmest zijn we afhankelijk van katalyse. Een katalysator is, kort gezegd, een stof die behulpzaam is bij een chemische reactie zonder daarbij zelf te worden verbruikt.

De reactie die bestudeerd wordt in dit proefschrift is de katalytische oxidatie van koolstofmonoxide (CO) met zuurstof (O_2) tot koolstofdioxide (CO_2). Dit is één van de reacties die plaatsvindt in die éne katalysator die iedereen kent, de autokatalysator. Deze bestaat uit een poreuze drager waarop het actieve materiaal, meestal een edelmetaal zoals palladium, in de vorm van nanodeeltjes* is aangebracht. Omdat de reagerende stoffen in dit geval gasvormig zijn en de katalysator 'vast' is spreken we van heterogene katalyse. Dit in contrast met homogene katalyse, waarbij de reagerende stoffen en de katalysator zich in dezelfde fase bevinden. Ze zijn dan bijvoorbeeld allebei vloeibaar. In het geval van heterogene katalyse vindt de reactie tussen de reagerende stoffen plaats op het *oppervlak* van het katalytisch actieve materiaal. De katalysator bindt de reagerende stoffen aan zijn oppervlak (adsorptie) en maakt bepaalde stoffen zelfs stuk door een chemische binding aan te gaan (dissociatieve adsorptie). De gebonden stoffen kunnen over het oppervlak bewegen (diffusie), met elkaar reageren en vervolgens het oppervlak weer verlaten (desorptie). Een goede katalysator bindt de reagerende stoffen wel, maar niet te sterk. In de autokatalysator kan het bijvoorbeeld onder bepaalde condities gebeuren dat het katalytisch actieve oppervlak volledig bedekt is met CO moleculen, daardoor is er géén ruimte meer voor de dissociatieve adsorptie van zuurstof moleculen en doet de katalysator zijn werk niet meer. We spreken dan van 'vergiftiging' van de katalysator. Het kan ook zijn dat de katalysator een ongewenste reactie versnelt. Een autokatalysator mag bijvoorbeeld niet zorgen voor makkelijke oxidatie van stikstof uit de lucht, want dat veroorzaakt

---

*Deeltjes met een typische afmeting van 1-100 nanometer. Een nanometer is een miljardste meter.

smog! De mate waarin een katalysator één reactie versnelt en een ander juist niet wordt de 'selectiviteit' genoemd.

Katalytisch actieve materialen, en zeker edelmetalen zoals palladium, zijn vaak erg duur. Door het katalytisch actieve materiaal in de vorm van nanodeeltjes te deponeren, creëert men zoveel mogelijk katalytisch actief oppervlak per hoeveelheid materiaal. Door de de hoge temperaturen die heersen in een katalysator kunnen deze nanodeeltjes samenklonteren. Dit proces zorgt voor een geleidelijk prestatieverlies van de katalysator.

Om nu goed te kunnen bestuderen hoe deze processen op atomaire schaal op het katalysatoroppervlak verlopen gebruikt men vaak vereenvoudigde katalysatoren. Zo'n modelkatalysator is in ons geval een perfect vlak gepolijst en ultrazuiver stukje palladium waarvan de palladiumatomen allemaal netjes op dezelfde wijze geordend zijn. Veel technieken om dit soort preparaten te bestuderen met atomair detail werken alleen in ultrahoog-vacuüm of bij zeer lage gasdruk van de reagerende gassen. Het is inmiddels gebleken dat bij die lage drukken de katalysator zich niet altijd hetzelfde gedraagt als onder de reactieomstandigheden die gebruikt worden in de industrie of in ons geval in de auto. Deze discrepantie noemen we de drukkloof of 'pressure gap'. Om echt inzicht te krijgen in het gedrag van katalysatoren moeten we dus met atomaire precisie naar het katalysatoroppervlak kijken terwijl de reactie daadwerkelijk plaatsvindt onder realistische reactieomstandigheden. Veel van de technieken die gebaseerd zijn op de verstrooiing van elektronen of ionen aan het preparaat, werken dan niet, omdat de elektronen en ionen sterk verstrooien aan het gas dat onder deze condities noodzakelijkerwijs boven het oppervlak zit. Oppervlakte-röntgendiffractie, de techniek die gebruikt wordt in dit proefschrift, is wel een uitermate geschikte techniek omdat de röntgenstraling nauwelijks verstrooit aan de gasmoleculen. We kunnen met deze techniek inzicht krijgen in de ordening van de atomen van het preparaat. Doordat er maar weinig atomen deel uitmaken van het materiaaloppervlak hebben we veel röntgenstraling nodig voor een goede meting. Dat is de reden dat alle metingen zijn gedaan bij het ESRF, een synchrotron of deeltjesversneller die speciaal is gebouwd om intense röntgenstraling te produceren.

De ontwikkeling van een reactor die gemonteerd kan worden in de oppervlakteröntgendiffractiebundellijn (ID03) staat beschreven in hoofdstuk 2. In deze reactor kunnen we preparaten goed schoon maken met ultrahoog-vacuüm technieken. Daarna kunnen we het oppervlak blootstellen aan een continue stroom van gassen onder atmosferische drukken en hoge temperaturen in een kleine reactor met

wanden van beryllium. De röntgenbundel schiet makkelijk door deze beryllium-wanden heen, en daardoor kunnen we het oppervlak tijdens de reactie bestuderen. Verder lekt er vanuit de reactor een minuscule hoeveelheid gas terug naar het ultrahoog-vacuüm zodat we met een massaspectrometer de samenstelling van het gas in de reactor kunnen meten. We kunnen op deze manier dus de reactiviteit van de modelkatalysator correleren met de oppervlaktestructuur.

In hoofdstuk 3 hebben we voor één bepaald preparaat, Pd(100)† onder een groot aantal condities de oppervlaktestructuur en de reactiviteit van het oppervlak bepaald. We hebben ontdekt dat het oppervlak bij lage temperaturen metallisch is, maar dat er vanaf een bepaalde temperatuur een dun palladiumoxidelaagje wordt gevormd aan het oppervlak. Afhankelijk van de hoeveelheid zuurstof die aanwezig is in de gasstroom is dit: een laagje van slechts één atoom dik bij een lage hoeveelheid zuurstof, een 'rommelige' dikke laag oxide bij een grote hoeveelheid zuurstof en tussenliggende situatie met een net geordend oxide van een aantal lagen dik. De reactiviteitsmetingen geven aan dat de CO_2 productie, zoals verwacht, oploopt met het verhogen van de temperatuur op het metallische oppervlak, maar dat de CO_2 productie maximaal is -en blijft- in de aanwezigheid van om het even welk laagje palladiumoxide. Het oppervlak met een laagje oxide erop is dus in staat alle CO die we aan het oppervlak aanbieden om te zetten. Dat geeft enkele problemen, want de 'echte' reactiviteit kan zo niet gemeten worden en eventuele verschillen tussen de verschillende laagjes oxide ook niet. Het resultaat is verrassend omdat men dacht dat geoxideerd palladium een slechtere katalysator voor de oxidatie van koolstofmonoxide zou zijn dan metallisch palladium. De resultaten zijn dan ook een waardevolle toevoeging aan de discussie hierover. Een deel van deze discussie staat beschreven in appendix A.

De blootstelling van het Pd(100) preparaat aan zuurstof en koolstofmonoxide bij een bepaalde constante temperatuur leidt tot zogenaamde spontane reactie-oscillaties. De productie van CO_2 springt met min of meer regelmatige periodes van een honderdtal secondes van een hoog naar laag, en weer terug. Het systeem gedraagt zich in feite als chemische klok. In hoofdstuk 4 wordt aangetoond dat het oppervlak periodiek springt van een gereduceerde toestand (een metallisch oppervlak) met een lage CO_2 productie, naar een geoxideerde toestand met een hoge CO_2 productie. De drijvende kracht achter dit fenomeen blijkt de oppervlakteruwheid te zijn. Het koolstofmonoxide reageert met de zuurstofatomen uit

---

†Pd staat voor palladium. De notatie (100) geeft kristaloriëntatie van het oppervlak aan.

de palladiumoxidelaag. De ontbrekende zuurstofatomen in de oxidelaag worden weer aangevuld met zuurstof uit de gastroom, maar het laagje palladiumoxide verruwt tijdens dit proces. Nu blijkt uit onze metingen dat het oxidelaagje bij een bepaalde ruwheid niet meer stabiel is. Het zuurstoflaagje verdwijnt dan en het oppervlak keert terug naar de metallische toestand. In eerste instantie is dit metallische oppervlak ruw, maar doordat palladiumatomen wat vrijheid hebben om over het oppervlak te bewegen wordt het oppervlak langzaam vlakker. Op een gegeven moment is het oppervlak zo vlak dat zich weer een net laagje oxide kan vormen en begint een nieuwe periode van de oscillatie.

In alle hierboven beschreven experimenten hebben we vlakke oppervlakken als modelkatalysator gebruikt, terwijl een echte katalysator uit nanodeeltjes bestaat. Er kunnen grote verschillen zijn tussen het gedrag van metalen nanodeeltjes en het gedrag van vlakke metaaloppervlakken. Het oppervlak waarop de deeltjes liggen kan bijvoorbeeld invloed uitoefenen op de vorm van de deeltjes, door de kleine kromtestraal van de deeltjes zijn er palladiumatomen met een verminderd aantal buuratomen en deze 'rand' kan zich katalytisch anders gedragen. Door dit soort effecten bestaat er een materialenkloof, ook wel 'materials gap' genoemd. Om deze effecten te bestuderen hebben we in hoofdstuk 5 preparaten gebruikt van vlak siliciumoxide en aluminiumoxide met daarop palladium nanodeeltjes met een diameter van van 15 nanometer. Doordat er nu geen sprake meer is van een perfect vlak palladiumoppervlak is het niet meer mogelijk gebruik te maken van oppervlakte-röntgendiffractie. In plaats daarvan kijken we nu naar de diffractiesignalen van gehele deeltjes en gebruiken we de kleine-hoek-verstrooiing van de röntgenbundel om de gemiddelde vorm van de deeltjes te bepalen. Het blijkt dat er ook spontane reactie-oscillaties optreden op de deeltjespreparaten. Wij zijn in staat geweest om te bepalen dat tijdens deze oscillaties zich een dunne schil van palladiumoxide vormt en weer verdwijnt. De ruwheid van deze schil kon echter niet worden bepaald. Wel hebben we gezien dat op het grensvlak van de deeltjes en het substraat zich een tussenlaag vormt. Deze laag bestaat waarschijnlijk uit palladium, zuurstof en het substraatmateriaal. Dat roept nieuwe en interessante vragen op over het belang van deze structuren voor katalyse en ook voor de invloed van de tussenstructuren op het veranderen van de verdeling van deeltjesgrootes.

Al met al is het werk beschreven in dit proefschrift erop gericht om de structurele en morfologische fenomenen die optreden tijdens de werking van palladium modelkatalysatoren onder realistische condities beter te begrijpen.

Acknowledgements

Although this thesis has only my name printed on the cover, at the basis of its contents lies the joint effort of many people. Here I take the opportunity to thank them all for their support, help, and advice.

My promotor Joost Frenken and co-promotor Roberto Felici were both a source of ideas, enthusiasm, and valuable advice during the whole project. The novel flow reactor was designed at the department of fine mechanics in Leiden by Arjen Geluk. Lucien Petit improved and extended upon that design at the ESRF in France. The commissioning of the setup in record time was only possible through the help I received from Thomas Dufrane and Helena Isern. Herve Gonzalez and Armando Sole made sure that the electronic components of the setup were properly interfaced with the rest of the beamline. Many measurement runs have yielded good results due to the encyclopaedic knowledge and skills of Didier Wermeille, and the resourcefulness of Olivier Balmes. Andrea Resta has helped me during uncountable night shifts.

The initial work of Marcelo Ackermann and Bas Hendriksen on the reaction oscillations provided me with a good start, and the experiments resulted in a nice article and a chapter of this thesis. During experiments in Grenoble I often got help from colleagues from Leiden and elsewhere: Dunja Stoltz, Kees Herbschleb, Marta Cañas Ventura, Violeta Navarro, Uta Hejral, and master-students-turned-colleagues Sander Roobol and Willem Onderwaater.

The succes of the collaboration with Edvin Lundgren, Johan Gustafson, and Rasmus Westerström from Lund University is well reflected in the publication list. Maria Messing kindly provided the monodisperse nanoparticles without which Chapter 5 would not have been written.

The fast polishing and delivery of a palladium crystal within 24 hours by Rene Koper saved us a week of valuable beamtime.

Finally I want to thank the whole IP-group for the all the stimulating work discussions.

List of publications

- *The active phase of palladium during methane oxidation,*
A. Hellman, A. Resta, N. M. Martin, J. Gustafson, A. Trinchero, P.-A. Carlsson, O. Balmes, R. Felici, R. van Rijn, J. W. M. Frenken, J. N. Andersen, E. Lundgren, and H. Grönbeck,
Journal of Physical Chemistry Letters **3**, 678682 (2012).

- *Reversible formation of a PdC_x phase in Pd nanoparticles upon CO and O_2 exposure,*
O. Balmes, A. Resta, D. Wermeille, R. Felici, M. E. Messing, K. Deppert, Z. Liu, M. E. Grass, H. Bluhm, R. van Rijn, E. Lundgren, R. Westerström, S. Blomberg, J. Gustafson, and J. N. Andersen,
Physical Chemistry Chemical Physics **14**, 4796-801 (2012).

- *Oxidation and reduction of Pd(100) and aerosol-deposited Pd nanoparticles,*
R. Westerström, M. E. Messing, S. Blomberg, A. Hellman, H. Grönbeck, J. Gustafson, N. M. Martin, O. Balmes, R. van Rijn, J. N. Andersen, K. Deppert, H. Bluhm, Z. Liu, M. E. Grass, M. Hävecker, and E. Lundgren,
Physical Review B: Condensed Matter and Materials Physics **83**, 115440 (2011).

- *Surface structure and reactivity of Pd(100) during CO oxidation near ambient pressures*,
R. van Rijn, O. Balmes, A. Resta, D. Wermeille, R. Westerström, J. Gustafson, R. Felici, E. Lundgren, and J. W. M. Frenken,
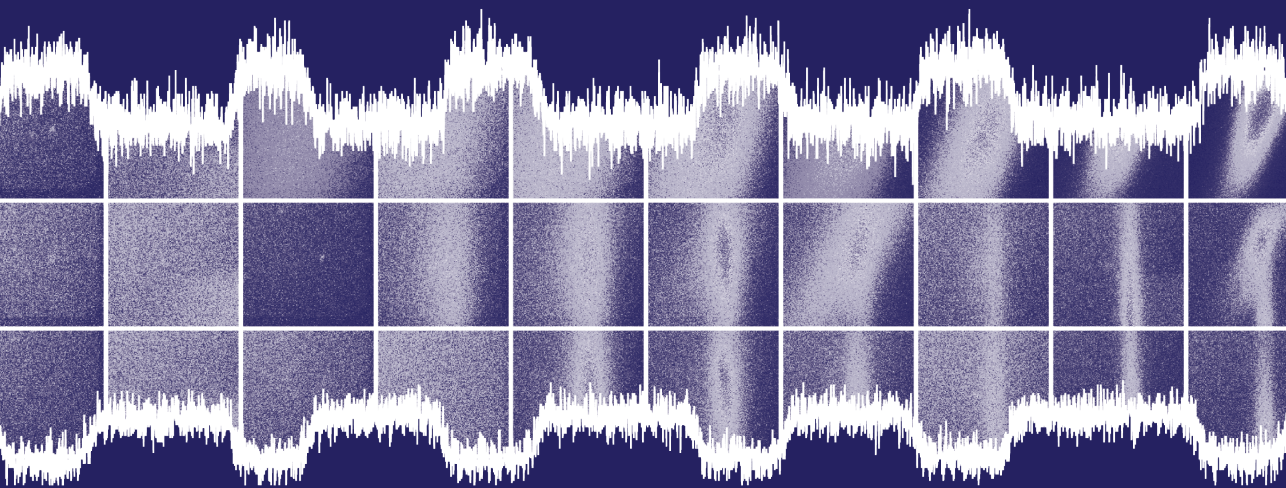Physical Chemistry Chemical Physics **13**, 13167-13171 (2011).

- *Generation of Pd model catalyst nanoparticles by spark discharge,*
  M. E. Messing, R. Westerström, B. O. Meuller, S. Blomberg, J. Gustafson,
  J. N. Andersen, E. Lundgren, R. van Rijn, O. Balmes, H. Bluhm, and K.
  Deppert,
  Journal of Physical Chemistry C **114**, 9257-9263 (2010).

- *A new role for steps in catalysis and reaction oscillations,*
  B. L. M. Hendriksen, M. D. Ackermann, R. van Rijn, D. Stoltz, I. Popa, O.
  Balmes, A. Resta, D. Wermeille, R. Felici, S. Ferrer, and J. W. M. Frenken,
  Nature Chemistry **2**, 730-734 (2010).

- *Reply to "Comment on 'Catalytic activity of the Rh surface oxide: CO oxidation over Rh(111) under realistic conditions' ",*
  J. Gustafson, R. Westerström, O. Balmes, A. Resta, R. van Rijn, X. Torrelles, C.T. Herbschleb, J. W. M. Frenken, and E. Lundgren,
  Journal of Physical Chemistry C **114**, 22372-22373 (2010).

- *Catalytic activity of the Rh Surface Oxide: CO oxidation over Rh(111) under realistic conditions,*
  J. Gustafson, R. Westerström, O. Balmes, A. Resta, R. van Rijn, X. Torrelles, C. T. Herbschleb, J. W. M. Frenken, and E. Lundgren,
  Journal of Physical Chemistry C **114**, 4580-4583 (2010).

- *Comment on "CO Oxidation on Pt-Group Metals from Ultrahigh Vacuum to Near Atmospheric Pressures. 2. Palladium and Platinum",*
  R. van Rijn, O. Balmes, R. Felici, J. Gustafson, D. Wermeille, R. Westerström, E. Lundgren, and J. W. M. Frenken,
  Journal of Physical Chemistry C **114**, 6875-6876 (2010).

- *Ultrahigh vacuum/high-pressure flow reactor for surface x-ray diffraction and grazing incidence small angle x-ray scattering studies close to conditions for industrial catalysis,*
  R. van Rijn, M. D. Ackermann, O. Balmes, T. Dufrane, A. Geluk, H. Gonzalez, H. Isern, E. de Kuyper, L. Petit, V. A. Sole, D. Wermeille, R. Felici, and J. W. M. Frenken,
  Review of Scientific Instruments **81**, 014101 (2010).

- *The ID03 surface diffraction beamline for in situ and real-time X-ray investigations of catalytic reactions at surfaces,*
  O. Balmes, R. van Rijn, D. Wermeille, A. Resta, L.Petit, H. Isern, T. Dufrane, and R. Felici,
  Catalysis Today **145**, 220-226 (2009).

Curriculum vitae

Richard van Rijn was born on July 5, 1983 in Delft . He obtained his VWO diploma from the Westland College in Naalwijk in 2001 and enrolled at Leiden University to study physics. After completing the undergraduate courses in 2005, he started studying the formation and diffusion of single-atom thick gold wires on a gold surface in the framework of a M.Sc. thesis project under the supervision of Dr. M. J. Rost. After this project he spent 5 months assembling, testing and designing parts of a flow reactor for the in situ study of model catalysts with surface x-ray diffraction at the European Synchrotron Radiation Facility (ESRF) in Grenoble, France. This work was done under the supervision of Dr. R. Felici. In 2007 he received his M.Sc. degree (cum laude) in physics from Leiden University.

In September 2007 he continued his work on the flow reactor under the joint supervision of Dr. R. Felici at the ESRF and Prof. dr. J. W. M. Frenken at Leiden University. The research project aimed at developing and using the flow reactor for in situ measurements of heterogeneous model catalysts. The results of this project are described in this thesis.